

A FOUNDATION FOR ARTIFICIAL PHOTOSYNTHESIS

Ciro Di Meglio

B.S., Worcester Polytechnic Institute, 1989

M.S., Oregon Graduate Institute of Science and Technology, 1996

A dissertation submitted to the faculty of the
Oregon Graduate Institute of Science and Technology
in partial fulfillment of the
requirements for the degree
Doctor of Philosophy
in
Chemistry

December 1999

The dissertation "A Foundation for Artificial Photosynthesis" by Ciro Di Meglio has been examined and approved by the following Examination Committee:

David H. Thompson
Associate Professor and Research Advisor
Purdue University

David W. Grainger
Associate Professor
Colorado State University

James K. Hurst
Professor
Washington State University

Shankar B. Rananavare
Assistant Professor
Portland State University

ACKNOWLEDGMENTS

There are many people who have provided assistance in many forms which allowed me to complete my graduate studies.

Thanks to Dr. David H. Thompson for the opportunity to do research in his laboratory. Thanks to Drs. David W. Grainger, Shankar B. Rananavare, and James K. Hurst for their ongoing guidance and service on my dissertation examination committee. Thanks to Dr. Thomas M. Loehr for prodding me along when things got slow, and to Nancy Christie and Terrie Hadfield for their proofreading, wordprocessing, and mothering.

Thanks to Dr. Jack Spadaro for his long-time friendship, and most especially I thank my parents for their love and support through all these years.

TABLE OF CONTENTS

ACKNOWLEDGEMENTS	iii
TABLE OF CONTENTS	iv
LIST OF TABLES	vii
LIST OF FIGURES	viii
ABSTRACT	xiii
CHAPTER 1. Design of Artificial Photosynthetic Systems	1
1.1 System Design: General Considerations	4
1.2 System Design: Membrane Component	7
1.3 Retrosynthesis System Design: Transducer Considerations	8
1.4 References	10
CHAPTER 2. Synthesis	17
2.1 Introduction	17
2.2 Instruments	20
2.3 Materials	20
2.4 Synthesis of Chiral Ether Lipids	23
2.5 Partial Route to Racemic Bolaamphiphiles	32
2.6 Synthesis of Porphyrin and Gramicidin A-Porphyrin Diad	35
2.7 References	36
CHAPTER 3. Physical Characterization of Bolaamphiphile Phases	40
3.1 Differential Scanning Calorimetry	40
3.1.1 Chain-melting transition	41
3.1.2 Instrumental	42

3.1.3	Results	44
3.2	Small Angle X-ray Scattering Spectroscopy	48
3.2.1	Experimental	53
3.3	Monolayer Experiments	68
3.3.1	Introduction	68
3.3.2	Experimental setup	78
3.3.3	General experimental considerations	79
3.3.4	Monolayer data	79
3.5	References	83
 CHAPTER 4. Characterization of Bolaamphiphile Vesicles		84
4.1	Introduction	84
4.2	Dynamic Light Scattering Spectroscopy	85
4.2.1	Introduction	85
4.2.2	Experimental	86
4.3	Cryo-TEM	90
4.3.1	Experimental method	90
4.3.2	Results	91
4.3.3	Discussion	97
4.4	References	98
 CHAPTER 5. Testing of the Bolaamphiphile-Gramicidin-Porphyrin Design		
	Concept	100
5.1	Flash Photolysis	100
5.1.1	Introduction	100
5.1.2	Experimental	105
5.2	Sodium Nuclear Magnetic Resonance	116
5.2.1	Introduction	116
5.2.2	Experimental	117
5.3	References	133

CHAPTER 6. Conclusion 137

BIOGRAPHICAL SKETCH 141

LIST OF TABLES

3.1	Curve Fitting Parameters for Phase Transition Data Appearing in Figure 3.1	43
3.2	Summary of Small Angle X-ray Scattering Data for C16 and C20 Bolaamphiphiles at Different Extents of Hydration	67
5.1	Summary of ^{23}Na NMR Parameters for 4:1 Phosphatidylcholine:Phosphatidylglycerol Vesicles Containing Gramicidin A	128
5.2	Summary of ^{23}Na NMR Parameters for 7:3 C20 Bolaamphiphile:Cholesterol Vesicles Containing Either Gramicidin A or GAP	129

LIST OF FIGURES

1.1	The photosynthetic Z-scheme of green plants	3
1.2	Schematic diagram depicting an artificial photosynthetic cycle	6
2.1	The basic structure of naturally occurring bolaamphiphiles	18
2.2	Reaction scheme to determine a suitable catalyst for the ring opening of R-oxiranemethanol 3-nitrobenzulfonate 1(R) with a long-chain alcohol	22
2.3	Sequence in the synthesis of C16 and C20 bolaamphiphiles	24
3.1	Plot of the gel-to-lamellar-phase transition temperature as a function of hydrocarbon chain length	43
3.2	Differential scanning calorimetry thermogram of hydrated C16 bolaamphiphile	45
3.3	Differential scanning calorimetry thermogram of hydrated C20 bolaamphiphile	46
3.4	Mean (dynamic) packing shapes and the structures which are formed	49
3.5	Top schematic view of the SAXS setup	52
3.6	Experimental setup used in SAXS	54
3.7	Small-angle X-ray scattering spectrum of lead stearate (calibration)	55
3.8	Small-angle X-ray scattering spectrum of pure C20 bolaamphiphile in the gel phase	57
3.9	Small-angle X-ray scattering spectrum of 90% C20 bolaamphiphile in 10% H ₂ O	58

3.10	Small-angle X-ray scattering spectrum of 80% C20 bolaamphiphile in 20% H ₂ O in the gel phase	59
3.11	Small-angle X-ray scattering spectrum of 75% C20 bolaamphiphile in 25% H ₂ O in the gel phase	60
3.12	Small-angle X-ray scattering spectrum of 60% C20 bolaamphiphile in 40% H ₂ O in the lamellar phase	61
3.13	Small-angle X-ray scattering spectrum of 50% C20 bolaamphiphile in 50% H ₂ O in the lamellar phase	62
3.14	Small-angle X-ray scattering spectrum of 35% C20 bolaamphiphile in 65% H ₂ O with coexistence of the lamellar and vesicular phases	63
3.15	Small-angle X-ray scattering spectrum of 25% C20 bolaamphiphile in 75% H ₂ O with coexistence of the lamellar and vesicular phases	64
3.16	Plot indicating the dependence of d-spacings obtained from SAXS upon varying water levels with C20 bolaamphiphile	65
3.17	Small-angle X-ray scattering spectrum of pure C16 bolaamphiphile	69
3.18	Small-angle X-ray scattering spectrum of 90% C16 bolaamphiphile in 10% H ₂ O	70
3.19	Small-angle X-ray scattering spectrum of 80% C16 bolaamphiphile in 20% water in the lamellar phase	71
3.20	Small-angle X-ray scattering spectrum of 70% C16 bolaamphiphile in 30% H ₂ O	72
3.21	Observed dependence of d-spacing upon varying water levels with C16 bolaamphiphile (approximate phase diagram)	73
3.22	A comparison of isotherms, acquired at the air–water interface, of several dialkyl phosphatidylcholines	77
3.23	A comparison of pressure versus area isotherms, acquired at the air–water interface, of several dialkyl phosphatidylcholines	80
3.24	A comparison of pressure versus area per headgroup isotherms, acquired at the air–water interface, of several dialkyl phosphotidylcholines	81

4.1	Dynamic light-scattering data from pure C20 bolaamphiphiles	87
4.2	Dynamic light-scattering data from 7:3 C20 bolaamphiphile:cholesterol vesicles	89
4.3	Cryo-transmission electron micrograph of pure C20 bolaamphiphiles in tris buffer	93
4.4	Cryo-transmission electron micrograph of 7:3 C20 bolaamphiphile: cholesterol vesicles in tris buffer	95
4.5	Cryo-transmission electron micrograph of 7:3 C20 bolaamphiphile: cholesterol vesicles after insertion of gramicidin A	96
5.1	Schematic cycle depicting GAPQ function in a C20 bolaamphiphile: cholesterol vesicle membrane	104
5.2	Schematic diagram showing experimental flash photolysis setup used for the triplet state lifetime measurements of GAP inserted in C20 bolaamphiphile:cholesterol vesicles	106
5.3	Triplet state lifetimes measured by flash photolysis of the GAP diad inserted into deoxygenated vesicles of 7:3 C20 bolaamphiphile: cholesterol in 20 mM tris buffer, pH 8	107
5.4	First-order plots of GAP porphyrin triplet states from the experiments conducted in 7:3 bolaamphiphile:cholesterol vesicles	108
5.5	Schematic diagram showing GAP inserted into preformed 7:3 C20 bolaamphiphile:cholesterol vesicles	110
5.6	Schematic diagram showing GAP inserted into preformed 7:3 C20 bolaamphiphile:cholesterol vesicles with intravesicular EDTA	111
5.7	Spectra indicating the progress of photoinduced electron transfer in 7:3 C20 bolaamphiphile:cholesterol vesicles with the GAP diad inserted	113
5.8	Expanded spectra indicating the progress of photoinduced electron transfer in 7:3 C20 bolaamphiphile:cholesterol vesicles with the GAP diad inserted	114
5.9	Schematic diagram showing possible orientations of GAP in a 7:3 C20 bolaamphiphile:cholesterol vesicle	115

5.10	Sodium NMR spectral data (points) and NLSFIT simulation (line) of 7:3 C20 bolaamphiphile:cholesterol vesicles (in the absence of gramicidin A) with sodium ions inside and Dy(PPP) ₂ outside	118
5.11	Sodium NMR spectra of vesicles measuring leakage as a function of time	120
5.12	Sodium NMR spectral data (points) and the NLSFIT simulation (line) of 7:3 C20 bolaamphiphile:cholesterol vesicles with one native gramicidin channel inserted within the membrane and Dy(PPP) ₂ added outside	121
5.13	Sodium NMR spectral data (points) and the NLSFIT simulation (line) of 7:3 C20 bolaamphiphile:cholesterol vesicles with five native gramicidin channels inserted within the membrane and Dy(PPP) ₂ outside	122
5.14	Sodium NMR spectral data (points) and NLSFIT simulation (line) of C20 bolaamphiphile:cholesterol vesicles containing 10 GAP channels per vesicle	123
5.15	Sodium NMR spectral data, digitized from published data (points) and NLSFIT simulation (line) of 4:1 phosphatidylcholine: phosphatidylglycerol vesicles in the absence of gramicidin channels	125
5.16	Sodium NMR spectral data (points) and NLSFIT simulation (line) of 4:1 phosphatidylcholine:phosphatidylglycerol vesicles containing 110 gramicidin channels per vesicle	126
5.17	Sodium NMR spectral data digitized from published data (points) and NLSFIT simulation (line) of 4:1 phosphatidylcholine:phosphatidylglycerol vesicles containing 166 gramicidin channels per vesicle	127
5.18	NMR computer simulation of 0.4 micron vesicles while the exchange rates are varied up to 5000 ions per second	130

5.19	NMR computer simulation of 0.1 micron vesicles while the exchange rates are varied up to 5000 ions per second	133
6.1	The GAPQ triad	140

ABSTRACT

A Foundation for Artificial Photosynthesis

Ciro Di Meglio

Oregon Graduate Institute of Science and Technology

Supervising Professor: David H. Thompson

The purpose of this study was to develop a model for an artificial photosynthetic device by coupling photoinduced electron and compensating ion transfer across an ultrathin bolaamphiphile membrane. Initially, an efficient, gram scale, synthetic route for the chiral synthesis of the short-chained bolaamphiphile phosphocholines, 2,2'-di-*O*-octyl-3,3'-*O*-hexadecamethylenedi-*sn*-glycerol-1,1'-diphosphocholine (C16 bolaamphiphile) and 3,3'-di-*O*-decyl-3,3'-*O*-eicosamethylenedi-*sn*-glycerol-1,1'-diphosphocholine (C20 bolaamphiphile), was developed. Several methods of physical characterization were employed to characterize the dispersions of these materials. Their phase behavior was studied using differential scanning calorimetry, monolayer film balance and small angle X-ray scattering techniques. The onset of the vesicular phase for the C16 bolaamphiphile occurred when the lipid concentration in water was 70% or less, while the vesicular phase for C20 bolaamphiphile was observed at concentrations of less than 35% lipid in water. The transmembrane dimensions were determined to be 32 Å for the C20 bolaamphiphile and 33 Å for the C16 bolaamphiphile with melting transitions at -27°C and 12°C, respectively.

Cryo-transmission electron microscopy of extruded 100:0 and 7:3 bolaamphiphile:cholesterol mixtures indicated that vesicles were formed in both cases; however, the pure C20 bolaamphiphile gave rise to large non-spherical morphologies

while the 7:3 bolaamphiphile:cholesterol mixtures were spherical 840-Å particles. No significant size changes were observed upon incorporation of a gramicidin derivative into these vesicles. A preliminary flash photolysis study was then undertaken to determine the orientation of an asymmetrically inserted gramicidin-porphyrin diad in 7:3 C20 bolaamphiphile vesicle membrane. The first-order triplet porphyrin decay constants in the presence and absence of 600 μM methylviologen were 2.8×10^{-3} and 2.6×10^{-3} , consistent with the porphyrin being inaccessible to extravesicular methylviologen. Steady-state photolysis experiments in the presence of EDTA and externally adsorbed decylviologen, however, suggested that the internal porphyrin and external decylviologen were close enough for transmembrane electron transfer.

Sodium NMR experiments in the presence of extravesicular dysprosium tripolyphosphate demonstrated that unmodified gramicidin was capable of exchanging sodium ions three orders of magnitude faster across 7:3 C20 bolaamphiphile:cholesterol vesicle membranes than in bilayer membranes, while the porphyrin-modified gramicidin was nearly 500 times faster.

These studies indicate that this model supramolecular system may potentially undergo photoinduced electron transfer with coupled cation transport across the thin monolayer membranes of bolaamphiphile vesicles.

CHAPTER 1

DESIGN OF ARTIFICIAL PHOTOSYNTHETIC SYSTEMS

In a world facing exponential population growth, one of the greatest technological problems is the ability to provide the basic energy required for modern living standards. The past consumption of cheap power from hydroelectric, nuclear and fossil fuel technologies has led to intolerable environmental pressure on wetlands, pollution, and global warming. It is for this reason that clean, renewable and environmentally innocuous sources of energy must be developed. In 1950, Bell Laboratories' research efforts exploiting the photoelectric effect yielded photovoltaic (PV) panels which have proven useful for remote power. However, when sunlight strikes a PV cell, only the photons with a certain level of energy are able to produce an electric current. Construction costs for a PV panel, combined with the inherent inefficiency due to limited spectral region being absorbed, results in a long period before the power produced becomes cost effective. This problem has limited the widespread use of PV panels for power production. New approaches are being sought to overcome the problems of satisfying energy requirements through solar photoconversion. The efficiency of solar energy utilization in biological photosynthesis has led to bio-mimetic approaches in the conversion of sunlight into a storable chemical fuel.

Biological organisms have evolved to utilize solar radiation. Photosynthetic organisms make use of long-range electron transfer to drive biologically relevant reactions [1]. For example, photosynthesis in plants requires charge separation across the thylakoid membranes of the green chloroplasts [2]. The photosynthetic reaction center from the purple bacterium *Rhodospseudomonas viridis* is also poised in a membrane with light-harvesting and electron-transfer sites [3,4]. It is of great interest to understand the organization of the supramolecular constituents which are

responsible for biological photoconversion. The structure and photochemical kinetics of the green plant photosynthetic reaction centers have been the subject of extensive investigations for over three decades [5–12]. These labors have provided a detailed understanding of the geometrical relationships and redox characteristics essential for the highly efficient initial charge separation required of photosynthesis. From this work, we have learned that the photosynthetic machinery includes lipid bilayer membranes, light-absorbing pigments, redox chains as mediators of electron transfer, and a water-splitting enzyme which are represented schematically as a Z-shaped pattern (Figure 1.1). The lipid bilayer membranes serve to maintain charge separation across a thin barrier film of low dielectric constant, while also hosting adenosine triphosphate (ATP) synthase proteins which provide the organism with the stored energy which is directly utilized by life—ATP. The light-absorbing chlorophyll pigments transfer excited-state energy in an "antenna" fashion until the energy can be given to the chlorophyll special pair. Beginning with photosystem II (P_{680}), an electron is relayed to pheophytin a, then to bound quinone molecules (PQ_a , PQ_b), followed by mobile proton-translocating quinones in the plastoquinone pool. The quinones then reduce cytochrome *f* which is then oxidized by plastocyanin (PCY). Two protons are translocated across the membrane in this process. A second photon is absorbed and used by photosystem I which transfers an electron to the iron-sulfur protein ferredoxin (Fd), which reduces nicotinamide adenine dinucleotide (NAD), another vital electron carrier. The water-splitting catalyst (S) fills the hole created in PS II while generating oxygen and protons, thereby completing the cycle. Therefore, the initial events of light-initiated proton translocation and electron transfer ultimately result in the synthesis of ATP and NADPH.

With the understanding of the electron transfer events comes the desire to artificially emulate biological photosynthesis, aspiring to make solar photoconversion an affordable energy-producing alternative. Mimicking a highly complex chemical process such as biological photosynthesis presents a multifaceted challenge to the chemist interested in synthesizing polyfunctional molecules which are capable of engaging in similar photoinduced charge-transfer reactions [13]. The generation of long-lived charge-separated intermediates derived from photoinduced electron transfer

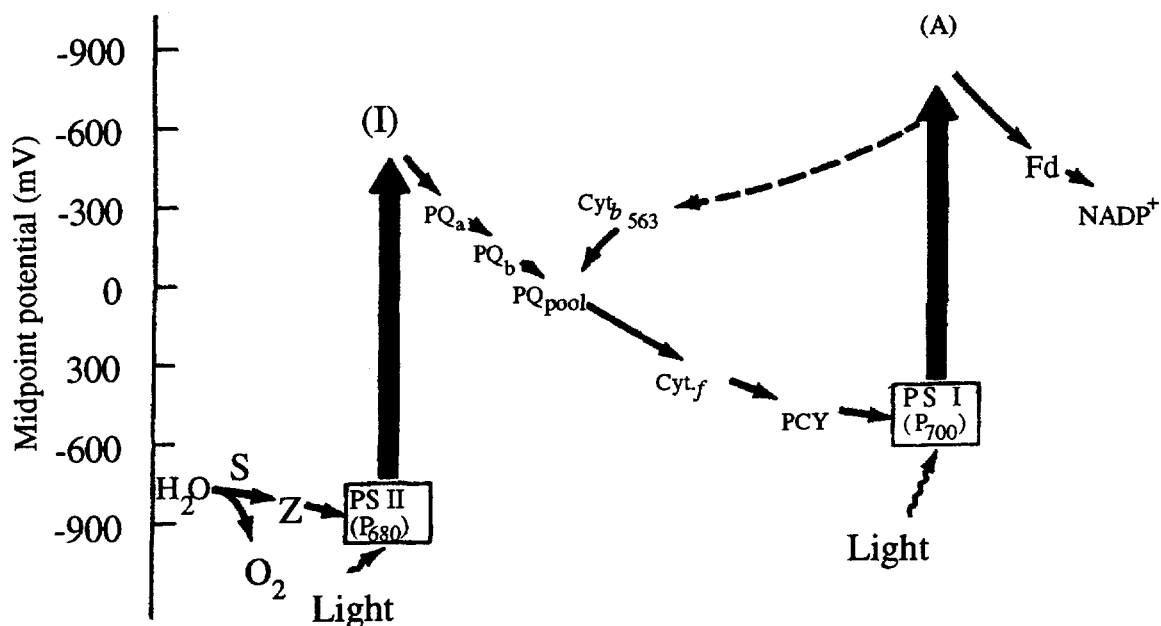


Figure 1.1 The photosynthetic Z-scheme of green plants. The arrows indicate the flow of electrons. This system is found in the hydrophobic region of the thylakoid membranes and is organized for vectorial electron transfer. In addition, protons are translocated by the plastoquinone pool.

Adapted from Figure 2 published in the following and used here with permission of the American Society for Photobiology.

Calvin, M. (1983) Artificial photosynthesis: quantum capture and energy storage. *Photobiochem. Photobiol.* 37, 349-360.

processes between vectorial-oriented synthetic donor and acceptor molecules could provide the membrane potential required to drive solar photoconversion.

1.1 System Design: General Considerations

Whereas biological photosynthesis uses a membrane potential and ion gradients to drive a multitude of biologically significant reactions such as ATP synthesis, a model system for solar photoconversion would use the membrane potential and ion gradients to generate a usable fuel. The primary challenge in developing a model system for solar photoconversion involves synthesizing thermochemically stable components that will selectively orient the donor-acceptor pair in a vectorial, asymmetric arrangement within the membrane in order to permit the coupled transport of electrons and protons. These components would ultimately consist of a membrane-spanning, photoredox-active ion channel capable of vectorial electron and cation transfer across a membrane barrier. The membrane must possess the capacitive properties that are similar to those found in biological membranes, thereby prohibiting nonselective ion movement. The membrane must also have a transmembrane dimension which allows the ion channel derivative to form an active state.

Previous attempts to enhance the efficiency of this class of reactions have focused on tuning the redox potentials of the donor and acceptor moieties [14], varying their intermolecular medium and spacing, or the complex synthesis of polyfunctional molecules [15]. Each approach has been successful to some extent when employed as the sole strategy. However, there are serious practical limitations to these approaches from the standpoint of the materials synthesis, device engineering, and chemical stability of the components. Many examples of coupled redox molecules exist based on donor-linker-acceptor triads [15-18], tetrads, and pentads [19]. Several interfacially separated charge pairs have been reported in dihexadecylphosphate (DHP) using zinc tetraphenylporphyrin sulfonate (ZnTPPS^{4-}) and alkylviologens [20], phosphatidylcholine (PC) vesicles and polymer-linked manganese porphyrins [21], or tetra(alkyl phosphocholine)-substituted zinc porphyrins [22] C_{70} fullerene/diphytanoyl-phosphatidylcholine bilayers [23], carbazole bilayers in

the presence of acceptors [24], zeolite-based molecular triads [25], as well as in self-assembled monolayers [26–28], colloidal semiconductors [29], and micelles [30,31]. Similar effects have been reported in bolaamphiphile systems [32,33], tetraarylborate/carbocyanine-based liposomes [34], donor–acceptor derivatized peptide helices [35,36], phospholipid-linked manganese porphyrins [37], membrane-immobilized triporphyrins [38], and an array of vectorial electron transfer reactions in liposomal matrices [39–42]. The common conclusion from these examples is that electron transfer in linked donors and acceptors is observed. The shortcoming of these systems comes from the well-described rate-limiting effects of membrane polarization due to uncoupled electron and ion transport across closed bilayer membrane vesicles [43–46]. There are very few supramolecular systems which integrate both electron and ion transport into their design [41,42,46–49]. While chemists lack the ability to synthesize and assemble systems approaching biological complexity [51,52], clever approaches may yield systems unattained through evolution to serve as simple models [12,50].

This dissertation describes the construction of a stable ultrathin synthetic membrane, mimicking the function and asymmetry of the bilayer liposomes in biological photosynthesis by the vectorial incorporation of a naturally occurring ion channel derivatized with a lipophilic porphyrin moiety as a photoinitiated electron donor, while directing membrane asymmetry aimed at constructing a model for solar photoconversion. This development aims for a composite photoinduced donor–ion channel linker–acceptor triad asymmetrically inserted into a thin bolaamphiphile membrane—a model photochemical system which would allow the correlated movement of electrons and ions across a membrane. The net result of this process will be to accumulate reducing equivalents on one membrane surface and oxidizing capacity on the other, poised for coupling to secondary (water-splitting and hydrogen-evolving) reactions (Figure 1.2).

Membrane Barrier

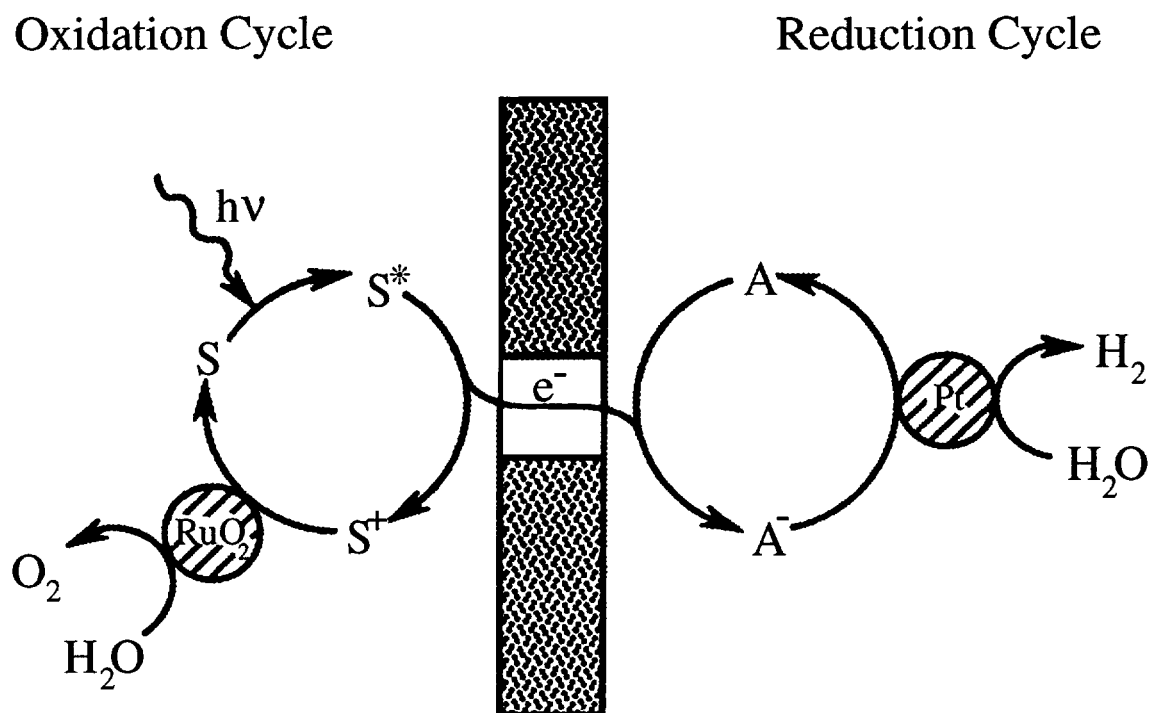


Figure 1.2 Schematic diagram depicting an artificial photosynthetic cycle. Electrons are transferred from a photosensitive donor to an acceptor. These processes are then coupled to water oxidation and hydrogen production.

1.2 System Design: Membrane Component

Several important considerations must be recognized in order to design target amphiphiles which are to self-assemble into vesicles from which a model photoconversion device can be constructed. The design of the amphiphile and the membrane that it forms must incorporate both molecular and supramolecular stability for ultimate success. The exponential dependence on distance of the electron tunneling probability, as estimated from a rectangular barrier approximation $p = Ae^{-\beta d}$, indicates that small changes in the distance in which an electron must be transferred would result in large changes in electron tunneling probabilities. Therefore, diminishing the transmembrane thickness in order to allow the donor and acceptor of a photoactive electron transfer complex to be closer should promote the electron transfer process. Thus, design of an ultrathin membrane for an artificial photosynthetic system would be advantageous.

In order to assemble vesicles having thinner membranes, the amphiphiles to be synthesized must possess a shorter hydrophobic component. The minimum membrane thickness that can be achieved, while retaining membrane stability, must consider the balance between the hydrophobic and hydrophilic contributions required for the lipids to self-assemble into vesicles. Lipids with short alkyl chains would not lead to stable vesicles, but would instead favor the formation of micelles. The gemini surfactants represent this class of materials [56].

Furthermore, the chemical stability of the amphiphile must be considered. Ester-linked lipids, which are most common, are unstable towards both acid- and base-catalyzed hydrolysis reactions. For these stability-related reasons, synthetic ultrathin membranes have been modeled after membranes found in thermophilic acidophilic archaeobacteria such as *Sulfolobus acidocaldarius*. These bacteria thrive in conditions of high temperatures (up to 85°C) and low pH (approaching pH 2–3) [53–55]. These archaeobacteria are able to thrive in such harsh environments without detrimental effects due to the specialized chemical architecture of their membranes. The unique stability of these archaeobacterial lipids compared to conventional diacylglycerophosphocholine lipids arises, in part, from ether linkages bonding the

hydrophobic chains to the glycerol backbone, in contrast to naturally prevalent ester linkages. These bipolar ether lipids form liposomes similar to lipid bilayers, but are technically monolayers as a result of their membrane-spanning nature [51-53]. These bipolar lipids are referred to as bolaamphiphiles [54].

By adapting structural features from archaeobacterial bolaamphiphiles, two different synthetic bolaamphiphiles were designed. In both bolaamphiphiles phosphatidylcholine headgroups were chosen to avoid problems associated with electrostatic repulsion. The headgroups are attached to glycerol backbones. These glycerol backbones are also ether linked to membrane-spanning and half-membrane-spanning polymethylene chains [55].

1.3 Retrosynthesis System Design: Transducer Considerations

The ultrathin bolaamphiphile membrane was conceived to accelerate the transfer of electrons and ions across it in a model photosynthetic system. The transducer of electrons and ions was chosen to be a ion channel which would be derivatized with a photoinduced electron donor and acceptor pair. The transmembrane dimension poses limitations on the dimension of the ion channel to be included. If the channel is too long, the inserted geometry of the channel would not be orthogonal to the opposing aqueous interfaces, giving unpredictable behavior once derivatized with the donor and acceptor pair. If the channel is too short, it may not act as a channel, but rather as a carrier as it shuttles back and forth across the membrane. For these reasons, gramicidin was chosen to act as the ion channel in the system.

Gramicidin D is a mixture of four different linear alternating D/L pentadecapeptides which *Bacillus brevis* secretes as an antibiotic to dissipate ion gradients in the organisms that it consumes for food. Gramicidin A (HCO-L-Val¹-D-Gly²-L-Ala³-D-Leu⁴-L-Ala⁵-D-Val⁶-L-Val⁷-D-Val⁸-L-Trp⁹-D-Leu¹⁰-L-Trp¹¹-D-Leu¹²-L-Trp¹³-D-Leu¹⁴-L-Trp¹⁵-NH₂CH₂OH) is one component of the mixture [57]. The gramicidins all assume a right-handed $\beta^{6.3}$ -helix conformation with a monomer length of approximately 15 Å in conventional phospholipid bilayers. Gramicidin A functions

in biological systems as a gradient-dissipating monovalent ion channel for cations smaller than Cs^+ . The native ion channel state of gramicidin A in a bilayer membrane is an anti-parallel dimer that is hydrogen-bonded between the N-formyl termini located at the center of the bilayer [58–68]. Since the dimer acts as an ion channel in membranes which are approximately twice the thickness of the synthetic bolaamphiphile membranes, an assumption was made that the gramicidin monomer may act as an active channel in the thinner bolaamphiphile membrane environment.

Ultimately, a bifunctional channel, 5,10,15,20-tris(4'-methylphenyl)porphyrin-gramicidin A-quinone (GAPQ), would be integrated into ultrathin bolaamphiphile membranes [69]. These materials should interact in a composite triad/bolalipid photochemical system in the following ways:

- (a) The vectorial orientation within the membrane, driven by the amphiphilic nature of the derivatized channel and the attached porphyrin and quinone, would produce an asymmetric membrane structure having both oxidizing and reducing surfaces.
- (b) Self-annihilation of the initially charge-separated pair would be inhibited by separating terminal donor and acceptor moieties at opposing membrane interfaces.
- (c) The photoinduced transmembrane electron transfer rates would be accelerated by reduction of the donor-acceptor separation distance.
- (d) The membrane potential gradient generated by the transmembrane electron transfer would result in the translocation of an ion by the integrated channel.

The following chapters describe the synthetic methods used to synthesize the system components, the various experiments used to define the phase behavior, morphology of the membrane component, methods and verification of the inclusion of the partially constructed ion-translocating photoinduced electron transfer complex (5,10,15,20-tris(4'-methylphenyl)porphyrin-gramicidin A, GAP), a demonstration of the photoinduced electron transfer properties, and ion channel function of GAP in bolaamphiphile vesicles.

1.4 References

1. Harold, F. M. (1986) *The Vital Force: A Study of Bioenergetics*, W. H. Freeman & Co., New York.
2. Calvin, M. (1983) Artificial photosynthesis: quantum capture and energy storage. *Photochem. Photobiol.* **37**, 349–360.
3. Deisenhofer, J., Epp, O., Miki, K., Huber, R., and Michel, H. (1986) Structure of the protein subunits in the photosynthetic reaction center of *Rhodospseudomonas viridis* at 3 Å resolution. *Nature* **318**, 618–624.
4. Deisenhofer, J., and Michel, H. (1989) Nobel lecture. The photosynthetic reaction centre from the purple bacterium *Rhodospseudomonas viridis*. *EMBO J.* **8**, 2149–2170.
5. Huber, R. (1989) Nobel lecture. A structural basis of light energy and electron transfer in biology. *Angew. Chem. Int. Ed. Engl.* **28**, 848–869.
6. Norris, J. R., and Raghavan, M. (1991) Strategies for mimicking the primary events of bacterial photosynthesis: structure, function, and mechanism. In *Photochemical Conversion and Storage of Solar Energy* (Pelizzetti, E. and Schiavello, M., Eds.) Kluwer Academic Publishers, Dordrecht, pp. 141–150.
7. Boxer, S. G. (1990) Mechanisms of long-distance electron transfer in proteins: lessons from photosynthetic reaction centers. *Annu. Rev. Biophys. Biophys. Chem.* **19**, 267–299.
8. Moser, C. C., Keske, J. M., Warncke, K., Farid, R. S., and Dutton, P. L. (1992) Nature of biological electron transfer. *Nature* **355**, 796–802.
9. Beratan, D. N., Betts, J. N., and Onuchic, J. N. (1991) Protein electron-transfer rates set by the bridging secondary and tertiary structure. *Science* **252**, 1285–1288.
10. Grätzel, M. (Ed.) (1987) *Energy Resources Through Photochemistry and Catalysis*, Academic Press, New York.
11. Willner, I., and Willner, B. (1991) Photosensitized electron-transfer reactions in supramolecular assemblies. In *Frontiers in Supramolecular Organic Chemistry and Photochemistry* (Schneider, H.-J. and Durr, H., Eds.) VCH, New York, pp. 337–375.
12. Robinson, J. N., and Cole-Hamilton, D. J. (1991) Electron transfer across vesicle bilayers. *Chem. Soc. Rev.* **20**, 49–94.

13. Lehn, J.-M. (1988) Supramolecular chemistry—scope and perspectives molecules, supermolecules, and molecular devices. *Angew. Chem. Int. Ed. Engl.* **27**, 89–112.
14. Juris, A., Balzani, V., Barigelletti, F., Campagna, S., Belser, P., and Von Zelewsky, A. (1988) Ruthenium(II) polypyridine complexes: Photophysics, photochemistry, electrochemistry, and chemiluminescence. *Coord. Chem. Rev.* **84**, 85–277.
15. Jordan, K. D., and Paddon-Row, M. N. (1992) Analysis of the interactions responsible for long-range through-bond-mediated electronic coupling between remote chromophores attached to rigid polynorbornyl bridges. *Chem. Rev.* **92**, 395–410.
16. Wasielewski, M. R. (1992) Photoinduced electron transfer in supramolecular systems for artificial photosynthesis. *Chem. Rev.* **92**, 435–461.
17. Isied, S. S., Ogawa, M. Y., and Wishart, J. F. (1992) Peptide-mediated intramolecular electron transfer—long-range distance dependence. *Chem. Rev.* **92**, 381–394.
18. Arrhenius, T. S., Blanchard-Desce, M., Dvolaitzky, M., Lehn, J.-M., and Malthete, J. (1986) Molecular devices: caroviologens as an approach to molecular wires—synthesis and incorporation into vesicle membranes. *Proc. Natl. Acad. Sci. USA* **83**, 5355–5359.
19. Gust, D., and Moore, T. A. (1989) Mimicking photosynthesis. *Science* **244**, 35–41.
20. Hurst, J. K., Thompson, D. H., and Connolly, J. S. (1987) Photooxidation of tetraanionic sensitizer ions by dihexadecylphosphate vesicle-bound viologens. *J. Am. Chem. Soc.* **109**, 507–515.
21. Dannhauser, T. J., Nango, M., Oku, N., Anzai, K., and Loach, P. A. (1986) Transmembrane electron transfer as catalyzed by poly(ethylenimine)-linked manganese porphyrins. *J. Am. Chem. Soc.* **108**, 5865–5871.
22. Tsuchida, E., Kaneko, M., Nishide, H., and Hoshino, M. (1986) Distance dependence of electron transfer from liposome-embedded (alkanephosphocholine-porphinato)zinc. *J. Phys. Chem.* **90**, 2283–2284.
23. Hwang, K. C., and Mauzerall, D. (1993) Photoinduced electron transport across a lipid bilayer mediated by C70. *Nature* **361**, 138–140.

24. Kunitake, T. (1987) Synthetic bilayer membranes: their relevance to photochemical energy-conversion. *Nouv. J. Chim.* **11**, 141–144.
25. Krueger, J. S., Mayer, J. E., and Mallouk, T. E. (1988) Long-lived light-induced charge separation in a zeolite I-based molecular triad. *J. Am. Chem. Soc.* **110**, 8232–8234.
26. Creager, S. E., Collard, D. M., and Fox, M. A. (1990) Mediated electron transfer by a surfactant viologen bound to octadecanethiol on gold. *Langmuir* **6**, 1617–1620.
27. (a) Chidsey, C. E. D. (1991) Free energy and temperature dependence of electron transfer at the metal-electrolyte interface. *Science* **251**, 919–922.
(b) Chidsey, C. E. D. (1991) Correction. *Science* **252**, 631–631.
28. Miller, C., Cuendet, P., and Grätzel, M. (1991) Adsorbed omega-hydroxy thiol monolayers on gold electrodes—evidence for electron tunneling to redox species in solution. *J. Phys. Chem.* **95**, 877–886.
29. Grätzel, M. (1989) *Heterogeneous Photochemical Electron Transfer*, CRC Press, Boca Raton, FL.
30. Kalyanasundaram, K. (1987) *Photochemistry in Microheterogeneous Systems*, Academic Press, Orlando, FL, Chap. 4-5, pp. 122–172.
31. Lawson, D. R., Liang, W., and Martin, C. R. (1993) Inorganic and biological electron transfer across an electronically conductive composite polymer membrane. *Chem. Mater.* **5**, 400–402.
32. Führop, J.-H., Krull, M., Schulz, A., and Möbius, D. (1990) Bolaform amphiphiles with a rigid hydrophobic bixin core in surface monolayers and lipid membranes. *Langmuir* **6**, 497–505.
33. Führop, J.-H., Hungerbühler, H., and Siggel, U. (1990) Quinone-containing amphiphiles and bolaform amphiphiles that form redox-active lipid membranes. *Langmuir* **6**, 1295–1300.
34. Armitage, B., and O'Brien, D. F. (1992) Vectorial photoinduced electron transfer between phospholipid membrane-bound donors and acceptors. *J. Am. Chem. Soc.* **114**, 7396–7403.
35. Mihara, H., Nishino, N., Hasegawa, R., Fujimoto, T., Usui, S., Ishida, H., and Ohkubo, K. (1992) Design of a hybrid of 2 alpha-helix peptides and ruthenium trisbipyridine complex for photoinduced electron-transfer system in bilayer membranes. *Chem. Lett.* **9**, 1813–1816.

36. (a) Inai, Y., Sisido, M., and Imanishi, Y. (1991) Photoinduced electron transfer on a single alpha-helical polypeptide chain: evidence of a through-space mechanism. *J. Phys. Chem.* **95**, 3847–3851.
(b) Inai, Y., Sisido, M., and Imanishi, Y. (1990) Distance and orientation dependence of electron transfer and exciplex formation of naphthyl and p-dimethylanilino groups fixed on a helical polypeptide-chain. *J. Phys. Chem.* **94**, 6237–6243.
37. Nango, M., Mizusawa, A., Miyake, T., and Yoshinaga, J. (1990) Transmembrane electron transfer catalyzed by phospholipid-linked manganese porphyrins. *J. Am. Chem. Soc.* **112**, 1640–1642.
38. Lamrabte, A., Janot, J. M., Bienvenue, E., Momenteau, M., and Seta, P. (1991) Photoinitiated vectorial transmembrane electron transfer in bilayers sensitized by a face to face triporphyrin acting as a molecular electronic device. Amplification due to ionic coupling. *Photochem. Photobiol.* **54**, 123–126.
39. Kuhn, E. R., and Hurst, J. K. (1993) Mechanisms of vectorial transmembrane reduction of viologens across phosphatidylcholine bilayer membranes. *J. Phys. Chem.* **97**, 1712–1721.
40. Zhao, Z.-G., and Tollin, G. (1992) Chlorophyll-photosensitized electron-transfer reactions in lipid bilayer vesicles—generation of proton gradients across the bilayer coupled to quinone reduction and hydroquinone oxidation. *Photochem. Photobiol.* **55**, 611–619.
41. Cafiso, D. S., and Hubbell, W. L. (1983) Electrogenic proton/hydroxide movement across phospholipid vesicles measured by spin-labeled hydrophobic ions. *Biophys. J.* **44**, 49–57.
42. Witt, H. T. (1987) Examples for the cooperation of photons, excitons, electrons, electric fields and protons in the photosynthesis membrane. *Nouv. J. Chim.* **11**, 91–101.
43. West, I. C. (1991) Redox-linked proton translocation by direct-coupled ligand conduction. *J. Bioenerg. Biomembr.* **23**, 703–714.
44. (a) Lyman, S. V., and Hurst, J. K. (1994) Electrogenic and electroneutral pathways for methyl viologen-mediated transmembrane oxidation-reduction across dihexadecylphosphate vesicular membranes. *J. Phys. Chem.* **8**, 989–996.
(b) Lyman, S. V., and Hurst, J. K. (1992) Mechanisms of viologen-mediated charge separation across bilayer-membranes deduced from mediator permeabilities. *J. Am. Chem. Soc.* **114**, 9498–9503.

45. Zhao, Z.-G., and Tollin, G. (1993) Vectorial electron transport across lipid vesicle membranes driven by 2 photoreactions. 1. Ethylenediaminetetraacetic acid as an electron donor via flavin triplet state in the inner compartment and cytochrome *c* as an electron acceptor from chlorophyll triplet-state in the outer compartment. *Photochem. Photobiol.* **57**, 331–337.
46. Zhao, Z.-G., and Tollin, G. (1993) Vectorial electron transport across lipid vesicle membranes driven by 2 photoreactions. 2. Photochemical regeneration of reduced cytochrome-*c* by flavin triplet-state and ethylenediaminetetraacetic acid in the inner compartment and reduction of ferredoxin by chlorophyll triplet-state in the outer compartment. *Photochem. Photobiol.* **57**, 338–343.
47. Tabushi, I., and Kugimiya, S. (1985) Phase-transfer-aided FMNH production using artificial photosynthesis cells of bacterial type. Cell system optimization by the concept of flux conjugation. *J. Am. Chem. Soc.* **107**, 1859–1863.
48. Thompson, D. H., and Hurst, J. K. (1988) Intermolecular transmembrane redox—Electron tunneling or molecular diffusion? In *Molecular Electronic Devices III* (Carter, F. L., Siatkowski, R. E., and Wohltjen, H., Eds.), Elsevier, Amsterdam, pp. 413–425.
49. Kuhn, H. (1979) Synthetic molecular organizates. *J. Photochem.* **10**, 111–132.
50. Ahmed, F. R., Burrows, P.E., Donovan, K. J., and Wilson, E. G. (1988) Organic quantum wells electron transport across Langmuir-Blodgett films of conjugated organic molecules. *Synth. Metals* **27**, B593–B600.
51. De Rosa, M., Gambacorta, A., and Gliozzi, A. (1986) Structure, biosynthesis, and physicochemical properties of archaebacterial lipids. *Microbiol. Rev.* **50**, 70–80.
52. De Rosa, M., Gambacorta, A., and Nicolaus, B. (1983) A new type of cell membrane, in thermophilic archaebacteria, based on bipolar ether lipids. *J. Membr. Sci.* **16**, 287–294.
53. De Rosa, M., Trincone, A., Nicolaus, B., and Gambacorta, A. (1991) In *Life Under Extreme Conditions* (diPrisco, G., Ed.), Springer-Verlag, Berlin, pp. 61–87.
54. Führhop, J.-H., and Mathieu, J. (1984) Pathways to functionalized vesicle membranes without proteins. *Angew. Chem. Int. Ed. Engl.* **23**, 100–113.

55. Thompson, D. H., Svendsen, C. B., Di Meglio, C., and Anderson, V. C. (1994) Synthesis of chiral diether and tetraether phospholipids—regiospecific ring-opening of epoxy alcohol intermediates derived from asymmetric epoxidation. *J. Org. Chem.* **59**, 2945–2955.
56. Menger, F. M., and Littau, C. A. (1993) Gemini surfactants—a new class of self-assembling molecules. *J. Am. Chem. Soc.* **115**, 10083–10090.
57. Stankovic, C. J., Delfino, J. M., and Schreibers, S. L. (1990) Purification of gramicidin A. *Anal. Biochem.* **184**, 100–103.
58. Weinstein, S., Wallace, B. A., Blout, E. R., Morrow, J. S., and Veatch, W. (1979) Conformation of gramicidin A channel in phospholipid vesicles: A carbon-13 and fluorine-19 nuclear magnetic resonance study. *Proc. Natl. Acad. Sci. USA* **76**, 4230–4234.
59. Urry, D. W. (1985) On the molecular structure of the gramicidin transmembrane channel. In *The Enzymes of Biological Membranes*, Vol. 1, 2nd Ed. (Martonosi, A. N., Ed.) Plenum Press, New York and London, pp. 229–257.
60. Nicholson, L. K., and Cross, T. A. (1989) Gramicidin cation channel: an experimental determination of the right-handed helix sense and verification of beta-type hydrogen-bonding. *Biochemistry* **28**, 9379–9385.
61. Chiu, S.-W., Nicholson, L. K., Brenneman, M. T., Subramaniam, S., Teng, Q., McCammon, J. A., Cross, T. A., and Jakobsson, E. (1991) Molecular dynamics computations and solid state nuclear magnetic resonance of the gramicidin cation channel. *Biophys. J.* **60**, 974–978.
62. (a) Prosser, R. S., Daleman, S. I., and Davis, J. H. (1994) The structure of an integral membrane peptide: a deuterium NMR study of gramicidin. *Biophys. J.* **66**, 1415–1428.
(b) Prosser, R. S., and Davis, J. H. (1994) Dynamics of an integral membrane peptide: a deuterium NMR relaxation study of gramicidin. *Biophys. J.* **66**, 1429–1440.
(c) Prosser, R. S., Davis, J. H., Dahlquist, F. W., and Lindorfer, M. A. (1991) ²H Nuclear magnetic resonance of the gramicidin-A backbone in a phospholipid bilayer. *Biochemistry* **30**, 4687–4696.
63. Hing, A. W., Adams, S. P., Silbert, D. F., and Norberg, R. E. (1990) Deuterium NMR of Val1...(2-2H)Ala3...gramicidin A in oriented DMPC bilayers. *Biochemistry* **29**, 4144–4156.

64. Hing, A. W., Adams, S. P., Silbert, D. F., and Norberg, R. E. (1990) Deuterium NMR of ^2HCO -Val1...gramicidin A and ^2HCO -Val1-D-Leu2...gramicidin-A in oriented DMPC bilayers. *Biochemistry* **29**, 4156–4166.
65. He, K., Ludtke, S. J., Wu, Y., and Huang, H. W. (1993) X-ray scattering with momentum transfer in the plane of membrane. Application to gramicidin organization. *Biophys. J.* **64**, 157–162.
66. Wallace, B. A. (1986) Structure of gramicidin A. *Biophys. J.* **49**, 295–306.
67. Wallace, B. A., and Ravikumar, K. (1988) The gramicidin pore: crystal structure of a cesium complex. *Science* **241**, 182–187.
68. Langs, D. A. (1988) 3-Dimensional structure at 0.86 Å of the uncomplexed form of the transmembrane ion channel peptide gramicidin A. *Science* **241**, 188–191.
69. Thompson, D. H., Kim, J.-M., and Di Meglio, C. (1993) Photoinduced charge transfer of bolaamphiphile membrane-gramicidin diad composites. In *Organic and Biological Optoelectronics*, *SPIE* **1853**, 142–147.

CHAPTER 2

SYNTHESIS

2.1 Introduction

In 1854, Virchow [1] was able to visualize, through the use of light microscopy, “myelin figures” similar to biological cell membranes. These structures are now referred to as bilayer lipid membranes (BLMs). In the 1960s, BLMs forming vesicle membranes were developed [2] which defined inner and outer aqueous pools. Since that time, BLMs have been the subject of thousands of manuscripts which vary in realm from the physical properties (i.e., phase behavior, transport of ions) to their use in biochemical studies (i.e., drug delivery, membrane protein reconstitution). More recently, another class of lipids has been attracted the interest of researchers. These lipids differ from the bilayer-forming lipids in that the headgroups which project towards the inner and outer aqueous pools are covalently attached through a membrane-spanning hydrophobic linker and are called bolaamphiphiles [3]. A “bola” refers to the configuration of a South American hunting weapon which has, in its minimal form, two weighted ends connected by a tether, and is thrown in order to entangle the hunter’s quarry. The analogous lipid structure has a form of two hydrophilic headgroups coupled by two chains linked via ether linkages to a glycerol backbone, forming a macrocyclic amphiphile or a single long chain joining the glycerol backbones which also each have a short chain (Figure 2.1). These bolaamphiphile lipids form monolayer lipid membranes (MLMs). MLMs give chemotropic archaebacteria (such as *Sulfolobus solfataricus*) the ability to live in extreme environments of high temperature and low pH such as those encountered in sulfur-rich, sub-marine volcanic vents. Studies of the naturally

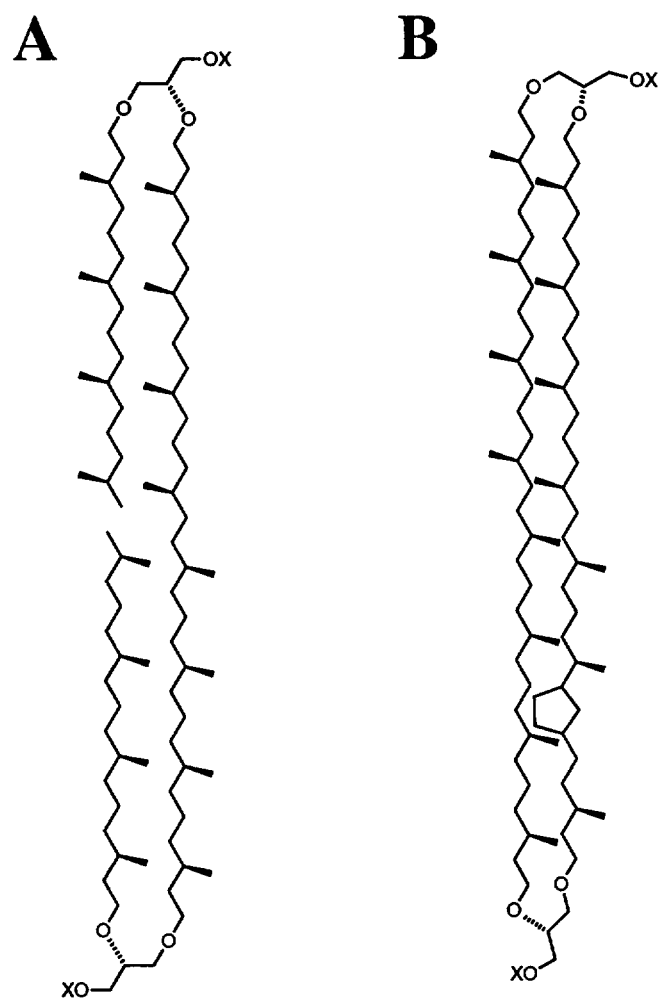


Figure 2.1 The basic structure of naturally occurring bolaamphiphiles. (A) acyclic; (B) macrocyclic. The headgroups X are either alcohol or saccharide.

occurring lipids [4] have generated interest in the synthesis of bolaamphiphile lipids with a variety of headgroups, backbones and linkages to membrane-spanning chains.

Okahata and Kunitake reported the first synthetic bolaamphiphiles in 1979 [5]. Baumgartner and Führop followed in 1980 with a report of another synthetic bolaamphiphile [6]. Since then more than a hundred different bolaamphiphiles have been made in the Führop laboratory [7]. A major interest of Führop has been the synthesis of many different types of macrocyclic bolaamphiphiles which self-assemble into membranes. These bolamphiphiles may have either cationic, anionic or neutral headgroups as well as combinations of the different headgroups [8]. Moreover, through the attachment of reactive headgroups, membrane functionality can be incorporated as in the case with N,N'-dialkyl-4,4'-dipyridinium dications [6,9] as well as the case where a quinone moiety has been attached to a bolaamphiphile [10]. Variations of headgroup size give vesicle membranes with large headgroups which prefer to face outside and small headgroups aimed towards the inside [11]. Other variations to the molecular structure of bolaamphiphiles made in Führop's group have been on the membrane spanning hydrophobic region (i.e., saturated hydrocarbon chains [12], rigid polyene chains [13]) as well as the types of linkages which connect the chains to the backbone or directly to the headgroup (e.g., ester, ether, amide).

Several synthetic acyclic bolaamphiphiles have been made in the laboratory of Yamauchi and coworkers [14]. Particularly interesting were acyclic bolaamphiphiles which possessed phosphocholine headgroups that gave sheetlike MLMs when sonicated, but formed closed liposomes when mixed with cholesterol or dipalmitoylphosphatidylcholine [5,14,15]. This behavior is based upon geometrical considerations which are discussed in Chapter 3. Other acyclic bolaamphiphiles were prepared by Moss and coworkers [16].

The bolaamphiphiles prepared in the Thompson laboratory are of the acyclic type [17]. Work for this dissertation included the synthesis of this type of bolaamphiphile [18].

The following sections describe the instruments and methodology used in the catalyst comparison, the total chiral synthesis of the bolaamphiphiles and enantiomeric excess determinations of the related chiral compounds, and the partial synthetic route

of racemic bolaamphiphiles. The goal of the synthetic work was to develop efficient synthetic methods for the components of a vesicle-based model for photoinduced electron transfer across thin vesicle membranes coupled to ion translocation.

2.2 Instruments

^1H NMR spectra were recorded on JEOL FX-90Q and GE QE-300 and Nicolet 500-MHz spectrometers with 5-mm probes using CDCl_3 as solvent and tetramethylsilane as internal standard unless otherwise noted. A Perkin Elmer 1800 FT-IR and VG Analytical 7070 E were used for infrared spectroscopy and FAB-MS, respectively. Centrifugal layer chromatography was performed on a Chromatotron from Harrison Research.

All yields reported are for isolated products (>95% pure). Product purification was typically performed by column chromatography using Baker silica gel 70–230 mesh. Similar results were also obtained using 4-mm Chromatotron plates coated with EM Science silica gel 60. Thin layer chromatography was performed using Baker-flex silica gel IB-F. Melting points were determined on a Mel-Temp II capillary melting point apparatus and are corrected. Boiling points are uncorrected.

2.3 Materials

Solvents and reagents were purified by recrystallization or distillation from desiccant unless otherwise noted. Cumene hydroperoxide was dried over 4 Å molecular sieves for at least 2 h prior to use. Methylene chloride, chloroform, and triethylamine were distilled from P_2O_5 . Titanium isopropoxide ($\text{Ti}(\text{O}i\text{Pr})_4$) and the tartrate esters were distilled from dry, powdered 3 Å molecular sieves. Boron trifluoride etherate and phosphorus oxychloride were distilled and stored under an inert atmosphere in reagent storage bottles with a glass stopcock and septum inlet. Triflic anhydride was prepared by P_2O_5 dehydration of triflic acid [19,20] and distilled twice from P_2O_5 before use. 1,8-Bis(dimethylamino)naphthalene, 4-(dimethylamino)pyridine (DMAP), and 3-nitrobenzenesulfonyl chloride were

recrystallized from diethyl ether. Triphenylmethyl chloride and *p*-toluenesulfonyl chloride were recrystallized from petroleum ether. The following reagents were used as received from Aldrich (except where noted): (2*S*)-glycidyl-3-nitrobenzenesulfonate, 1-tetradecanol, 1-hexadecanol, 1-octadecanol, 1-eicosanol (Sigma), 1,16-hexadecanediol, 1,20-eicosanedioic acid (American Tokyo Kasei), lithium aluminum hydride (Baker), toluenesulfonic acid, tropylium tetrafluoroborate, triflic acid (3M), 40% tetrabutylammonium hydroxide, cesium acetate, trimethylamine, 1,3-dioxo-2-chloro-2-phospholane (Fluka), and silica gel (EM Science).

Catalyst efficiency comparison

The purpose of this comparison was to determine a suitable catalyst for the ring opening of (R)-oxiranemethanol 3-nitrobenzenesulfonate **1(R)** with a long-chain alcohol (Figure 2.2). A stock solution was prepared by combining (R)-oxiranemethanol 3-nitrobenzenesulfonate **1(R)** (0.375 g, 1.45 mmol), 1-tetradecanol (0.372 g, 1.74 mmol), and *p*-xylene (internal standard; 0.108 mg, 1.02 mmol) into a 25-mL volumetric flask and diluting to volume with CDCl₃ (distilled from P₂O₅). Seven 5-mm NMR tubes were prepared with the following acid catalysts: DDQ (8.5 mg), triflic acid (32.5 μL), boron trifluoride etherate (32.5 μL), cesium fluoride (2.9 mg), tropylium tetrafluoroborate (1.3 mg), magnesium chloride (1.8 mg), or toluenesulfonic acid (0.4 mg). An eighth tube was catalyst-free to serve as a control. Aliquots of the stock solution were transferred by syringe (3.25 mL) to each NMR tube; the tubes were sealed, placed in a 60°C oil bath, and periodically withdrawn for spectral analysis over a 38-h reaction time. The ¹H NMR spectra (see Appendix) were analyzed by comparing the α-methylene integrals of tetradecanol and/or 3-*O*-tetradecyl-*sn*-glycerol 1-(3'-nitrobenzene)sulfonate **4** (after normalizing to the *p*-xylene CH₃ integral) and calculating the product concentration at various time points. As a first approximation, the rates of starting material disappearances and product appearance were assumed to be equal.

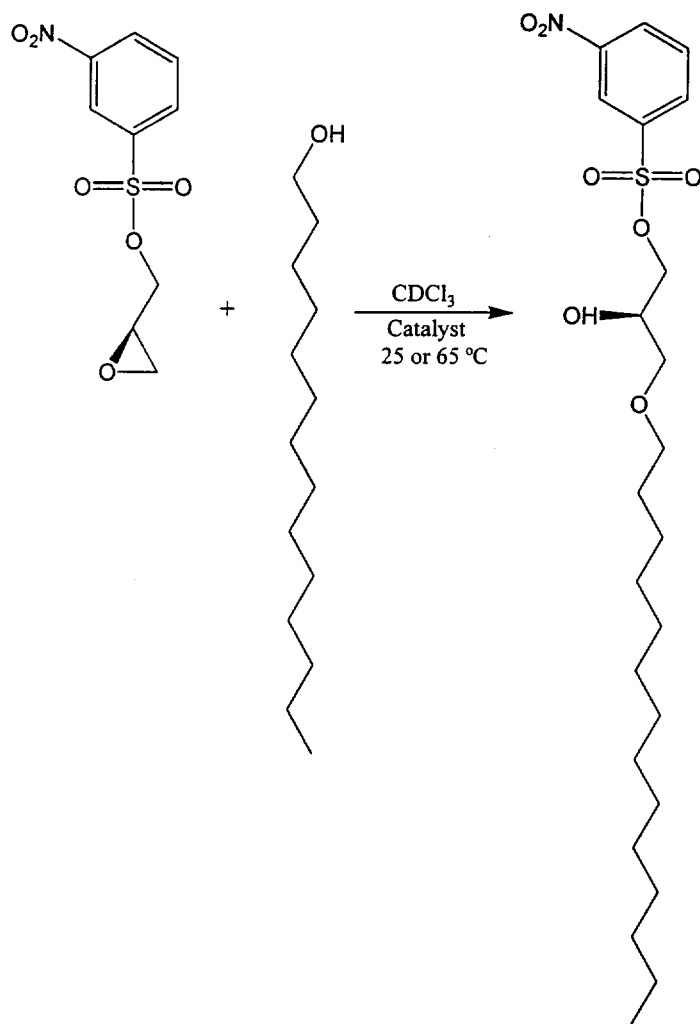


Figure 2.2 Reaction scheme to determine a suitable catalyst for the ring opening of R-oxiranemethanol 3-nitrobenzenesulfonate **1(R)** with a long-chain alcohol. The reaction was monitored by proton NMR.

In a more direct comparison, experiments were performed using identical concentrations of **1(R)**, 1-tetradecanol, and *p*-xylene in CDCl₃ as previously described; solutions of triflic acid, boron trifluoride etherate, tropylium tetrafluoroborate, and toluene sulfonic acid were added as 25 μL CDCl₃ solutions to 3.0-mL aliquots of the stock solutions to give catalyst concentrations of 10 mol%. Two series of experiments were conducted, at 25°C and at 65°C. These experiments were monitored with time and the data were analyzed. From this comparison it was found that the catalysts were all able to catalyze the epoxide ring opening reaction satisfactorily. Triflic acid was chosen for our reactions due to ease of handling, rapid reaction rate, and overall efficiency.

2.4 Synthesis of Chiral Ether Lipids

This section focuses on the synthetic methods used in the development of an efficient route to chiral bolaamphiphiles (Figure 2.3).

(R)-Oxiranemethanol 3-nitrobenzenesulfonate (1(R)) [21–26]

Powdered 3 Å molecular sieves (7.2 g) were weighed into a flask fitted with a septum, vacuum adapter, and addition funnel, and flame dried under vacuum. The flask was charged with methylene chloride (380 mL), allyl alcohol (13.6 mL, 200 mmol), L-diisopropyl tartrate (L-DIPT; 2.8 mL, 13.3 mmol), and cooled to -5°C under dry argon. Ti(O*i*Pr)₄ (3.1 mL, 10.4 mmol) was then added, the catalyst cured for 1.5 h before addition of 80% cumene hydroperoxide (80 mL, 433 mmol) over a 30-min period, and the temperature maintained at -5°C. After 8 h, the reaction mixture was cooled to -38°C and the remaining hydroperoxide quenched by slow addition of trimethyl phosphite TMP; (38 mL, 322 mmol). Triethylamine (39 mL, 278 mmol), DMAP (2.74 g, 22 mmol), and 3-nitrobenzenesulfonyl chloride (44.32 g, 200 mmol) were then added and the reaction mixture held at 0°C. After 12 h, the suspension was filtered through Celite and the filtrate washed with 10% tartaric acid (100 mL), saturated NaHCO₃ (150 mL), brine (100 mL), and dried over MgSO₄. The solvent was removed by rotary evaporation and the product concentrated by

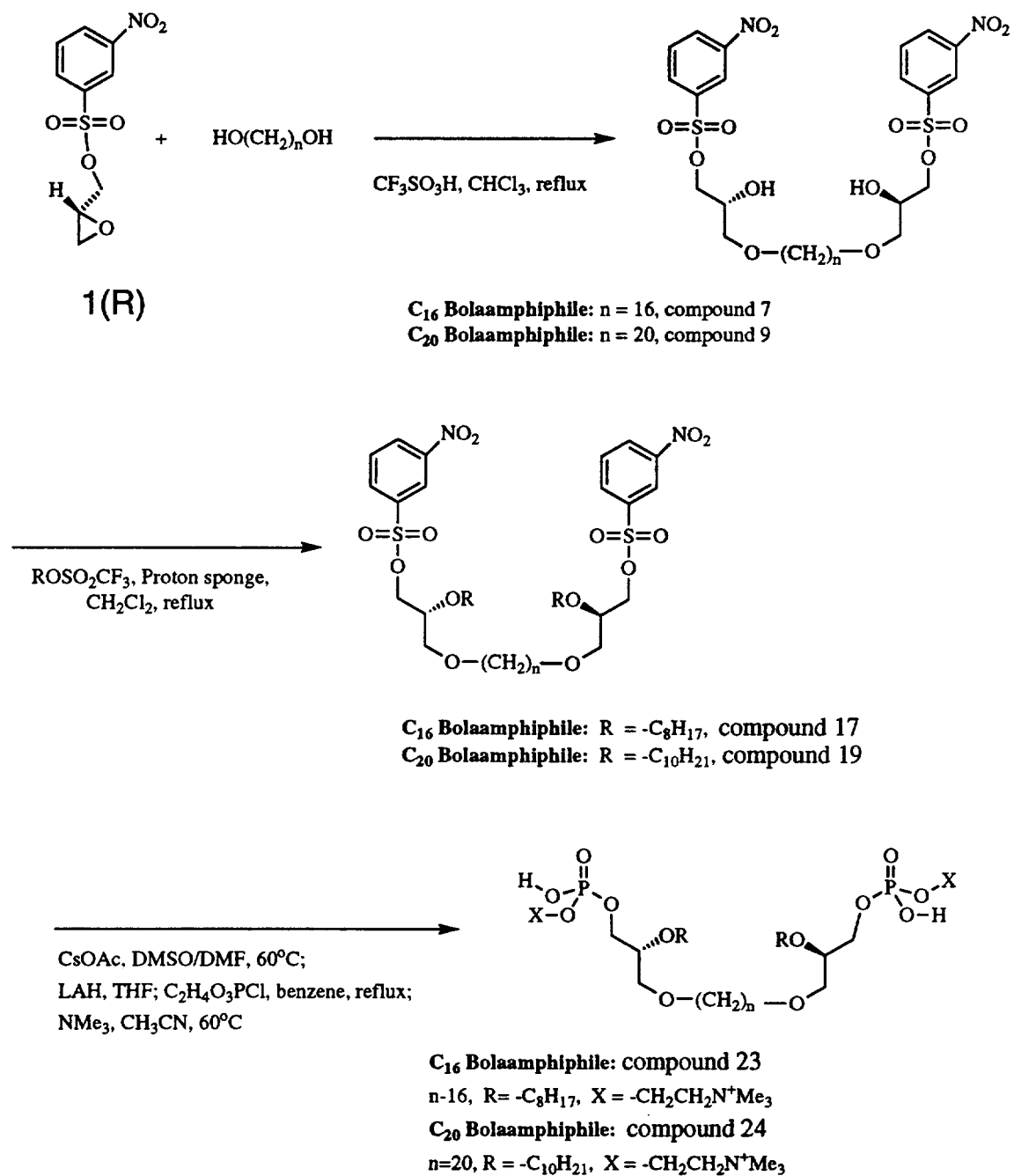


Figure 2.3 Sequence in the synthesis of C16 and C20 bolaamphiphiles.

vacuum distillation at 1 μ to remove cumyl alcohol. The remaining dense yellow oil was purified by column chromatography to give **1(R)** (17.27 g after recrystallization from diethyl ether, 33% yield). TLC: $R_f = 0.25$, CH_2Cl_2 . MP: 61°C.

3-O-Hexadecyl-*sn*-glycerol 1-(3'-nitrobenzene)sulfonate (2) [27]

1-Hexadecanol (14.03 g, 57.9 mmol) and **1(R)** (5.0 g, 19.3 mmol) were combined in a 5-mL flask fitted with a CaCl_2 drying tube. The solids were heated to 65°C \pm 5°C with vigorous stirring to emulsify the phase-separated melt prior to addition of triflic acid (100 μL). After 5 h, the reaction mixture was cooled, dissolved in 30 mL CH_2Cl_2 , filtered through a 1" plug of silica gel, evaporated under reduced pressure, and isolated by flash column chromatography using 3:1 hexane:ethyl acetate as eluant to give 7.65 g of **2** (79% yield). TLC: $R_f = 0.18$, 3:1 hexane:ethyl acetate. MP: 58°C. ^1H NMR: 8.78 (s, 1H, 2'-*H*), 8.53 (d, 1H, 6'-*H*), 8.28 (d, 1H, 4'-*H*), 7.81 (t, 1H, 5'-*H*), 4.20 (dd, 2H, CH_2OSO_2), 4.01 (m, 1H, glycerol methine *H*), 3.47 (t, 2H, OCH_2R), 3.42 (t, 2H, $\text{OCHCH}_2\text{OCH}_2\text{R}$), 2.19 (br s, 1H, *OH*), 1.52 (m, 2H, $\text{OCH}_2\text{CH}_2\text{R}$), 1.27 (br s, 26H, polymethylene *H*'s), 0.89 (t, 3H, CH_3). ^{13}C NMR: 133.5, 131.5, 128.0, 123.4, 72.2 ($\text{CH}_2\text{OSO}_2\text{Ar}$), 72.0 (OCHCH_2OR), 70.8 ($\text{OCHCH}_2\text{OCH}_2\text{R}$), 68.2 (OCHCH_2OR), 32.3, 29.8, 29.6, 29.4, 29.2, 26.3, 23.1, 14.2; Mosher ester ^1H NMR 8.57 (d, $J = 8$ Hz, 1H), 8.20 (d, $J = 8$ Hz, 1H), 7.88 (s, 1H), 7.77 (s, 1H), 7.73-7.31 (m, 5H), 5.42 (s, 1H), 4.42 (dd, $J_{\text{AC}} = 2.9$ Hz, $J_{\text{AB}} = 11$ Hz, 1H) 4.35 (dd, $J_{\text{AB}} = 11$ Hz, $J_{\text{BC}} = 7.3$ Hz, 1H), 3.25-2.87 (m, 7H), 1.44 (m, 2H), 1.28 (m, 28H), 0.90 (t, $J = 7$ Hz, 3H).

1-O-Hexadecyl-*sn*-glycerol 3-(3'-nitrobenzene)sulfonate (3) [26]

1-Hexadecanol (2.51 g, 10.4 mmol) and **1(S)** (1.057 g, 4.08 mmol) were treated as for **2** and isolated by Chromatotron using 3:1 hexane:ethyl acetate to give **3** (1.60 g, 3.19 mmol, 78% yield). $\geq 99\%$ ee by NMR of Mosher ester; 98.3% ee by HPLC): Mosher ester ^1H NMR 8.48 (d, $J = 8$ Hz, 1H), 8.07 (d, $J = 8$ Hz, 1H), 7.85 (br s, 1H), 7.44 (m, 5H), 5.42 (s, 1H), 4.35 (dd, $J_{\text{AC}} = 3$ Hz, $J_{\text{AB}} = 11$ Hz,

1H), 4.25 (dd, $J_{AB} = 11$ Hz, $J_{BC} = 7$ Hz, 1H), 3.54 (m, 7H), 1.50 (m, 2H), 1.26 (m, 28H), 0.88 (t, $J = 7$ Hz, 3H).

3-*O*-Tetradecyl-*sn*-glycerol 1-(3'-nitrobenzene)sulfonate (4)

1(R) (1.36 g, 5.25 mmol) and 1-tetradecanol (3.38 g, 15.8 mmol) gave **4** in 83% yield (2.06 g, 4.35 mmol; $\geq 99\%$ ee by NMR of Mosher ester) using the procedure described for **2**. TLC: $R_f = 0.12$, 3:1 hexane:ethyl acetate. MP: 41°C; Mosher ester ^1H NMR 8.46 (d, $J = 7$ Hz, 1H), 7.95 (br s, 1H), 7.77 (t, $J = 7$ Hz, 1H), 7.43 (m, 5H), 5.41 (s, 1H), 4.42 (dd, $J_{AC} = 3$ Hz, $J_{AB} = 11$ Hz, 1H), 4.35 (dd, $J_{BC} = 7$ Hz, $J_{AB} = 11$ Hz, 1H), 3.44 (m, 7H), 1.42 (s, 2H), 1.26 (m, 24H), 0.88 (t, $J = 7$ Hz, 3H).

3-*O*-Octadecyl-*sn*-glycerol-1-(3'-nitrobenzene)sulfonate (5)

5 (1.88 g, 35.5 mmol, 75% yield) was obtained from 1-octadecanol as described for **2** ($\geq 99\%$ ee by NMR of Mosher ester): TLC: $R_f = 0.16$, 3:1 hexane:ethyl acetate. MP: 65°C. Mosher ester ^1H NMR 8.52 (br s, 1H), 8.19 (br s, 1H), 7.74 (br s, 1H), 7.43 (m, 5H), 5.42 (br s, 1H), 4.40 (br d, $J = 11$ Hz, 2H), 3.25–3.77 (m, 7H), 1.44 (br s, 2H), 1.27 (br s, 32H), 0.90 (br s, 3H).

3-*O*-Eicosyl-*sn*-glycerol 1-(3'-nitrobenzene)sulfonate (6)

A procedure similar to that described for **2** was used except that 1-eicosanol (3.45 g, 11.6 mmol) and **1(R)** (1.00 g, 3.86 mmol) were heated for 19 h to give **6** (1.47 g, 2.63 mmol, 68% yield). TLC: $R_f = 0.14$, 3:1 hexane:ethyl acetate. MP: 70°C; Mosher ester ^1H NMR 8.51 (br s, 2H), 8.19 (br s, 1H), 7.77 (s, 1H), 7.73–7.31 (m, 5H), 5.41 (s, 1H), 4.39 (m, 1H), 4.35 (m, 1H), 3.22–3.87 (m, 7H), 1.44 (m, 2H), 1.28 (m, 36H), 0.89 (t, $J = 7$ Hz, 3H).

3,3'-Di-*O*-hexadecamethylenedi-*sn*-glycerol 1,1'-bis(3'-nitrobenzene)sulfonate (7)

1(R) and 1,16-hexadecanediol were dissolved in dry chloroform followed by triflic acid addition by microliter syringe. The reaction mixture was heated at reflux

for ~48 h before filtration through a 1" plug of silica gel. The filtrate was evaporated and chromatographed using 9:1 CHCl₃:acetone to give pure **7**. ¹H NMR: 8.78 (s, 2H), 8.56 (d, 2H), 8.31 (d, 2H), 7.80 (t, 2H), 4.20 (m, 4H), 4.05 (m, 2H), 3.42 (m, 4H), 2.4 (d, 2H), 1.58 (m, 4H), 1.27 (br s, 24H); Mosher ester ¹H NMR 8.52 (br s, 2H), 8.22 (br s, 2H), 7.98 (br s, 2H), 7.80 (br s, 2H), 7.25–7.73 (m, 10H), 5.42 (br s, 2H), 4.43 (dd, $J_{AC} = 3$ Hz, $J_{AB} = 11$ Hz, $J_{BC} = 7$ Hz, 2H), 3.90–3.15 (m, 14H), 1.45 (m, 4H), 1.27 (m, 24H).

1,1'-Di-*O*-hexadecamethylenedi-*sn*-glycerol 3,3'-bis(3'-nitrobenzene)sulfonate (8)

This was prepared as described for **7**, except **1(S)** was used as substrate.

3,3'-Di-*O*-eicosamethylenedi-*sn*-glycerol 1,1'-bis(3'-nitrobenzene)sulfonate (9)

This was prepared as described for **7**, except 1,20-eicosanediol was used as substrate. ¹H NMR: 8.75 (s, 2H), 8.54 (d, 2H), 8.29 (d, 2H), 7.78 (t, 2H), 4.18 (m, 4H), 3.99 (m, 2H), 3.39 (m, 4H), 2.42 (d, 2H), 1.58 (m, 4H) 1.27 (br s, 32H); Mosher ester ¹H NMR 8.52 (d, $J = 7$ Hz, 2H), 8.19 (d, $J = 8$ Hz, 2H), 7.98 (d, $J = 7$ Hz, 2H), 7.77 (d, $J = 8$ Hz, 2H), 7.49 (m, 10H), 5.42 (br s, 2H), 4.43 (dd, $J_{AC} = 3$ Hz, $J_{AB} = 11$ Hz, 2H), 4.35 (dd, $J_{BC} = 7$ Hz, $J_{AB} = 11$ Hz, 2H), 3.48 (m, 14H), 1.43 (m, 4H), 1.27 (m, 36H).

1,1'-Di-*O*-eicosamethylenedi-*sn*-glycerol 3,3'-di(3'-nitrobenzene)sulfonate (10)

This was prepared as described for **7**, except **1(S)** was used as substrate.

Alkyl triflates

Triflate esters of 1-hexanol, 1-octanol, 1-tetradecanol, 1-hexadecanol, 1-octadecanol, and 1-eicosanol were prepared as described by Aoki and Poulter [28]. The triflate ester products were dissolved in pentane and purified by filtration through a 1" plug of silica gel. The purified products were stored as pentane solutions (< C₁₆) or as solids at 5°C (after evaporation for ≥ C₁₆) prior to use.

2,3-Di-*O*-hexadecyl-*sn*-glycerol 1-(3'-nitrobenzene)sulfonate (11)

Alcohol **2** (0.617 g, 1.23 mmol), 1,8-bis(dimethylamino)naphthalene (0.418 g, 1.95 mmol), hexadecyl triflate (0.731 g, 1.95 mmol), and 5 mL dichloromethane were included in a 10-mL round bottom flask. The solution was heated at reflux for 5 days, although little additional conversion of **2** to **11** occurred after the first 2 days. When no further reaction progress was detected by TLC, the orange suspension was evaporated to dryness (after addition of HCl to protonate the excess base), triturated with ether, and the ether solution filtered through a 1" plug of silica gel to remove low R_f impurities. The eluant was evaporated and the product isolated by Chromatotron using 2:1 hexane:ethyl acetate to give **11** (0.797 g, 1.10 mmol, 89% yield). TLC: R_f = 0.70, 2:1 hexane:ethyl acetate. ^1H NMR: 8.80 (s, 1H), 8.53 (d, 1H), 8.25 (d, 1H), 7.80 (t, 1H), 4.30–4.15 (m, 2H), 3.65 (m, 1H), 3.5–3.3 (m, 6H), 1.45 (m, 4H), 1.25 (m, 52H), 0.85 (t, 6H). ^{13}C NMR: 148.3, 138.3, 133.8, 130.9, 128.1, 123.5, 76.6 (CHOCH₂OR), 72.1 (ArSO₃CH₂), 71.6 (CHOCH₂R), 70.8 (CHOCH₂OR), 68.7 (CH₂OCH₂CH₂R), 32.3, 30.1, 29.8, 29.6, 29.4, 26.6, 26.5, 22.8, 14.6. Pirkle phase HPLC indicated that no scrambling of the *sn*-2 chirality occurred during alkylation. When the same reaction was run in refluxing chloroform, the reaction time was reduced to 2.5 days to give **11** in 84% yield.

1,2-Di-*O*-hexadecyl-*sn*-glycerol 3-(3'-nitrobenzene)sulfonate (12)

12 was prepared as described for **11** (CH₂Cl₂), except that **3** (1.556 g, 3.10 mmol) was heated for 2 days with hexadecyl triflate (2.32 g, 6.20 mmol) to give 2.072 g **12** (92% yield).

2,3-Di-*O*-tetradecyl-*sn*-glycerol 1-(3'-nitrobenzene)sulfonate (13)

4 (0.198 g, 0.42 mmol), 1,8-bis(dimethylamino)naphthalene (0.223 g, 1.04 mmol), and tetradecyl triflate (0.463 g, 1.33 mmol) were heated for 48 h in CH₂Cl₂ and isolated as in **11** to give **13** (0.249 g, 3.72 mmol, 89% yield). ^1H NMR: 8.80 (s, 1H), 8.52 (d, 1H), 8.28 (d, 1H), 7.80 (t, 1H), 4.38–4.15 (m, 2H), 3.67 (m, 1H), 3.6–3.35 (m, 6H), 1.30 (m, 48H), 0.90 (t, 6H).

2,3-Di-*O*-octadecyl-*sn*-glycerol 1-(3'-nitrobenzene)sulfonate (14)

14 was prepared in 92% yield as described for **11** (CH₂Cl₂), except the reaction time was 48 h. TLC: R_f = 0.65, 2:1 hexane:ethyl acetate.

2,3-Di-*O*-eicosyl-*sn*-glycerol 1-(3'-nitrobenzene)sulfonate (15)

6 (1.114 g, 2.00 mmol) and eicosyl triflate (1.72 g, 3.99 mmol) were heated with 1,8-bis(dimethylamino)naphthalene (0.857 g, 4.00 mmol) in CH₂Cl₂ for 46 h to give **15** (1.517 g, 1.81 mmol, 91% yield).

2,2'-Di-*O*-octyl-3,3'-di-*O*-hexadecamethylenedi-*sn*-glycerol 1,1'-bis(3'-nitrobenzene)sulfonate (16)

1,8-Bis(dimethylamino)naphthalene, octyl triflate and **7** in chloroform were heated at reflux for 48 h. The reaction mixture was then filtered and chromatographed as for **11**. ¹H NMR: 8.89 (s, 2H), 8.63 (d, 2H), 8.37 (d, 2H), 7.89 (t, 2H), 4.47–4.16 (m, –CH₂OSO₂), 3.67–3.60 (m, 2H, methine *H*'s), 3.53–3.33 (m, 12H, α-methylenes and glycerol *H*'s), 1.47 (m, 8H, β-methylenes), 1.29 (s, 44H, aliphatic methylenes), 0.89 (t, 6H, ω-CH₃).

2,2'-Di-*O*-octyl-1,1'-*O*-hexadecamethylenedi-*sn*-glycerol 3,3'-bis(3'-nitrobenzene)sulfonate (17)

This was prepared as for **16** above, except **8** was used in the alkylation reaction. ¹H NMR 8.82 (s, 2H), 8.59 (d, 2H), 8.30 (d, 2H), 7.85(t, 2H), 4.38–4.20 (m, 6H), 1.32 (s, 44H), 0.92 (t, 6H).

2-*O*-Hexadecyl-3,3'-*O*-hexadecamethylene-di-*sn*-glycerol 1,1'-bis(3'-nitrobenzenesulfonate) (18)

7, hexadecyl triflate (1.1 eq), and 1,8-bis(dimethylamino)naphthalene were heated at reflux in chloroform as described for **16**. ¹H NMR: 8.89 (s, 2H), 8.64 (d, 2H), 8.37 (d, 2H), 7.89 (t, 2H), 4.35–4.12 (m, 4H, –CH₂OSO₂), 3.68–3.60 (m, 2H,

methine *H*'s), 3.53–3.32 (m, 7.3H, α -methylenes and glycerol *H*'s), 1.47 (m, 4H, β -methylenes), 1.29 (s, 64H, aliphatic and β -methylene *H*'s), 0.89 (t, 6H, ω -CH₃).

2,2'-Di-*O*-decyl-3,3'-*O*-eicosamethylenedi-*sn*-glycerol 1,1'-bis(3'-nitrobenzene-sulfonate) (19)

The procedure was similar to that described for **16**, except **17** was used as substrate. ¹H NMR: 8.89 (s, 2H), 8.61 (d, 2H), 8.34 (d, 2H), 7.87 (t, 2H), 4.39–4.13 (m, 4H), 3.68 (m, 2H), 3.55–3.34 (m, 10H), 1.47 (m, 4H), 1.26 (s, 60H), 0.87 (t, 6H).

2,2'-Di-*O*-octyl-1,1'-*O*-hexadecamethylenedi-*sn*-glycerol 1,1'-diacetate (20)

17 (250 mg, 0.226 mmol) was dissolved in 1 mL of 4:1 DMSO:DMF. Cesium acetate (659 mg, 3.43 mmol) was added and the system heated to 60°C overnight [27]. The solvent was removed by vacuum distillation and the residue was dissolved in chloroform before filtration. The solvent from the filtrate was removed by rotary evaporation giving **20** in 82% yield. *R*_f = 0.71 in 5:2 Et₂O:hexane.

2,2'-Di-*O*-decyl-3,3'-*O*-eicosamethylenedi-*sn*-glycerol 1,1'-diacetate (21)

19 was dissolved in 2 mL of 4:1 DMSO:DMF. Cesium acetate (4.280 g, 22.3 mmol) was added and the system heated to 65°C overnight [27]. The solvent was removed by vacuum distillation and the residue was dissolved in chloroform before filtration. The solvent from the filtrate was removed by rotary evaporation giving **21** in 89% yield. *R*_f = 0.75 in 5:2 Et₂O:hexane.

2,2'-Di-*O*-octyl-1,1'-*O*-hexadecamethylenedi-*sn*-glycerol 1,1'-diol (22)

20 (150 mg, 0.179 mmol) was dissolved in anhydrous THF. LAH (15 mg, 0.394 mmol) was added, and the system heated to reflux with stirring overnight. The reaction was quenched with water, the aluminum salt removed by filtration and the residue evaporated. The residue was dissolved in 3:2 Et₂O:hexane, filtered through a 1" plug of silica gel, and the product isolated on a 2-mm Chromatotron plate using

3:2 diethyl ether:hexane as eluant. 60% yield, $R_f = 0.16$. $^1\text{H NMR}$: 3.76–3.40 (m, 18H), 1.65 (p, 10H), 1.40–1.25 (s, 60H), 0.89 (t, 6H).

2,2'-Di-*O*-octyl-3,3'-*O*-hexadecamethylenedi-*sn*-glycerol 1,1'-diol (22)

17 (0.444 g, 0.444 mmol) was treated with 20 equivalents of benzylalkoxy lithium in THF (10 mL) heated at reflux for 18 h; hydrogenolysis of the benzyl protected bolaamphiphile (0.161 g, 0.196 mmol) was effected using 120 psi H_2 and 5% Pd/C (8 mg) at 100°C for 12 h. The tetraether diol product was isolated by filtration through a plug of Celite, followed by evaporation and chromatography on silica gel using 3:1 hexane:ethyl acetate. $^1\text{H NMR}$: 4.47–4.16 (m, 8H, $\text{CH}_2\text{OPOCH}_2$), 3.97 (m, 4H, $2\text{CH}_2\text{N}$), 3.67–3.60 (m, 2H, methine *H*'s), 3.53–3.33 (m, 12H, α -methylenes and glycerol *H*'s), 3.25 (s, 18H, $2\text{N}(\text{CH}_3)_3$), 1.47 (m, 8H, β -methylenes), 1.29 (s, 44H, aliphatic methylenes), 0.89 (t, 6H, $\omega\text{-CH}_3$).

2,2'-Di-*O*-octyl-3,3'-*O*-hexadecamethylenedi-*sn*-glycerol 1,1'-diphosphocholine (23)
[14b]

The tetraether diol 22 (73 mg, 0.10 mmol) was lyophilized and dissolved at 0°C in 5 mL of benzene containing Et_3N (103 mg, 1.02 mmol) and 2-chloro-2-oxo-1,3,2-diphospholane (93 mg, 1.02 mmol). The ice bath was removed and the system stirred for 36 h at room temperature prior to removal of the Et_3NHCl salt by filtration and rotary evaporation of the filtrate. The residue was dissolved in CH_3CN (5 mL) and the CH_3CN solution transferred to a 20-mL pressure tube, cooled in dry ice/acetone, and charged with freshly distilled, anhydrous Me_3N (1 mL). The system was then sealed and heated to 65°C with stirring for 48 h; a white solid precipitated as the reaction proceeded. The system was cooled and the volatile components were removed under vacuum. The residue was dissolved in 2:1 chloroform:methanol (25 mL) and washed with water. The organic layer was concentrated and purified by column chromatography using 8:6:4:3 (v/v) chloroform:acetone:methanol: NH_4OH to give a colorless solid (90 mg, 82% yield): $R_f = 0.37$, 8:6:4:3 (v/v) chloroform:acetone:methanol: NH_4OH : $^1\text{H NMR}$: 4.47–4.16 (m, 8H, $\text{CH}_2\text{OPOCH}_2$), 3.97 (m, 4H, $2\text{CH}_2\text{N}$), 3.67–3.60 (m, 2H,

methine *H*'s), 3.53–3.33 (m, 12H, α -methylenes and glycerol *H*'s), 3.25 (s, 18H, 2N(CH₃)₃), 1.47 (m, 8H, β -methylenes), 1.29 (s, 44H, aliphatic methylenes), 0.89 (t, 6H, ω -CH₃).

2,2'-Di-*O*-decyl-3,3'-*O*-eicosamethylenedi-*sn*-glycerol 1,1'-diphosphocholine (24)
[14b]

24 was phosphorylated as in the procedure described for 23. ¹H NMR: 4.39–4.13 (m, 8H), 3.97 (m, 4H), 3.68 (m, 2H), 3.55–3.34 (m, 10H), 3.25 (s, 18H), 1.47 (m, 4H), 1.26 (s, 60H), 0.87 (t, 6H).

2.5 Partial Route to Racemic Bolaamphiphiles

Synthesis of 1,1'-*O*-hexadecamethylenedi-*rac*-solketal (25)

Solketal (2.9 g, 93.7 mmol) was dissolved in 300 mL of tetrahydrofuran. NaH (3.75 g, 93.7 mmol) was added as a 60% dispersion in mineral oil with stirring. H₂ gas evolved for 30 min. 1,16-Dibromohexadecane (15.61 mmol) was dissolved in tetrahydrofuran and added to the reaction mixture. The system was heated at reflux for 2 days. After cooling, the solvent was removed by rotary evaporation. The residue was dissolved in dichloromethane and washed with 300 mL water. The dichloromethane solution was then dried over anhydrous sodium sulfate. The solution was filtered and stripped to dryness by rotary evaporation. The residue was dissolved in 10 mL of dichloromethane and purified by silica gel column chromatography eluting with 1 L dichloromethane followed by 10% acetone/90% dichloromethane. The fractions were monitored by TLC. The solvent from the fraction-containing product was removed by rotary evaporation to give the product as colorless crystals (4.3 g, 8.8 mmol) in 57% yield. ¹H NMR (CDCl₃) 1.27 (s, 24H, (CH₂)₁₂), 1.36 (s, 6H, acetonide CH₃), 1.41 (s, 6H, acetonide CH₃), 1.56 (t, 4H, OCCH₂), 3.17 (m, 8H, OCH₂OCH₂), 3.73 (dd, 2H, CH₂O), 4.06 (dd, 2H, CH₂O), 4.26 (p, 2H, CHO).

1,1'-*O*-hexadecamethylenedi-*rac*-glycerol (26)

26 was obtained by hydrolysis of **25** (4.2 g, 8.6 mmol) with 5 mL of H₂O and 7 mL of concentrated HCl in 300 mL of methanol and heated at reflux for 2 days. The solvent was removed by rotary evaporation and the residue was redissolved in dichloromethane before drying over anhydrous sodium sulfate. The solution was filtered, the solvent removed by rotary evaporation, and the product recrystallized from ethyl acetate to afford colorless crystals (1.7 g, 4.2 mmol). MP: 87°C. ¹H NMR (DMSO-*d*₆) 1.26 (s, 24H, (CH₂)₁₂), 1.54 (t, 4H, (OCCH₂)₂), 3.42–3.52 (m, 12H, OCHCH₂OCH₂), 3.58 (m, 2H, OCH₂).

3,3'-Di-*O*-(triphenylmethyl)-1,1'-*O*-hexadecamethylenedi-*rac*-glycerol (27)

27 was obtained by dissolving **26** (1.7 g, 4.2 mmol), 4-dimethylaminopyridine (0.082 mmol) and pyridine (2.4 g, 30.3 mmol) in 130 mL of dry tetrahydrofuran and treating it with trityl chloride (12.0 g, 43 mmol) dissolved in a minimum amount of dry tetrahydrofuran. After heating at reflux for three days (a yellowish-brown color was noted after 1 day of reflux), the reaction was quenched by cooling, filtered, and the solvent removed by rotary evaporation. The residue was redissolved in dichloromethane and washed with water. The organic phase was dried over anhydrous sodium sulfate, filtered, and rotary evaporated. R_f = 0 components were removed by filtering a dichloromethane solution through alumina.

1,20-Eicosanediol (28)

28 was synthesized by dissolving 1,18-eicosanedioic acid (7.10 g, 20.7 mmol) in 400 mL of anhydrous tetrahydrofuran (the solution was added dropwise to LiAlH₄; 2.0 g, 0.052 mmol) and the mixture heated at reflux for 2 days. Progress of the reaction was monitored by TLC. The reaction was quenched by acidification with HCl, and the solution extracted with CHCl₃. The extract was dried over anhydrous magnesium sulfate, filtered, and the solvent removed by rotary evaporation. The residue was recrystallized from benzene to yield colorless amorphous powder (6.11 g, 19.7 mmol; 95% yield). R_f = 0.4 in 1:1 hexane:ethyl acetate (1:1). MP: 95°C. ¹H NMR(CDCl₃) 1.27 (s, 34H, (OH₂ and(CH₂)₁₆), 1.57 (p, 4H, OCCH₂), 3.64 (t, 4H, CH₂O).

1,20-Dibromoeicosane (29)

29 was synthesized by heating **28** in 100 mL of 30% HBr in acetic acid. The system was heated to reflux for 24 h. The TLC indicated the absence of starting material. The system was cooled to room temperature, and the liquid layer was decanted. The remaining dark brown solid was dissolved in CHCl_3 and was washed with water until pH of the water was neutral. **29** was isolated by column chromatography eluting with hexane. $R_f = 0.5$ in hexane. 8.2 g (19.5 mmol) was obtained as colorless crystals (70.5% yield). MP: 63°C. $^1\text{H NMR}$ (CDCl_3) 1.25 (s, 28H, $(\text{CH}_2)_{14}$), 1.41 (t, 4H, $\gamma\text{-CH}_2$), 1.85 (p, 4H, $\beta\text{-CH}_2$), 3.41 (t, 4H, CH_2Br)

1,1'-*O*-Eicosamethylenedi-rac-solketal (30)

30 was synthesized by dissolving solketal (19.7 g, 149 mmol) in 250 mL of anhydrous tetrahydrofuran, NaH (6.0 g, 150 mmol) added as a 60% dispersion in mineral oil and upon completion of hydrogen gas evolution, **29** (8.2 g, 19.5 mmol) added prior to heating the reaction mixture at reflux for 4 days. After cooling, the dark yellow mixture was filtered through silica gel and the filtrate was concentrated by rotary evaporation. The crude product was obtained by column chromatography using dichloromethane as eluant, followed by recrystallization from methanol. The material was then rechromatographed using a silica gel column eluting with dichloromethane to give **30** (1.10 g, 2.02 mmol, 10.3% yield). $R_f = 0.7$ in CH_2Cl_2 . MP: 57°C. $^1\text{H NMR}$ 1.27 (s, 32H, $(\text{CH}_2)_{16}$), 1.36 (s, 6H, acetonide CH_3), 1.42 (s, 6H, acetonide CH_3), 1.57 (t, 4H, OCCH_2), 3.50 (m, 8H, OCH_2OCH_2), 3.74 (dd, 2H, CH_2O), 4.08 (dd, 2H, CH_2O), 4.29 (p, 2H, CHO).

1,1'-*O*-Eicosamethylenedi-rac-glycerol (31)

31 was synthesized by dissolving **30** (0.72 g, 1.32 mmol) in 20 mL of warm methanol, 2.15 mL of 7 M HCl added (dropwise) and the mixture heated at gentle reflux for two days. The reaction was quenched by cooling to give colorless crystals. After filtration, the crystals were washed with water, extracted with CHCl_3/THF and the extract dried over sodium sulfate and filtered. The filtrate was stripped by rotary evaporation. The material was recrystallized from ethyl acetate to give colorless crystals

(0.61 g, 1.12 mmol, 85% yield). $R_f = 0.6$ in THF. MP: 100°C. $^1\text{H NMR}$ 1.25 (s, 32H, $(\text{CH}_2)_{16}$), 1.6 (t, 4H, $(\text{OCCH}_2)_2$), 3.2 (d, 8H), 3.3–3.6 (m, 8H), 4.0 (p, 2H, OCH_2).

3,3-Di'-O-(triphenylmethyl)-1,1'-O-eicosamethylenedi-rac-glycerol (32)

31 (100 mg, 0.216 mmol) and trityl chloride (181 mg, 0.648 mmol) were contained in an airlessware flask; 5.0 mL of pyridine (anhydrous) was added to the flask and the mixture stirred. AgBF_4 (140 mg, 0.648 mmol) was weighed into an airlessware flask and dissolved in 1 mL of pyridine. The AgBF_4 solution was added dropwise, under argon, to the reactants and the system was heated at 45°C for three days in the dark. After pyridine removal by rotary evaporation, the residue was washed with water, extracted with dichloromethane, dried over anhydrous sodium sulfate and filtered. Evaporation gave a product with an $R_f = 0.3$ in dichloromethane.

2.6 Synthesis of Porphyrin and Gramicidin A–Porphyrin Diad

The porphyrin and the derivatized gramicidin ion channel were obtained from Dr. Jong-Mok Kim. 5-(4'-Chlorobenzoyl)-10,15,20-tris(4'-methylphenyl)porphyrin [29] (**33**) was prepared in a condensation reaction of *p*-tolualdehyde and terephthalaldehydic acid methyl ester and pyridine in propionic acid/acetic anhydride. The desformylgramicidin A was prepared, according to the literature procedures, from hydrolysis of gramicidin A using anhydrous HCl in methanol [30]. The desformylgramicidin A and the 5-(4'-chlorobenzoyl)-10,15,20-tris(4'-methylphenyl)porphyrin (**34**) were esterified in a coupling reaction using diphenylphosphorylazide in dimethylformamide.

2.7 References

1. Virchow, R. (1854) *Virchows Archiv für Pathologische Anatomie und Physiologie und für Klinische Medizin*, Vol. 6, p. 571.
2. Bangham, A. D., Standish, M. M., and Watkins, J. C. (1965) Diffusion of univalent ions across the lamellae of swollen phospholipids. *J. Mol. Biol.* **13**, 238-252.
3. (a) Zana, R., Yiv, S., and Kale, K. M. (1980) Chemical relaxation and equilibrium studies of association in aqueous solutions of bolaform detergents. 3. Docosane-1,22-bis(trimethylammonium bromide). *J. Colloid Interface Sci.* **77**, 456-465.
(b) Menger, F. M., and Wrenn, S. (1974) Interfacial and micellar properties of bolaform electrolytes. *J. Phys. Chem.* **78**, 1387-1390.
(c) Kachar, B., Evans, D. F., and Ninham, B. W. (1984) Video enhanced differential interference contrast microscopy: A new tool for the study of association colloids and prebiotic assemblies. *J. Colloid Interface Sci.* **100**, 287-301.
4. (a) Gliozzi, A., Rolandi, R., De Rosa, M., and Gambacorta, A. (1983) Monolayer black membranes from bipolar lipids of archaebacteria and their temperature-induced structural changes. *J. Membr. Biol.* **75**, 45-56.
(b) Gliozzi, A., Paoli, G., Rolandi, R., De Rosa, M., and Gambacorta, A. (1982) Structure and transport properties of artificial bipolar lipid membranes. *Bioelectrochem. Bioenerg.* **9**, 591-601.
(c) Gulik, A., Luzzati, V., De Rosa, M., Gambacorta, A. (1985) Structure and polymorphism of bipolar isopranyl ether lipids from archaebacteria. *J. Mol. Biol.* **182**, 131-149.
5. Okahata, Y., and Kunitake, T. (1979) Formation of stable monolayer membranes and related structures in dilute aqueous solution from two-headed ammonium amphiphiles. *J. Am. Chem. Soc.* **101**, 5231-5234.
6. Baumgartner, E., and Führop J.-H. (1980) Vesicles with a monolayer, redox-active membrane. *Angew. Chem. Int. Ed. Engl.* **19**, 550-551.
7. Führop, J.-H., and Detlev, F. (1986) Bolaamphiphiles form ultrathin, porous and unsymmetric monolayer lipid membranes. *Acc. Chem. Res.* **19**, 130-137, and references therein.
8. Führop, J.-H., and Bach, R. (1992) Monolayer lipid membranes (MLMs) from bolaamphiphiles. *Adv. Supramol. Chem.* **2**, 25-63.

9. Führhop, J.-H., Fritsch, D., Tesche, B., and Schmiady, H. (1984) Water-soluble α,ω -bis(paraquat) amphiphiles form monolayer membrane vesicles, micelles, and crystals by stepwise anion exchange or photochemical reduction. *J. Am. Chem. Soc.* **106**, 1998–2001.
10. Führhop, J.-H., Hungerbühler, H., and Siggel, U. (1990) Quinone-containing amphiphiles and bolaform amphiphiles that form redox-active lipid membranes. *Langmuir* **6**, 1295–1300.
11. Führhop, J.-H., and Mathieu, J. (1983) An unsymmetric monolayer vesicle membrane. *Chem. Commun.* 144–145.
12. Führhop, J.-H., David, H. H., Mathieu, J., Liman, U., Winter, H.-J., and Boekema, E. (1986) Bolaamphiphiles and monolayer lipid membranes made from 1,6,19,24-tetraoxa-3,21-cyclohexatriacontadiene-2,5,20,23-tetrone. *J. Am. Chem. Soc.* **108**, 1785–1791.
13. Führhop, J.-H., Krull, M., Schulz, A., and Möbius, D. (1990) Bolaform amphiphiles with a rigid hydrophobic bixin core in surface monolayers and lipid membranes. *Langmuir* **6**, 497–505.
14. (a) Yamauchi, K., Sakamoto, Y., Moriya, A., Yamada, K., Hosokawa, T., Higuchi, T., and Kinoshita, M. (1990) Archaeobacterial lipid models. Highly thermostable membranes from 1,1'-(1,32-dotriacontamethylene)-bis(2-phytanil-sn-glycero-3-phosphocholine). *J. Am. Chem. Soc.* **112**, 3188-3191.
(b) Yamauchi, K., Moriya, A., and Kinoshita, M. (1989) Peculiar membrane morphologies of archaeobacterial lipid models: 1,1'-polymethylenebis(2-alkyl-sn-glycero-3-phosphocholine). *Biochim. Biophys. Acta* **1003**, 151-160.
15. Führhop, J.-H., and Mathieu (1984) Routes to functional vesicle membranes without proteins. *Angew. Chem. Int. Ed. Engl.* **23**, 100-113.
16. (a) Moss, R. A., and Fujita, T. (1990) Proton/hydroxide permeation across ammonium ion bilayer vesicles detected by self-indicating head groups. *Tetrahedron Lett.* **31**, 2377-2380.
(b) Moss, R. A., and Fujita, T., and Okumura, Y. (1991) Effect of unsaturation on lipid dynamics within synthetic lipid membranes. *Langmuir* **7**, 2415–2418.
17. (a) Kim, J.-M., and Thompson, D. H. (1992) Tetraether bolaform amphiphiles as models of archaeobacterial membrane lipids: Synthesis, differential scanning calorimetry, and monolayer studies. *Langmuir* **8**, 637-644.
(b) Thompson, D. H., and Kim, J.-M. (1992) Photoinduced charge transfer studies in bolaamphiphile-gramicidin-porphyrin membranes. *MRS Symp.* "Macromolecular Host-Guest Complexes: Optical and Optoelectronic Properties and Applications" **277**, 93-98.

18. Thompson, D. H., Svendsen, C. B., Di Meglio, C., and Anderson, V. C. (1994) Synthesis of chiral diether and tetraether phospholipids-regiospecific ring-opening of epoxy alcohol intermediates derived from asymmetric epoxidation. *J. Org. Chem.* **59**, 2945–2955.
19. Eguchi, T., Arakawa, K., Terachi, T., and Kakinuma, K. (1997) Total synthesis of achaeal 36-membered macrocyclic diether lipid. *J. Org. Chem.* **62**, 1924–1933.
20. Burdon, J., Farazmand, I., Stacey, M., and Tatlow, J. C. (1957) Fluorinated sulfonic acids. I. Perfluoromethane-, octatane-, and -decanesulfonic acids and their simple derivatives. *J. Chem. Soc.* 2574–2578.
21. Gao, Y., Hanson, R. M., Klunder, J. M., Ko, S. Y., Masamune, H., and Sharpless, K. B. (1987) Catalytic asymmetric epoxidation and kinetic resolution-modified procedures including *in situ* derivatization. *J. Am. Chem. Soc.* **109**, 5765–5780.
22. Klunder, J. M., Onami, T., and Sharpless, K. B. (1989) Arenesulfonate derivatives of homochiral glycidol—versatile chiral building-blocks for organic-synthesis. *J. Org. Chem.* **54**, 1295–1304.
23. Woodard, S. S., Finn, M. G., and Sharpless, K. B. (1991) Mechanism of asymmetric epoxidation. 1. Kinetics. *J. Am. Chem. Soc.* **113**, 106–113.
24. Finn, M. G., and Sharpless, K. B. (1991) Mechanism of asymmetric epoxidation. 2. Catalyst structure. *J. Am. Chem. Soc.* **113**, 113–126.
25. Carlier, P. R., and Sharpless, K. B. (1989) Studies on the mechanism of the asymmetric epoxidation—a ligand variation approach. *J. Org. Chem.* **54**, 4016–4018.
26. Burns, C. J., Martin, C. A., and Sharpless, K. B. (1989) Tartrate-like ligands in the asymmetric epoxidation. *J. Org. Chem.* **54**, 2826–2834.
27. Guivisdalsky, P. N., and Bittman, R. (1989) An efficient stereocontrolled route to both enantiomers of platelet activating factor and analogs with long-chain esters at C2-saturated and unsaturated ether glycerolipids by opening of glycidyl arenesulfonates. *J. Org. Chem.* **54**, 4643–4648.
28. Aoki, T., and Poulter, C. D. (1985) Archaeobacterial isoprenoids. Synthesis of 2,3-di-*O*-phytanil-*sn*-glycerol and its 1,2-isomer. *J. Org. Chem.* **50**, 5634–5636.

29. Gust, D., Moore, T. A., Liddel, P. A., Nemeth, G. A., Makings, L. R., Moore, A. L., Barrett, D., Pessiki, P. J., Bensasson, R. V., Rougée, M., Chachaty, C., De Schryver, F. C., Van der Auweraer, M., Holzwarth, A. R., and Connolly, J. S. (1987) Charge separation in carotenoporphyrin-quinone triads: Synthetic, conformational, and fluorescence lifetime studies. *J. Am. Chem. Soc.* **109**, 846–856.
30. Stankovic, C. J., Delfino, J. M., and Schreiber, S. L. (1990) Purification of gramicidin A. *Anal. Biochem.* **184**, 100–103.

CHAPTER 3

PHYSICAL CHARACTERIZATION OF BOLAAMPHIPHILE PHASES

The section which follows put the novel bolaamphiphiles through a battery of experiments in order to test their suitability for use as a photoconversion host matrix. Experiments were conducted to determine what physical conditions would be required for these material to enter into a vesicle phase characterized by a lipid membrane surrounding an inner aqueous volume. The early sections describe the physical characterization experiments to determine such parameters. The experimental protocols for differential scanning calorimetry, the surface pressure measurements, and small angle X-ray scattering spectroscopy are also described.

3.1 Differential Scanning Calorimetry

Hydrated lipid aggregates exhibit a variety of phases whose occurrence depends on the molecular structure, temperature, pressure, water content and cosurfactant/solute concentrations [1]. The aggregation process of hydrated phospholipids is partially driven by the hydrophobic effect, which maximizes the entropy of the system by minimizing the amount of water which must be ordered around the hydrocarbon chains. Counteracting this hydrophobic interaction are repulsive electrostatic interactions (i.e., ionic, dipolar, and multipolar) between the lipid headgroups. Since water concentration and temperature both affect the identity of the stable phase, these systems display both lyotropic and thermotropic polymorphism. These terms refer to the fact that phase transitions can be induced by varying either the water concentration or the temperature of the system. Transitions of the lamellar phase are of particular interest since they establish the functional phase

space of biomembranes and vesicle bilayers. The predominant transitions in bilayer-forming lipids involve alkyl chain-melting and headgroup dehydration processes that give rise to the gel-lamellar phase transition and the transition to lamellar-hexagonal phase transition. In the gel phase, the hydrocarbon chains are crystalline, while in the lamellar and hexagonal phases they are more disordered and fluid. Thus, the fundamental transition in phospholipids is the chain-melting transition involving gel-to-lamellar hexagonal phases. The driving force for the chain-melting transition is the increase in configurational entropy of the hydrophobic chains with increasing temperature; this produces a two-dimensional fluid lamellar phase such as those found in biomembranes. The driving force for non-lamellar phase transitions is the non-zero spontaneous curvature of the bilayer caused by conformational and/or hydration changes of the hydrophilic headgroup [2]. Under suitable conditions of temperature and mol% water, vesicles are formed by these liquid crystalline phases.

3.1.1 Chain-melting transition

The chain-melting transition occurs due to increasing entropy which results from chain rotational disorder, in addition to increased headgroup hydration and intermolecular entropy. Increased conformational freedom at the chain-melting transition leads to (i) increases in the internal energy, (ii) increases in hydrophobic exposure to water, and (iii) a decrease in van der Waals attraction between the chains [3]. Both the increase in rotational isomerization and the decrease in van der Waals interactions depend directly upon chain length. The total enthalpy, ΔH_t , can be approximated by the contributions of both the van der Waals interactions and the *trans-gauche* isomerizations by the following relationship:

$$\Delta H_t = \Delta H_{inc} (n - n_o) \quad (3.1)$$

where n is the phospholipid chain length, n_o is the constant effective chain length arising from headgroup interactions and hydration, and ΔH_{inc} is the incremental transition enthalpy per methylene group. Similarly, the total transition entropy can be related by the relationship:

$$\Delta S_t = \Delta S_{inc} (n - n_o) \quad (3.2)$$

where ΔS_{inc} is the incremental transition entropy. These incremental thermodynamic contributions represent about half of those observed for isotropic melts of corresponding hydrocarbons and indicate that the rotational disorder is considerably less in lipid aggregates, while the chain packing is enhanced as compared to the molten isotropic hydrocarbons as understood from ^2H NMR experiments of specifically deuterated phospholipids [4]. This implies that the hydrocarbons are more ordered in lipid aggregates.

The transition temperature dependence upon chain length is given by:

$$T_t = T_t^\infty [1 - (n_o - n'_o) / (n - n'_o)] \quad (3.3)$$

where $T_t^\infty = \Delta H_{inc} / \Delta S_{inc}$ and represents the transition temperature when it is extrapolated to a system with an infinite chain length. Phospholipids obey this relation, with the observation of a large, initial dependence upon chain length which diminishes with increasing chain length, as the end (headgroup) effects are weighted less (Figure 3.1).

It was important to compare the phase behavior of the novel bolaamphiphiles (Chap. 2) with the behavior of well-understood systems in order to determine the temperature regime over which lamellar phases exist as the sole or predominate phase. The phase transition temperatures of the C20 and C16 bolaamphiphiles were determined by differential scanning calorimetry (DSC).

3.1.2 Instrumental

The calorimeter supplies the sample with a steady, known amount of electrically produced heat while a thermocouple monitors the changing temperature. During the phase transition, the heat which previously resulted in sample temperature change is absorbed by the lipid. The differential change in heat capacity during a phase transition is marked by a corresponding increase in electrical current flow to the sample in order to preserve the prescribed temperature ramp rate. The current flow is plotted with respect to temperature, yielding a DSC thermogram with the phase transition temperature reported by an abrupt deviation from the baseline. In the following experiments, differential scanning calorimetry was performed on a Perkin-Elmer DSC-7 and a TAC7/PC instrument controller interfaced to an IBM PS/2 Model

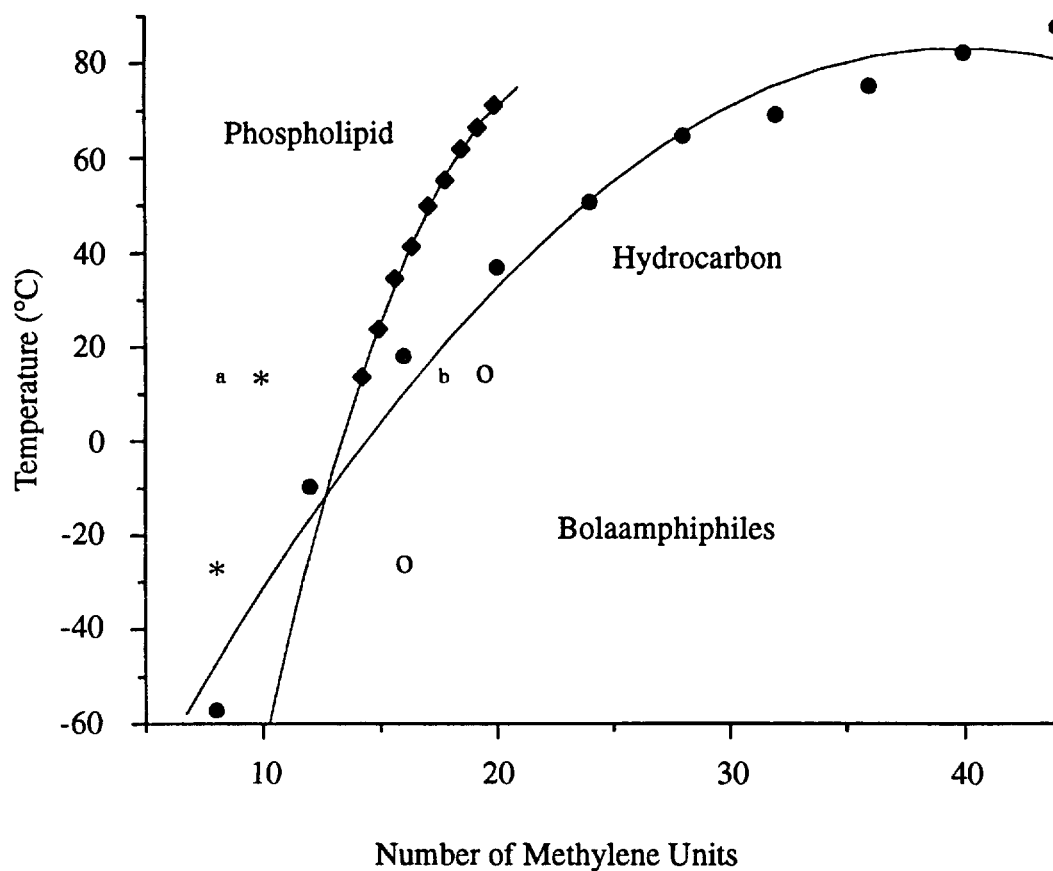


Figure 3.1 Plot of the gel-to-lamellar-phase transition temperature as a function of hydrocarbon chain length. (a) Considering the shorter chain length. (b) Considering the longer chain length.

Table 3.1 Curve Fitting Parameters for Phase Transition Data Appearing in Figure 3.1

Material	Coefficients from $y = Cx^2 + BX + A$		
	A	B	C
PC lipids	-198	22	-0.4
Hydrocarbon	-120	10	-0.1

50 Z computer. Approximately 10 mg of lipid hydrated with 2 mg of water was analyzed in stainless steel pans using air as a reference.

3.1.3 Results

From the DSC experiments, phase transition temperatures were determined to be -27°C for C16 bolaamphiphiles and 12°C for C20 bolaamphiphiles as obtained from the onset temperature in the thermogram (Figures 3.2 and 3.3). The transition temperatures of the bolaamphiphile lipids, PC lipids and pure hydrocarbons were plotted as a function of the number of methylene groups. The phase transition temperatures of the bolas were included in the plot of chain length dependence vs. transition temperature in two ways. When the bolas were plotted according to their shorter chain, the bolaamphiphile lipids and biologically derived PC lipids (which form bilayers) demonstrate the predicted chain-melting transitions which are higher than for the corresponding hydrocarbons, indicating that they are more ordered than hydrocarbons. If the bolaamphiphiles were plotted according to their long chains, the data imply that the bolaamphiphiles are much less ordered than the phosphocholine lipids. Since the bolaamphiphile lipids are bipolar, there are two possible ways that they could self assemble into lamellar arrays. In one case, the bolaamphiphiles may assemble into a bilayer. In the second case they form a monolayer. A bilayer of bipolar lipids differs in architecture from naturally occurring phospholipids. Instead of the lipids aligning with a single headgroup per amphiphile facing away from the hydrocarbon region, the bolaamphiphiles would have two headgroups per molecule. This leads to the U-shaped configuration where the polar headgroups face the water phase, the long joining chain is bent in the air phase, and the two short chains extend into the air phase. The monolayer structure is the other possible mode into which the bolaamphiphiles could self-assemble. In this way a single molecule forms the lamella with the two headgroups occupying opposite interfaces with the long joining chain extended and not bent as in the U-shaped structure. Therefore, if we are to compare the bolaamphiphiles to naturally occurring phospholipids, it would be more reasonable to consider them as dimers of short alkyl chains rather than bilayer phosphocholines which have been coupled at the inter-monolayer region of the bilayer.

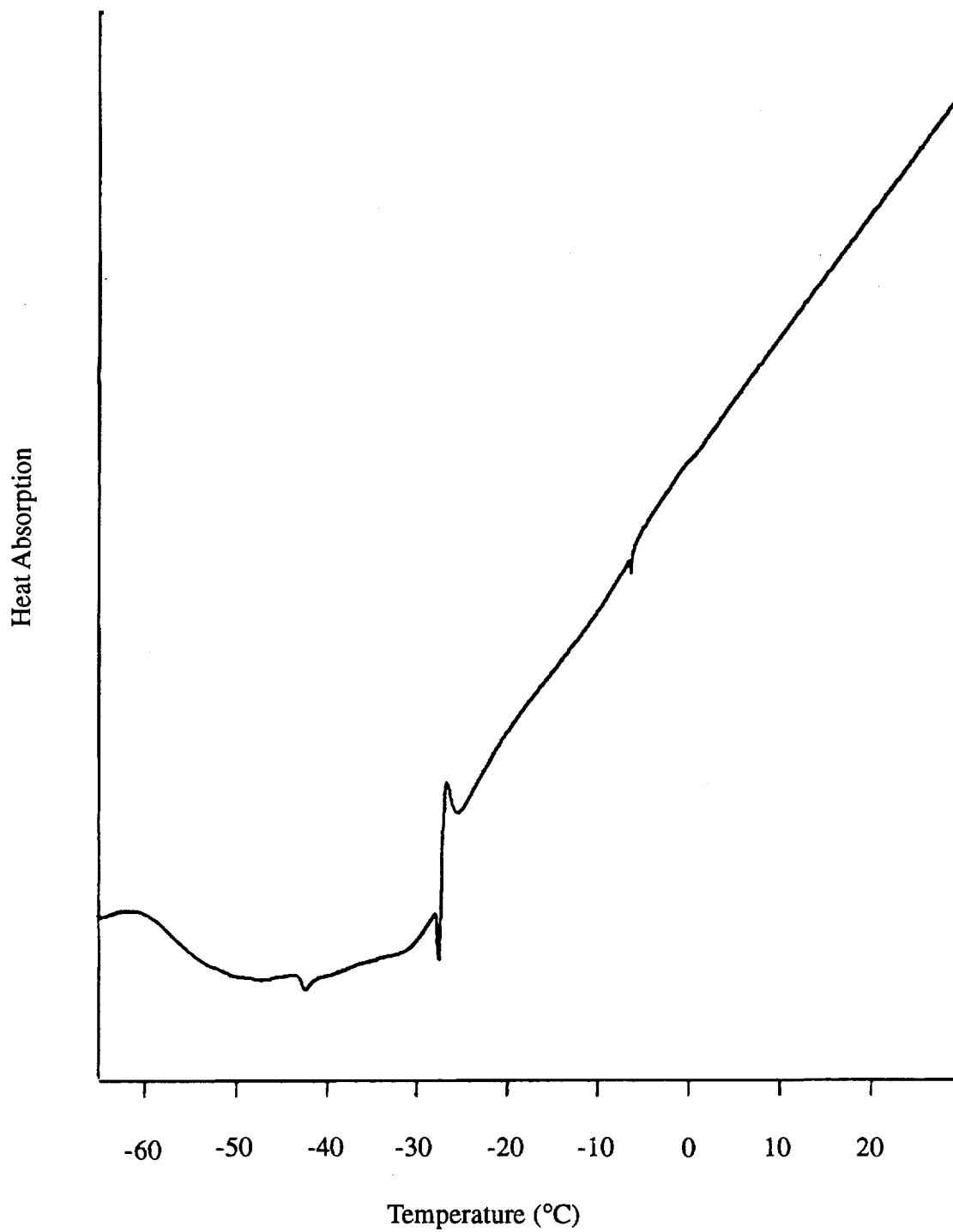


Figure 3.2 Differential scanning calorimetry thermogram of hydrated C16 bolaamphiphile.

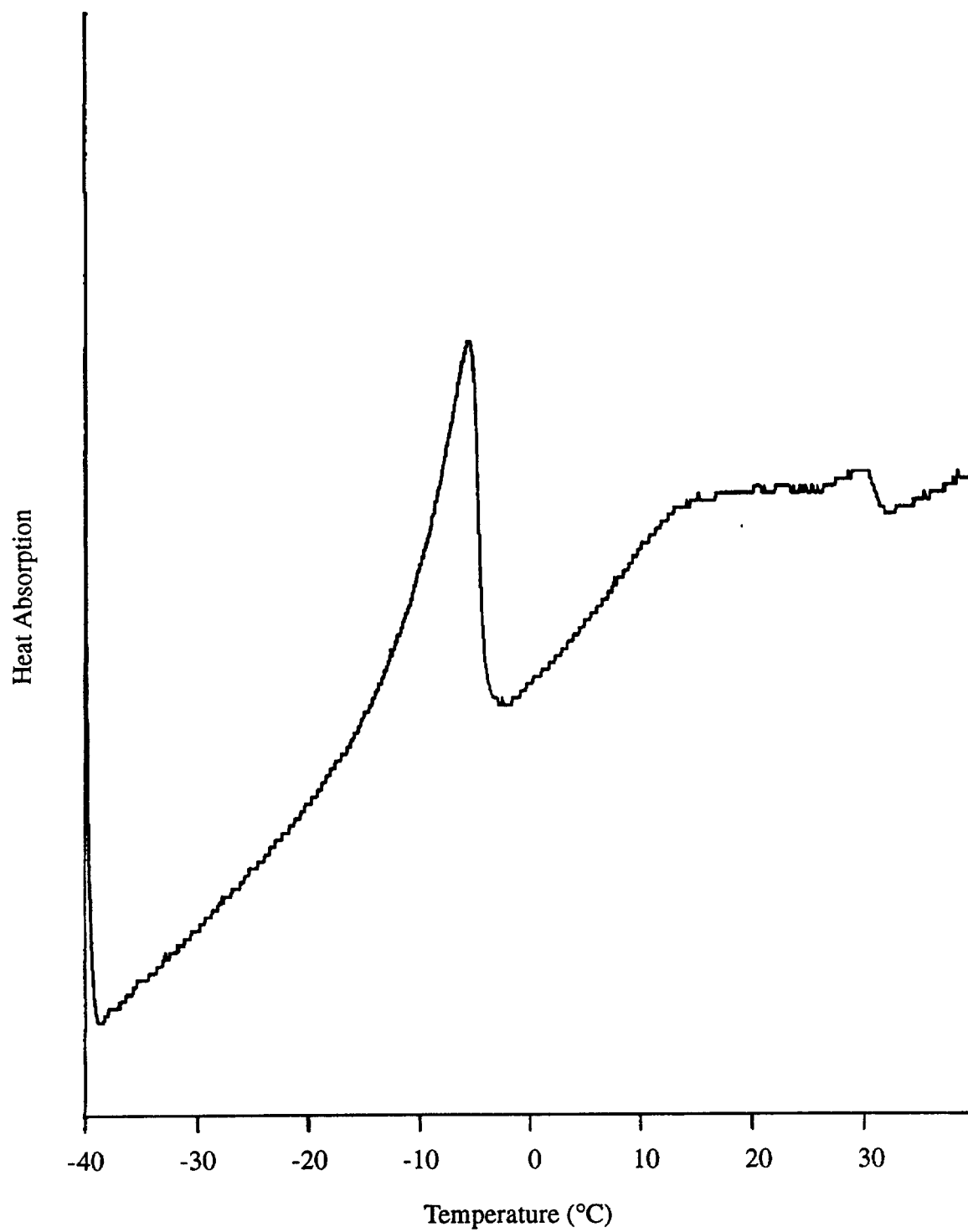


Figure 3.3 Differential scanning calorimetry thermogram of hydrated C20 bolaamphiphile.

By comparing the bolaamphiphiles to PCs (Figure 3.1), these materials appear to behave similarly to PC lipids based on chain length considerations, albeit with slightly higher-than-expected transition temperatures. This deviation from what would be extrapolated can be explained by the fact that there is a long aliphatic chain connecting the glycerophosphocholine headgroups. The behavior of the lipid falls closer to that expected for the short chains, presumably due to an influence on the long chain by the molten short chains.

The transition temperatures of the lipids were also compared to the melting points of pure hydrocarbons (Figure 3.1 and Table 3.1). In phospholipids, the phase transition temperatures are roughly twice those observed for pure hydrocarbons. This is consistent with the fact that each lipid possesses two hydrocarbon chains. Hence the change in one methylene unit corresponds to the addition of two methylene groups to the phospholipid. When considering the bolaamphiphiles (Figures 3.2 and 3.3), the transition temperatures are higher than those found in the phospholipids or the pure hydrocarbons. This difference can be attributed to many causes. One contribution could be an increase in transition enthalpy. Another factor could be a decrease in transition entropy. Based on the molecular architecture of the bolaamphiphile lipids, the entropic effect would seem to be of more importance. Whether monolayer or bilayer structure, the covalent bond in the long connecting chain (compared to natural phospholipids) introduces a higher degree of order due to restricted degrees of conformational freedom. Furthermore, for a membrane-spanning structure, the translational degrees of freedom are significantly reduced compared to a bilayer structure. From the data it cannot be surmised which assembly mechanism is in operation. Still, we expect that the reduced conformational and translational degrees of freedom in bolaamphiphile phases should result in decreased entropy at the gel-lamellar transition. The observed higher transition temperatures are, therefore, consistent with the reduced entropic contribution, i.e., higher degree of chain ordering. With the limited thermal data at hand, a more quantitative interpretation cannot be made. Further studies entailing chain length variation with careful measurements of the heats of transition are needed before any detailed quantitative interpretation can be made.

3.2 Small Angle X-ray Scattering Spectroscopy

The DSC studies presented in the previous section indicate the occurrence of lipid phase transitions; however, they do not indicate which phases are involved in the temperature-induced transition. Molecular packing considerations determine which of the equilibrium phase structures (i.e., lamellar/hexagonal/vesicle) are likely to be formed [5] (Figure 3.4). There are three important molecular shape parameters that are useful for predicting the occurrence of particular structures: V (molecular lipid volume), A_o (lipid cross sectional area perpendicular to the interface), and l_c (the molecular thickness). The critical packing parameter of an amphiphilic molecule is defined as $P = V/A_o l_c$. When $P = 1$, the optimal packing of amphiphilic molecules results in a planar lamellar structure. If $1/3 < P < 1/2$, then the wedge-shaped lipid structure prefers a hexagonal (H_I , tube-like) structure. For values of $P < 1/3$, a micellar structure is observed, whereas reversed hexagonal or reversed micelle structures (i.e., H_{II} phases) are formed when $P > 1$. The critical packing parameter P essentially describes the intrinsic or spontaneous curvature present in a dispersion of the amphiphile as a single component at thermodynamic equilibrium. Spontaneous curvature is zero when $P = 1$ (i.e., planar structure); however, curved equilibrium structures can be expected when $P \neq 1$. In addition to the predictive value of P , the observed changes in phase structure induced by changes in temperature or solution conditions can be qualitatively correlated to changes in amphiphile conformations, hydration, counterion, localization, etc. (Figure 3.4). The parameters are well understood for conventional diacyl and dialkyl lipids, including phospholipids, and their corresponding critical packing parameters; however, relatively little is known about the phase behavior of synthetic bolaamphiphiles. The critical packing parameters for the bolaamphiphiles whose synthesis is described in Chapter 2 should be equal to one if they adopt a membrane-spanning monolayer orientation, since the molecule is cylindrically symmetrical. Therefore we anticipate that lamellar structures should prevail in the phase diagram. These packing parameters (i.e., transmembrane thickness, cross-sectional areas, and phase structure of lyotropic

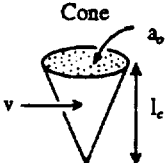
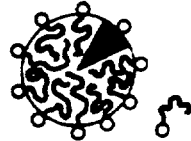
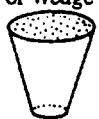


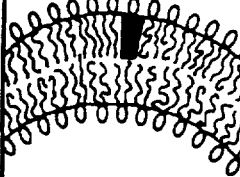

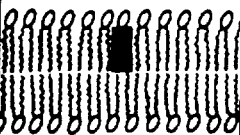

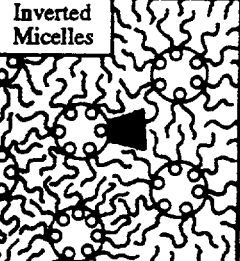
Lipid	Critical Packing Parameter $v/a_h l_c$	Critical Packing Shape	Structures Formed
Single chained lipids with large head group areas	$\frac{1}{3}$	Cone 	Spherical Micelles 
Single chained lipids with small head group areas	$\frac{1}{3}$ to $\frac{1}{2}$	Truncated Cone or Wedge 	Cylindrical Micelles 
Double chained lipids with large head groups and fluid chains	$\frac{1}{2}$ to 1	Truncated Cone 	Flexible Bilayers Vesicles 
Double chained lipids with small head group areas and fluid chains	-1	Cylinder 	Planar Bilayers 
Double chained lipids with small head group areas	>1	Inverted truncated cone or wedge 	Inverted Micelles 

Figure 3.4 Mean (dynamic) packing shapes and the structures which are formed.

systems) may be experimentally determined using X-ray diffraction [6] and compared with the predictions of the packing model.

Since phase behavior information does not exist for this new class of lipids, it was necessary to establish the binary phase diagrams of bolaamphiphiles in water. It was particularly essential to determine the thickness of the membrane lamellae, especially for the lamellar liquid crystalline phase, and for establishing the experimental boundaries of vesicle stability so that ion and electron transfer experiments can be conducted in that regime.

Prior to discussion of the X-ray results, it is instructive to summarize the thermodynamics and structural features observed in the binary phospholipid/water systems which are well described by Cevc and Marsh [7]. In such systems, the number of phases which may co-exist and the composition ranges which may co-exist can be predicted by the Gibbs phase rule. The phase rule is grounded in the thermodynamic precept that the chemical potential, μ_i^A , of each component i is the same in all the phases (A) at equilibrium. When the number of components is two, there are two degrees of freedom for a unique phase at constant pressure. Therefore, under limiting hydration, the phase may exist over a range of compositions and temperatures. When the number of phases is two, the system has one degree of freedom. Thus at a given composition, two phases may coexist over a range of temperatures; or at a given temperature, two coexisting phases could have a range of compositions. At a specific temperature and composition, the compositions and relative proportions of the two coexisting phases are fully determined. Three phases can possibly exist in equilibrium at constant temperature and composition when the system is invariant, and is referred to as the eutectic, peritectic, or monotectic point depending upon the qualities of the invariant transition. Generally, lyotropic transitions between single phases will occur by two co-existing phases, i.e., they are first-order phase transitions. The phases which may occur depend upon the packing fraction. When the lipid concentration is very low, the lipids are present as monomers which self-assemble at the critical micelle concentration (cmc) to form normal micelles (M_1). If the lipid concentration is increased, the system may undergo a transition, through a normal hexagonal phase (H_1), then finally to the lamellar phase

(L_α). Up to this point, the sequence would apply to amphiphiles possessing a single chain. Similarly, in phospholipids with two chains, the system may transform with further reduction in water concentration to an inverted hexagonal phase (H_{II}) and finally to an inverted micellar phase.

These phases can be easily distinguished by small angle X-ray scattering studies. The spherical structures of dilute micellar and vesicular solutions produce diffuse scattering patterns from which it is possible to determine the shape, size and structure of these particles. However, liquid crystalline phases scatter strongly and exhibit diffraction patterns characteristic of the underlying phase symmetry. In lamellar liquid crystalline phases, a series of diffraction peaks are observed which exhibit a simple linear periodicity. The separation for first-order peaks is exactly one half of that for the second-order peaks. Often it is possible to see even higher-order peaks. These peaks can be easily indexed such that the primary spacing reflects the interlayer repeat distance. This is established in the Bragg diffraction equation:

$$n\lambda = 2d \sin\theta \quad (3.4)$$

where n is the order of the reflection, λ is the X-ray wavelength and d is the lipid interlamellar distance (Figure 3.5). The angular position of the diffraction peak is defined by θ . θ is obtained by the relation:

$$\theta = 1/2 \tan^{-1} (S/L) \quad (3.5)$$

where S is the distance of the peak from the undiffracted beam (calibrated from lead stearate), and L is the distance of the sample from the detector. Thus for the lamellar structures the angular position, $\sin\theta$, varies linearly between the successive order of peaks. Therefore, the angular spacing for the diffraction peaks is in a 1:2:3 ratio for $n = 1, 2,$ and 3 . Gel-lamellar phases also exhibit this ratio. Higher-order peaks (i.e., $n > 1$) are generally observed in well-oriented plate samples. A sample loaded into a small X-ray capillary typically produces first-order diffraction peaks due to the lack of long-range order in such a geometry. This observation can be exploited to distinguish between gel and liquid crystalline lamellar phases.

The most characteristic feature of the hexagonal phase is tubelike cylinders arranged in a hexagonal lattice. This results in a diffraction pattern where the 1:2:3 periodicity ratio from the gel-lamellar phases changes to $1:\sqrt{3}:2$. The occurrence and

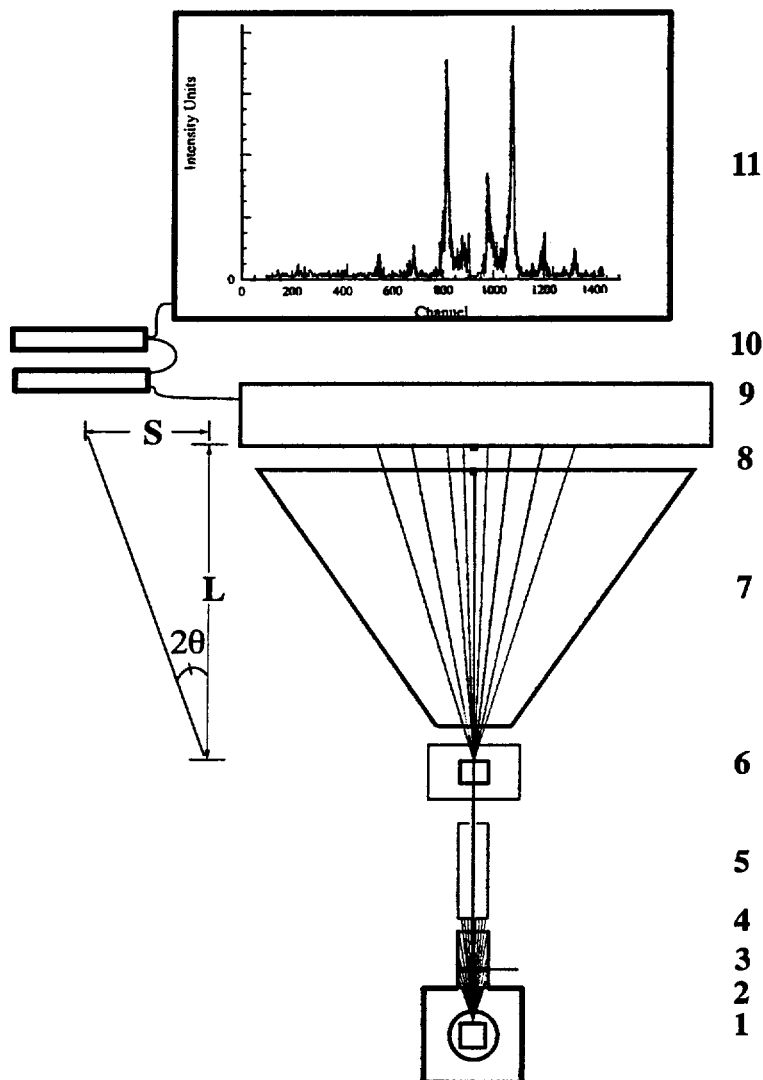


Figure 3.5 Top schematic view of the SAXS setup. (1) X-ray tower housing cathode tube and copper target. (2) Beryllium window. (3) Nickel filter. (4) Electronic shutter. (5) Pinhole collimator. (6) Temperature-regulated sample holder. (7) Evacuated chamber. (8) Lead beam stop. (9) Position-sensitive detector. (10) Multichannel analyzer and computer. (11) Final spectrum. From this experiment, L , S , and 2θ can be determined, and the Bragg equation may be applied to determine the d -spacing.

interpretation of diffraction patterns derived from lamellar and hexagonal phases are well understood [8].

The variation of egg phosphatidylcholine lipid interlamellar distance (d_{100}) as a function of water concentration has been studied [8]. At low concentrations of water, the phospholipid is in a gel state. Starting from pure lipid, initial incremental addition of small amounts of water results in no change in the d-spacing. This has been attributed to headgroup hydration which serves to swell the layer laterally. At a certain critical water concentration, the gel-to-lamellar phase transition occurs. Further addition of water simply results in unidirectional swelling; i.e., the incremental addition of water serves to increase the interlamellar distance. This is reflected by the linear increase of d as a function of water concentration. This linear region can be exploited to determine the average lipid layer thickness and cross-sectional area (see below). The increase in interlamellar distance occurs to a point where further addition of water results in no further swelling. At this point the system enters a two-phase region consisting of excess water and swollen lamellar phase. In this region it is possible to form vesicular structures. Thus lyotropic transitions can also be determined from the X-ray scattering data.

3.2.1 Experimental

The small-angle X-ray scattering studies were performed with a Phillips XRG-2500 generator operating at 35 kV and 20 mA using a sealed fine-focus copper tube. The X-ray was monochromatized, $\lambda = 1.54 \text{ \AA}$, using a β -nickel filter and a pinhole collimator. For a schematic of the experimental set-up, see Figure 3.6. The instrument was calibrated using lead stearate assigned at 50 \AA (Figure 3.7). The lipid:water mixtures were bath-sonicated for 1 day and equilibrated for 5 days before being included in a Mark capillary (1 mm o.d.) and placed in a temperature-regulated ($\pm 0.25^\circ\text{C}$) chamber. The diffraction patterns were collected using a linear position-sensitive detector with spatial resolution of $92 \mu\text{m}$ interfaced with a personal computer through a Nuclear Data multichannel analyzer. The sample-detector distance (30 cm) was adjusted to permit detection of small-angle diffraction peaks.

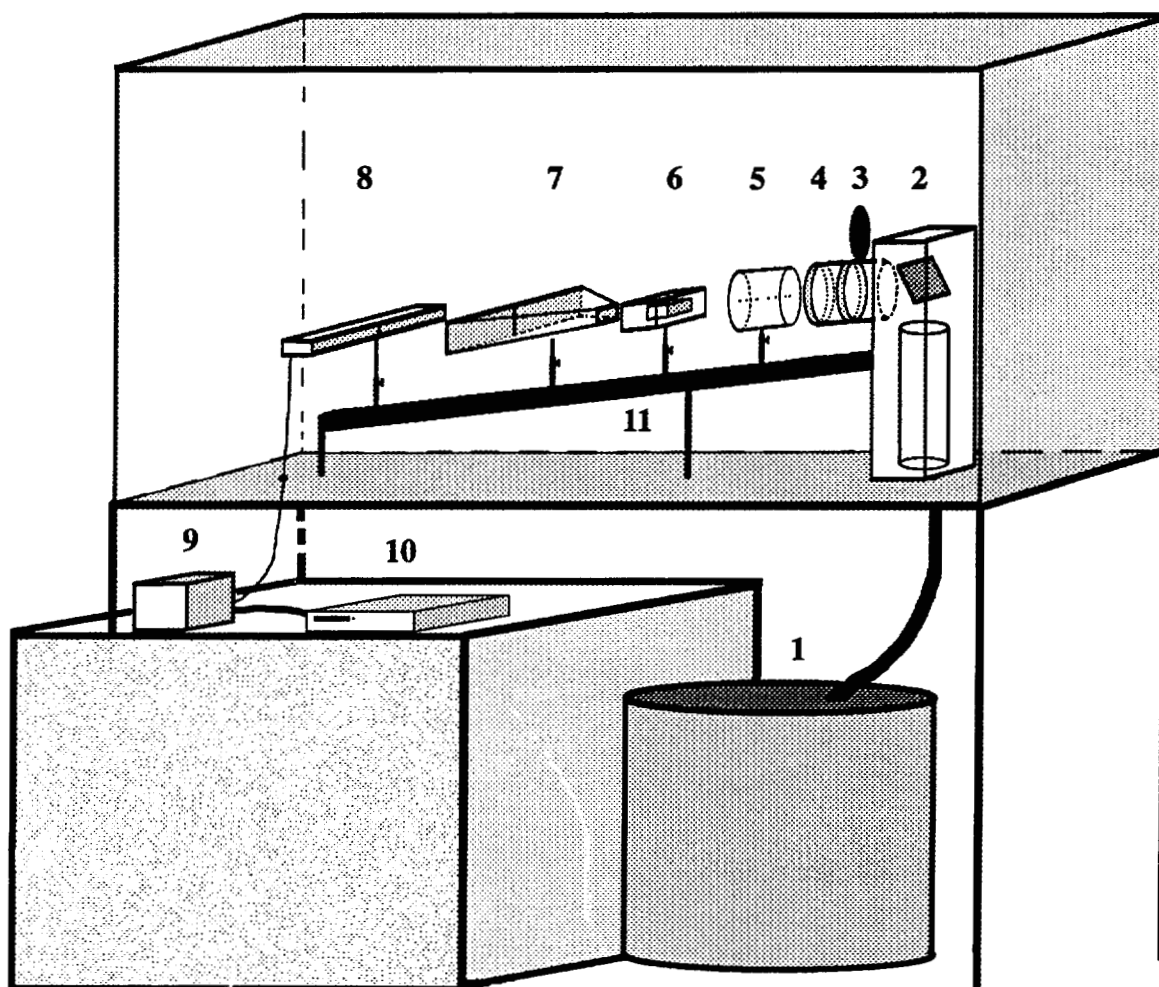


Figure 3.6 Experimental setup used in SAXS. (1) Generator. (2) X-ray tower. (3) Electronic shutter. (4) Nickel filter. (5) Pinhole collimator. (6) Sample holder. (7) Evacuated chamber. (8) Position-sensitive detector. (9) Multichannel analyzer. (10) Computer. (11) Optic rail.

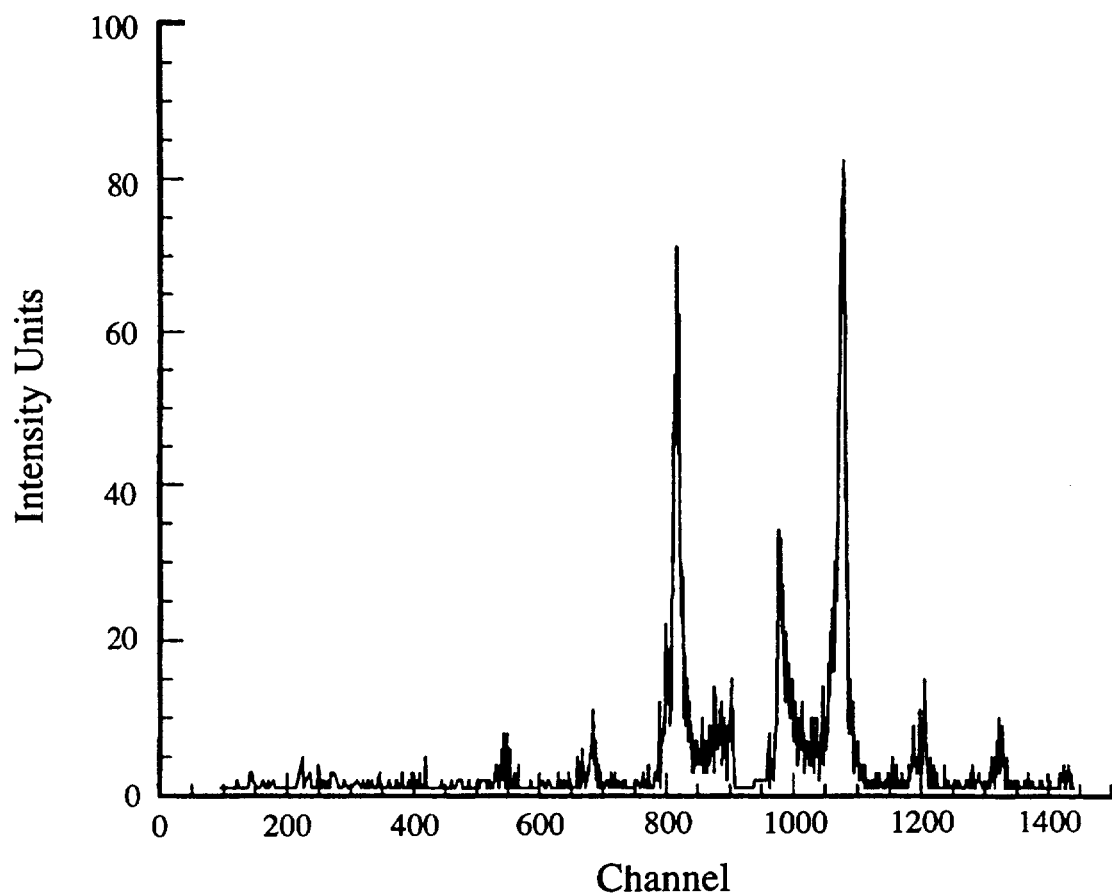


Figure 3.7 Small-angle X-ray scattering spectrum of lead stearate (calibration). The channel numbers are related to S . Assigning the lead stearate d -spacing of 50 \AA . L can be experimentally determined and applied for subsequent calculations.

Preparations of C20 bolaamphiphiles in quartz capillaries gave rise to X-ray reflections in the low-angle region (Figures 3.8 to 3.15). The measured d-spacings as a function of water concentration appear in Figure 3.16. From pure lipid up to 25% water, the d-spacing does not vary significantly. The scattering patterns in this composition region do not exhibit second- or higher-order peaks. This is indicative of the gel phase at room temperature.

At higher water concentrations, higher-order peaks appear (Figure 3.13). The long spacings in the low-angle region are in the ratio of 1:2 and are indicative of a one-dimensional lamellar structure. The water dependent, unidimensional repeat distance, d_{100} , determines the small-angle X-ray reflections in a series of stacked lamellae. This is clearly realized in Figures 3.13 and 3.14 in which the lamellar repeat distances increase with increasing water content until a limiting value is reached at about 25% lipid. After this value, the water is no longer contributing to interlamellar swelling such that further added water contributes to the excess free water phase. The effective bilayer thickness, d_l , can be calculated [8] from these water concentration-dependent d-spacing data from the relationship:

$$d_l = d_{100}/[1 + (v_w/v_l)(1 - c)/c] \quad (3.6)$$

where d_{100} is the unidimensional lamellar repeat distance and c is the weight fraction of the lipid at limiting hydration. The values v_l and v_w are the partial specific volumes for the lipid and the interlamellar water, respectively [9]. The extrapolated d-spacing is 32 Å for C20 bolaamphiphile lipids. This differs from the d-spacing of the pure lipid (40 Å) because: (1) pure lipid is in the gel phase at zero water concentration; since the hydrocarbon chains are crystalline in the gel phase, their contribution to the observed d-spacing is larger than in the liquid crystalline lamellar phase where the chains are molten, and (2) linear extrapolation assumes that all the water is involved in unidirectional swelling, which neglects the water involved in headgroup hydration.

The molecular area can also be obtained from the lipid thickness by the equation:

$$A_o = Mv_l/(N_A d_l) \quad (3.7)$$

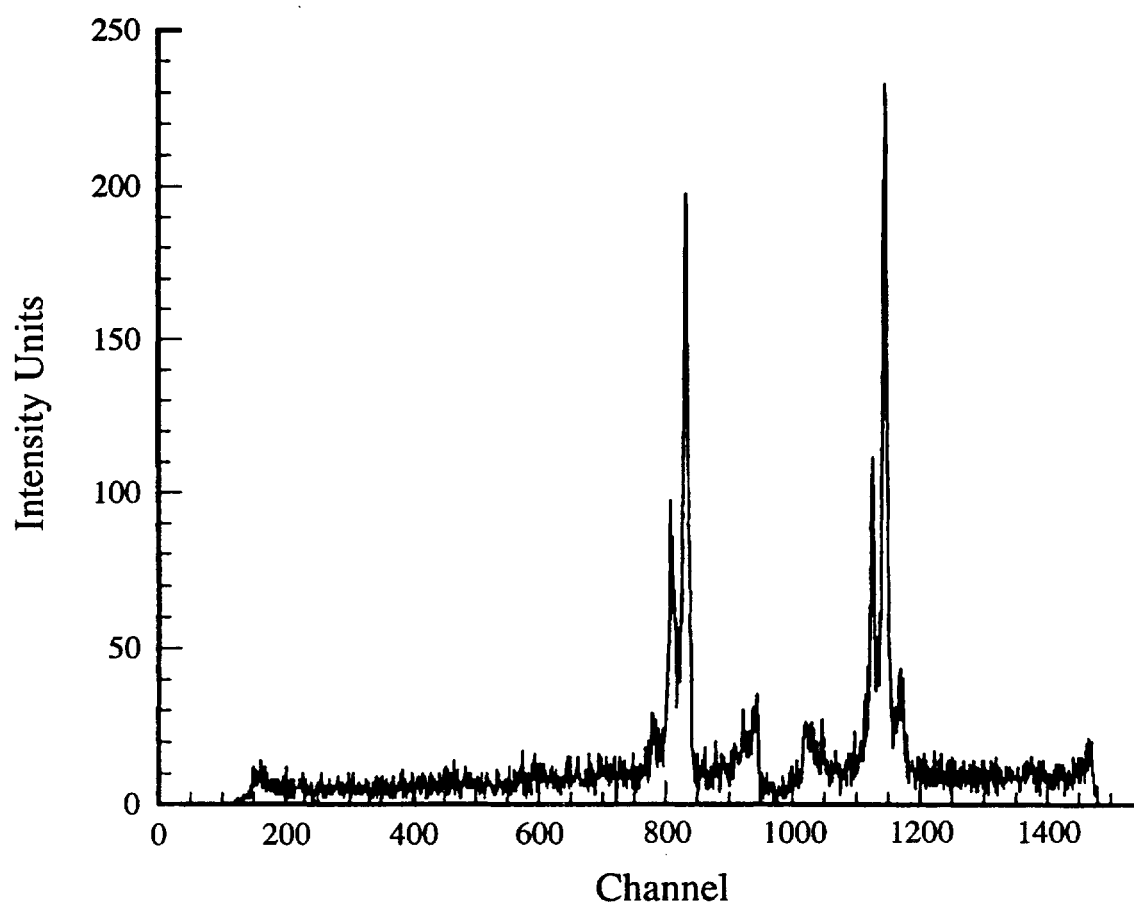


Figure 3.8 Small-angle X-ray scattering spectrum for pure C20 bolaamphiphile in the gel phase.

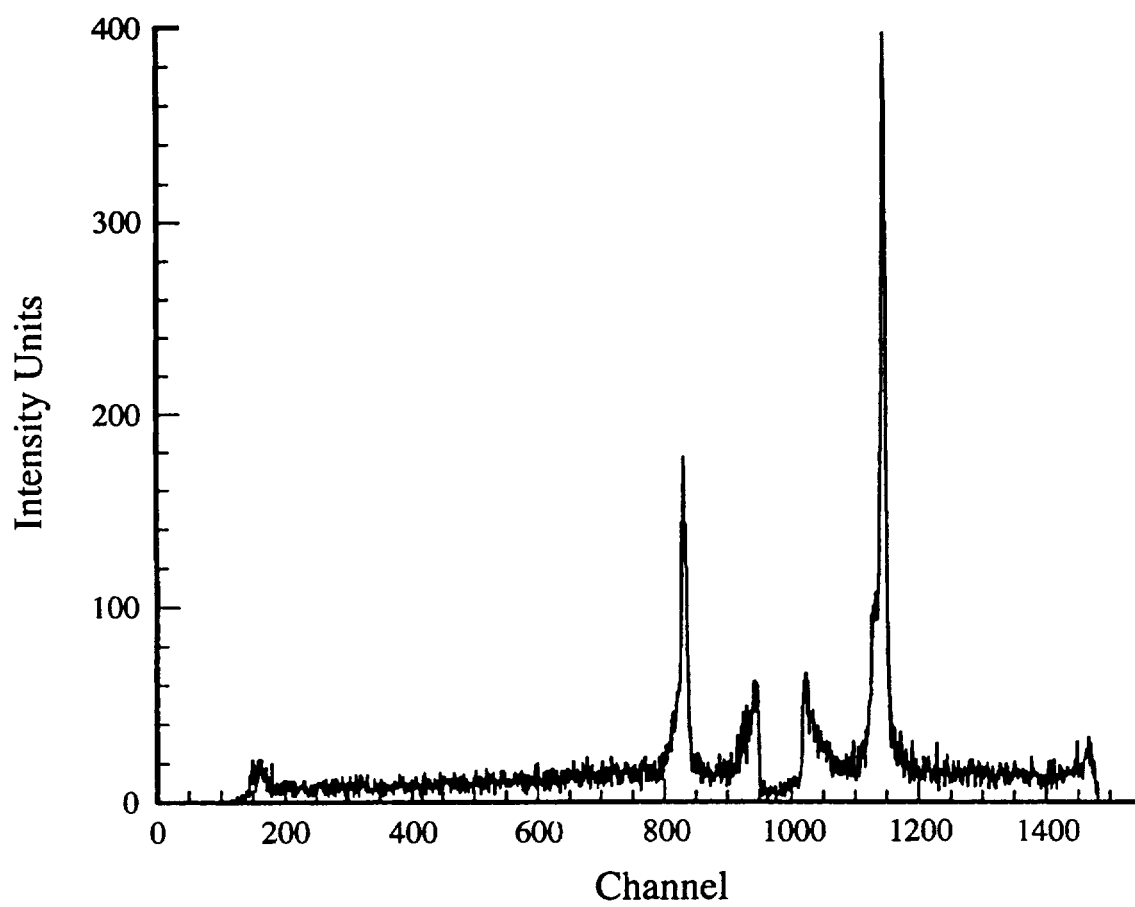


Figure 3.9 Small-angle X-ray scattering spectrum of 90% C20 bolaamphiphile in 10% H₂O.

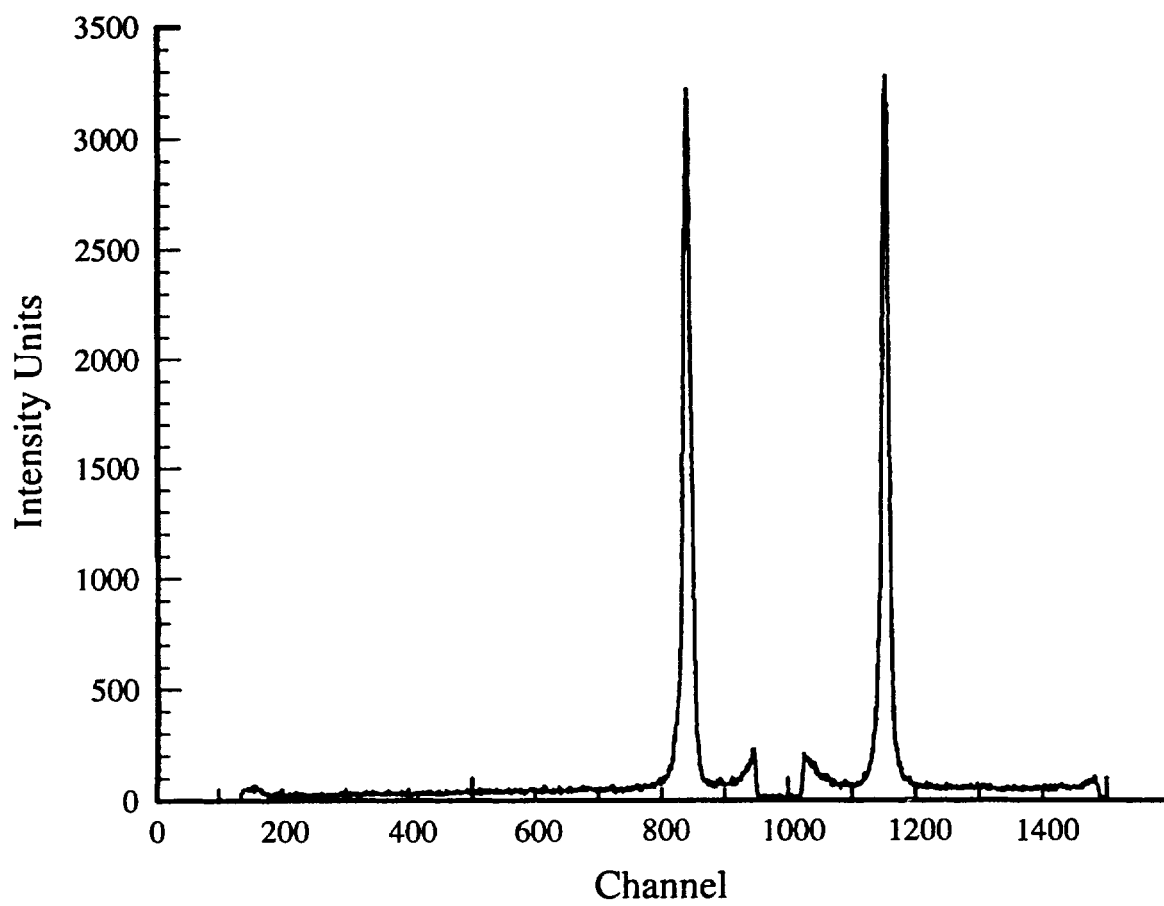


Figure 3.10 Small-angle X-ray scattering spectrum of 80% C20 bolaamphiphile in 20% H₂O in the gel phase.

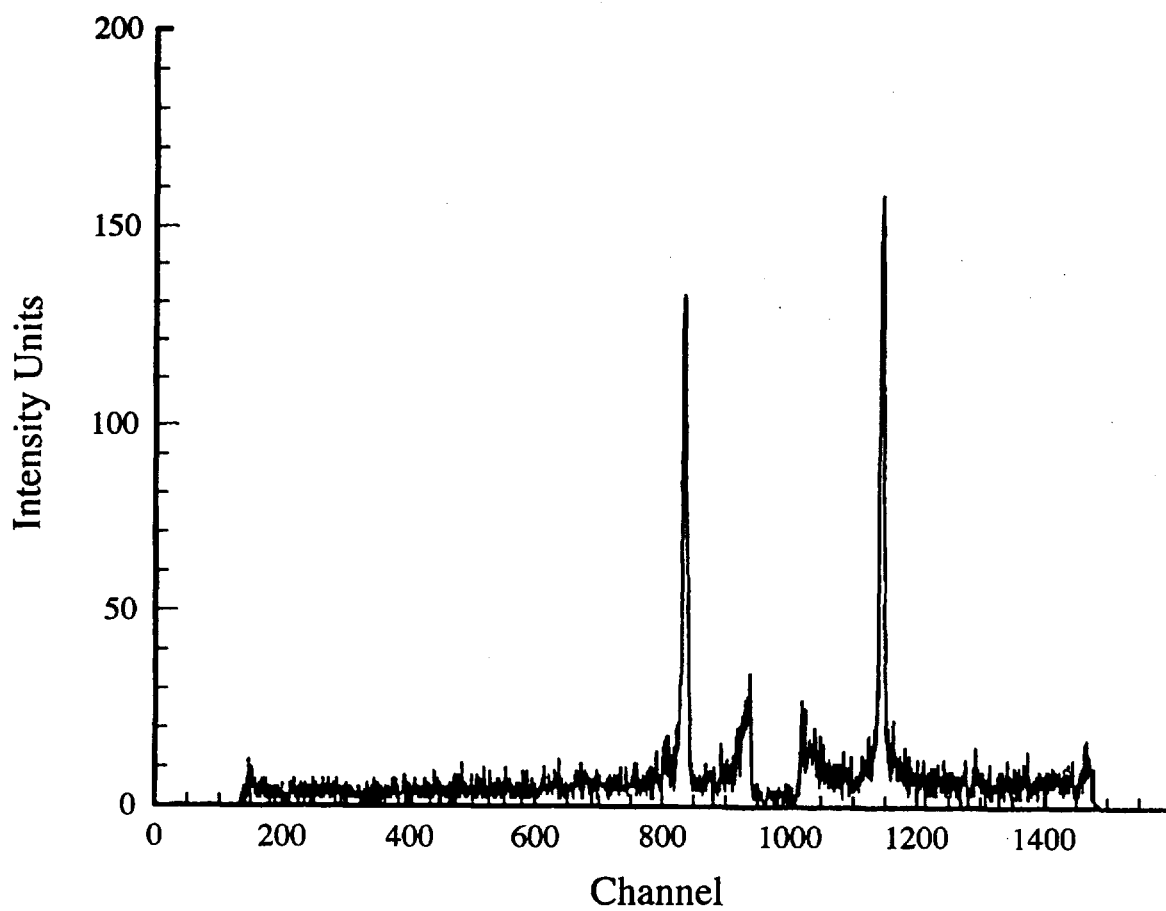


Figure 3.11 Small-angle X-ray scattering spectrum of 75% C20 bolaamphiphile in 25% H₂O in the gel phase.

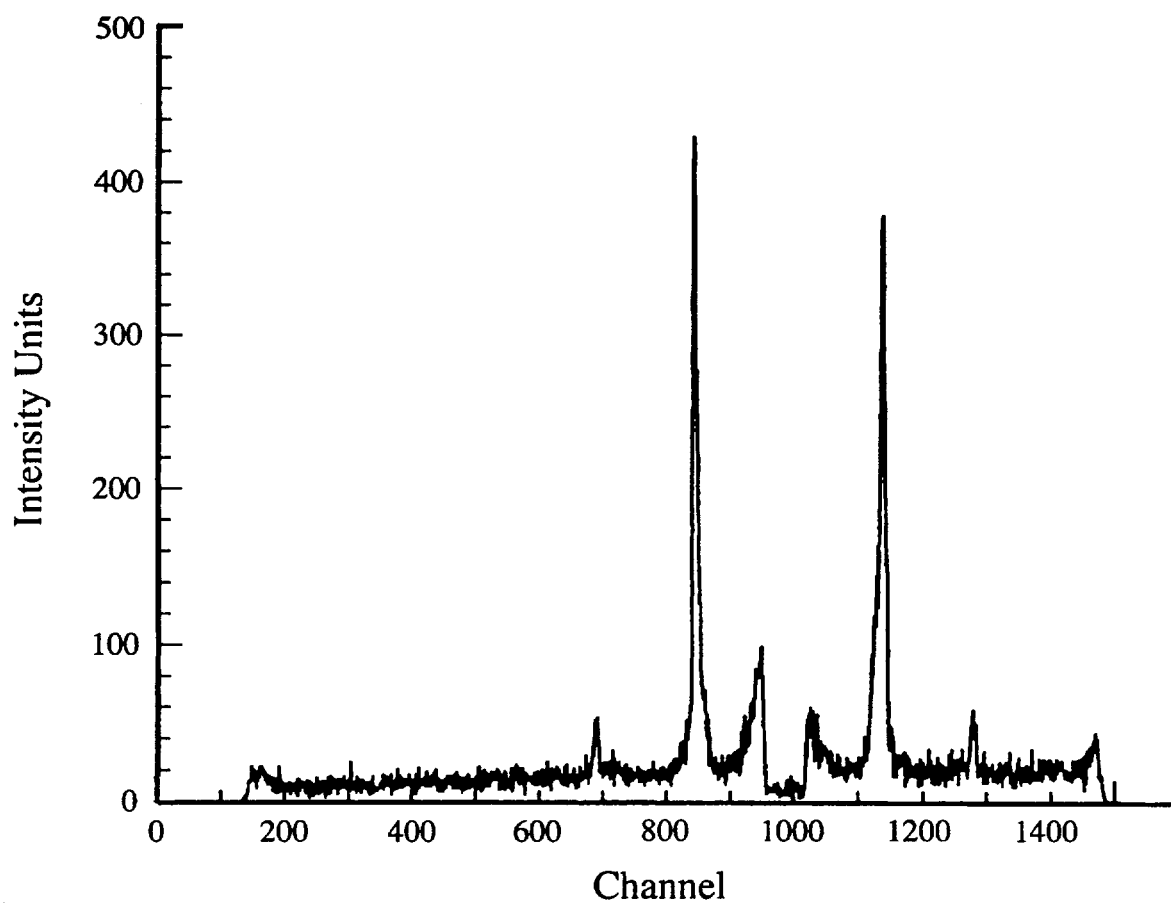


Figure 3.12 Small-angle X-ray scattering spectrum of 60% C20 bolaamphiphile in 40% H₂O in the lamellar phase.

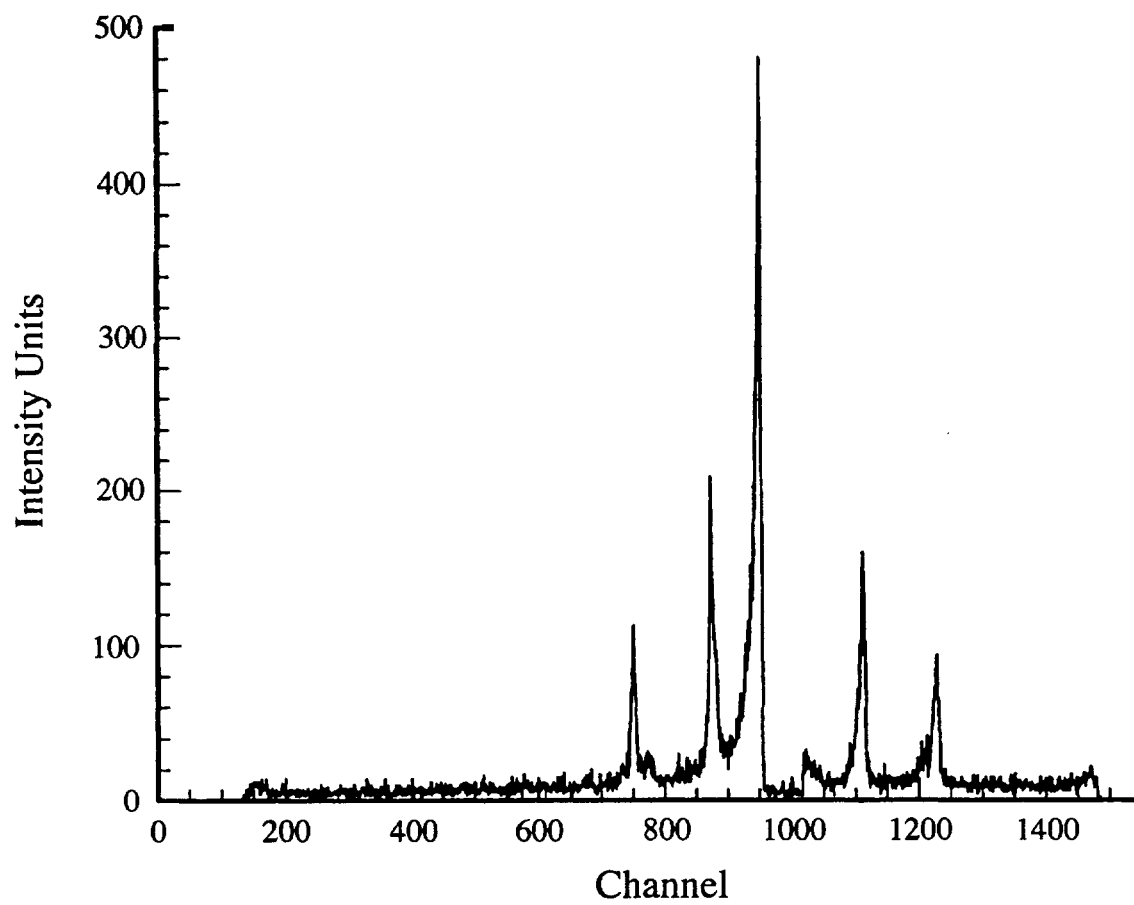


Figure 3.13 Small-angle X-ray scattering spectrum of 50% C20 bolaamphiphile in 50% H₂O in the lamellar phase.

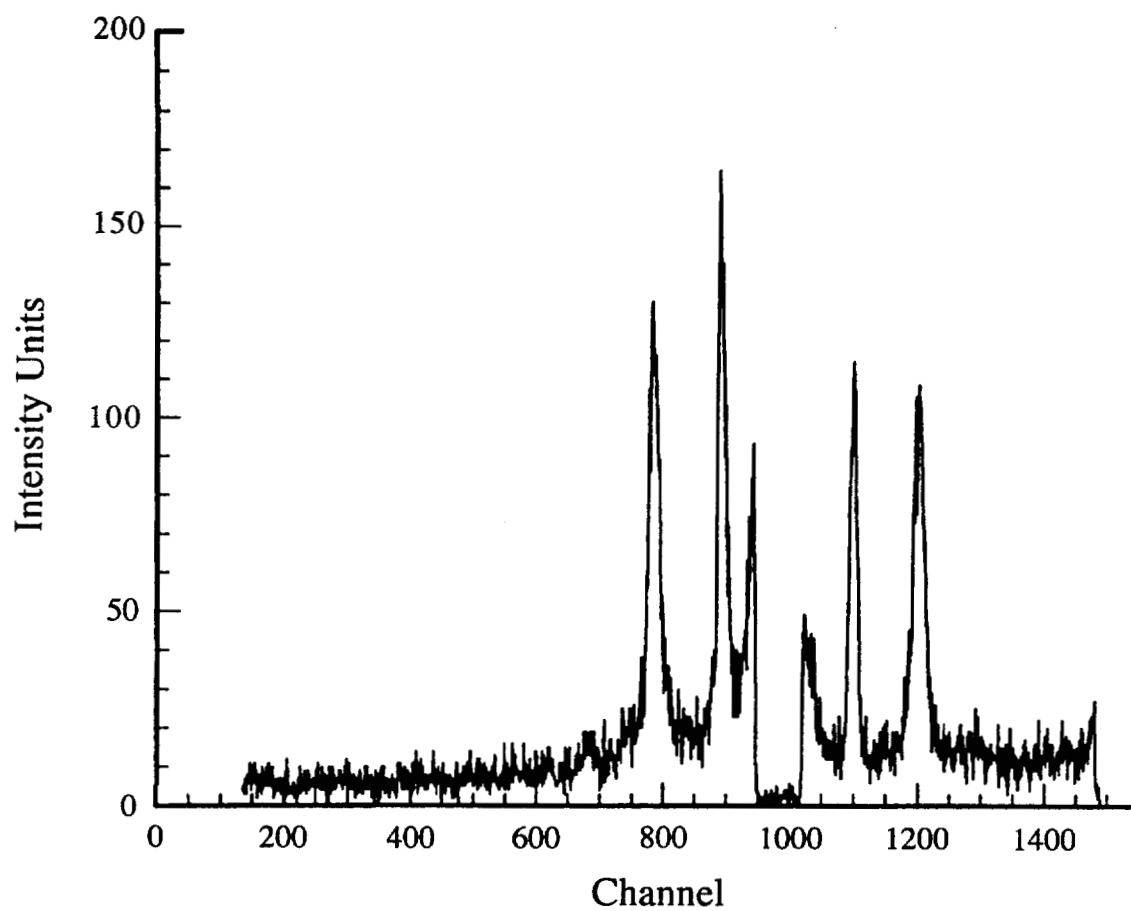


Figure 3.14 Small-angle X-ray scattering spectrum of 35% C20 bolaamphiphile in 65% H₂O with coexistence of the lamellar and vesicular phases.

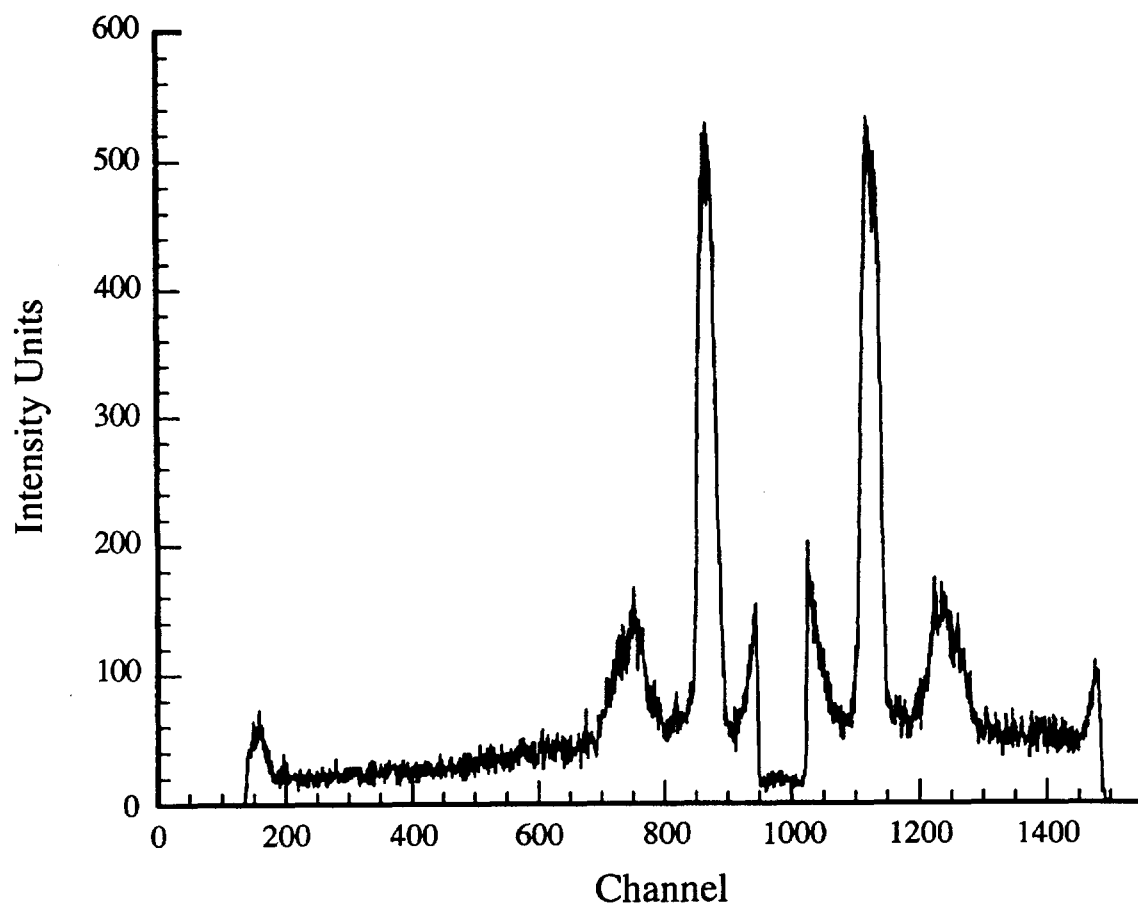


Figure 3.15 Small-angle X-ray scattering spectrum of 25% C20 bolaamphiphile in 75% H₂O with coexistence of the lamellar and vesicular phases.

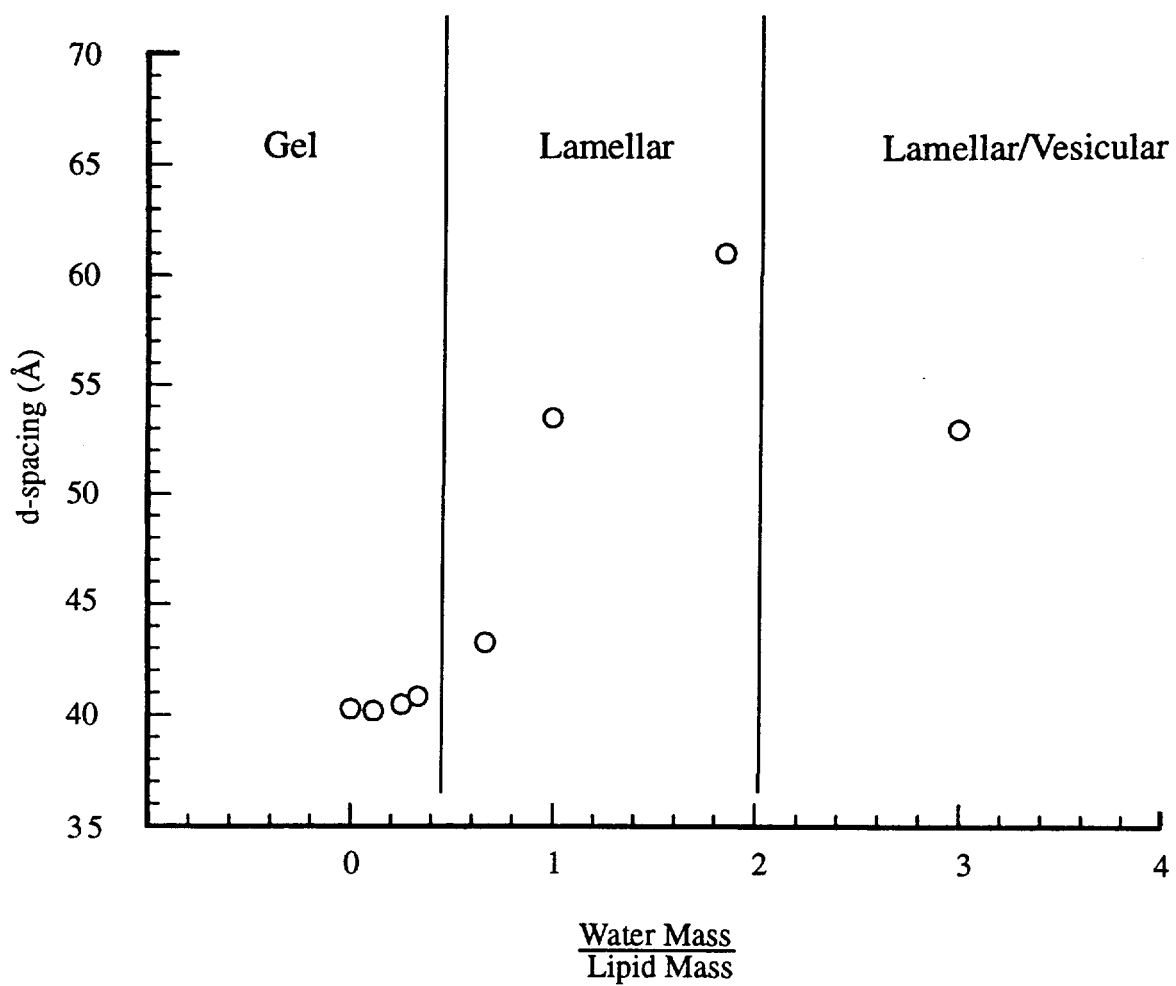


Figure 3.16 Plot indicating the dependence of d-spacings obtained from SAXS upon varying water levels with C20 bolaamphiphile.

where M is the lipid molecular weight, N_A is Avogadro's number, and d_l is one for monolayer lamella and two for bilayer structure [1]. The experimental and calculated X-ray parameters are given in Table 3.2.

An interesting comparison results from examination of the cross-sectional areas and lipid layer thickness of the gel and lamellar phases of dipalmitoyl phosphocholine and C20 bolaamphiphiles. The cross-sectional area for DPPC in the gel phase varies from 43 \AA^2 to 48 \AA^2 as the water content increases from 0 to 20%, while the cross sectional area of the bolaamphiphile lipid in the gel phase varies from 44 to 58 \AA^2 as the water content increases from 0 to 25% [8]. In the lamellar phase, the cross-sectional areas of DPPC vary from 68 to 81 \AA^2 as the water content is increased from 26% to 54% [8]. In the C20 bolaamphiphiles, the cross-sectional area in the lamellar phase is about 68 \AA^2 as the water content is increased from 40% to 50%. Under conditions of excess water, the cross-sectional areas are comparable in both materials at about 82 \AA^2 . Thus the structural modification of the C20 bolaamphiphile hardly affects its cross-sectional area in excess water.

The extrapolated lipid bilayer thickness for DPPC in the lamellar phase is 30-36 \AA [8], whereas in liquid crystalline phase C20 bolaamphiphiles the thickness varies from 26 to 27 \AA . We calculate the length per methylene group for DPPC of $1.03 \pm 0.1 \text{ \AA}$, whereas for C20 bolaamphiphiles it is calculated to be $1.3 \pm 0.1 \text{ \AA}$. This reflects a higher degree of order in the hydrocarbon region for the C20 bolaamphiphiles. This suggests that a membrane-spanning structure is more probable than the U-shaped configuration which places intramolecular headgroups on the same side of the layer. Furthermore, we observe a higher degree of ordering of the C20 bolaamphiphiles in the gel phase based upon similar calculations. The incremental change in length per methylene group is 1.75 \AA for C20 bolaamphiphiles versus 1.59 \AA for the DPPC.

From these X-ray studies, the binary phase diagram of C20 bolaamphiphiles and water indicates that the gel phase exists up to 25% water, with the appearance of the gel-lamellar liquid crystal phase transition between 25-40% of water. The lamellar phase persists up to 65% water, where the lamellar and vesicular phases coexist. At 75% water, we see a scattering pattern reminiscent of vesicular phases

Table 3.2. Summary of Small Angle X-ray Scattering Data for C16 and C20 Bolaamphiphiles at Different Extents of Hydration

Lipid Type	% Lipid	Phase	Figure Number	d-spacing (Å)	(1-c)/c	d ₁ (Å)	A ₀ (Å ²)
C20 bolaamphiphile	100	gel	3.8	40.3 ± 0.5	0	40.3	44
	90	gel	3.9	40.2 ± 0.5	0.111	36.2	49
	80	gel	3.10	40.5 ± 0.5	0.25	32.4	55
	75	gel	3.11	40.8 ± 0.5	0.33	30.6	58
C16 bolaamphiphile	60	lamellar	3.12	43.2 ± 0.5	0.67	26.0	69
	52	lamellar	3.13	53.5 ± 0.5	1.0	26.7	67
	35	lamellar/vesicles	3.14	61.0 ± 0.5	1.86	21.32	83
	25	vesicular	3.15	59.4 ± 0.5	3.0	14.8	120
C16 bolaamphiphile	100	gel	3.17	33.25 ± 0.5	0	33.25	48
	90	lamellar	3.18	34.26 ± 0.5	0.11	30.8	42
	80	lamellar	3.19	35 ± 0.5	0.25	28	57
	70	vesicular	3.20	39.4 ± 0.5	0.43	27.5	58

found in ordinary phosphocholines. Our approximate phase diagram is denoted in Figure 3.16 (from the d-spacing plot).

The SAXS data for C16 bolaamphiphile are presented in Figures 3.17 to 3.20. The measured d-spacings as a function of water concentration for C16 bolaamphiphiles appear in Figure 3.21. Unlike C20 bolaamphiphile lipids, the gel phase of C16 bolaamphiphiles disappears below 10% water concentration; however, the cross-sectional area at equivalent water concentration is comparable (44 Å versus 48 Å) for C16. When the d-spacing is 33 Å, the lamellar phase appears between 0-10% water and disappears at between 20-30% water. The cross-sectional area in the lamellar phase is significantly lower (between 52 Å² and 57 Å²) in the C16 bolaamphiphiles, which may require a lesser degree of headgroup hydration to induce this phase. The degree of chain ordering as revealed by incremental length per methylene group is even higher than in the C20 bolaamphiphiles. Furthermore, the increased hydration in the vesicular phase does not lead to significantly higher cross-sectional areas, suggesting that larger vesicles may be present.

In summary, the X-ray data of these two bolaamphiphiles display only three distinct thermodynamic phases: gel, lamellar and vesicular. X-ray and DSC data are consistent with a monolayer structure for the bolaamphiphile membrane in bulk phases. Unlike bulk phases, the air-water interface provides a highly unsymmetrical surface. Monolayer experiments were performed to see how the air-water interface might influence bolaamphiphile organization. These experiments are described in the following section.

3.3 Monolayer Experiments

3.3.1 Introduction

Since C16 and C20 bolaamphiphiles each have two phosphocholine headgroups, the phase behavior at the air-water interface was expected to be qualitatively different when compared to amphiphiles possessing a single phosphocholine headgroup. The monolayer film balance technique provides surface pressure vs. area isotherms that may offer insights into structure-property

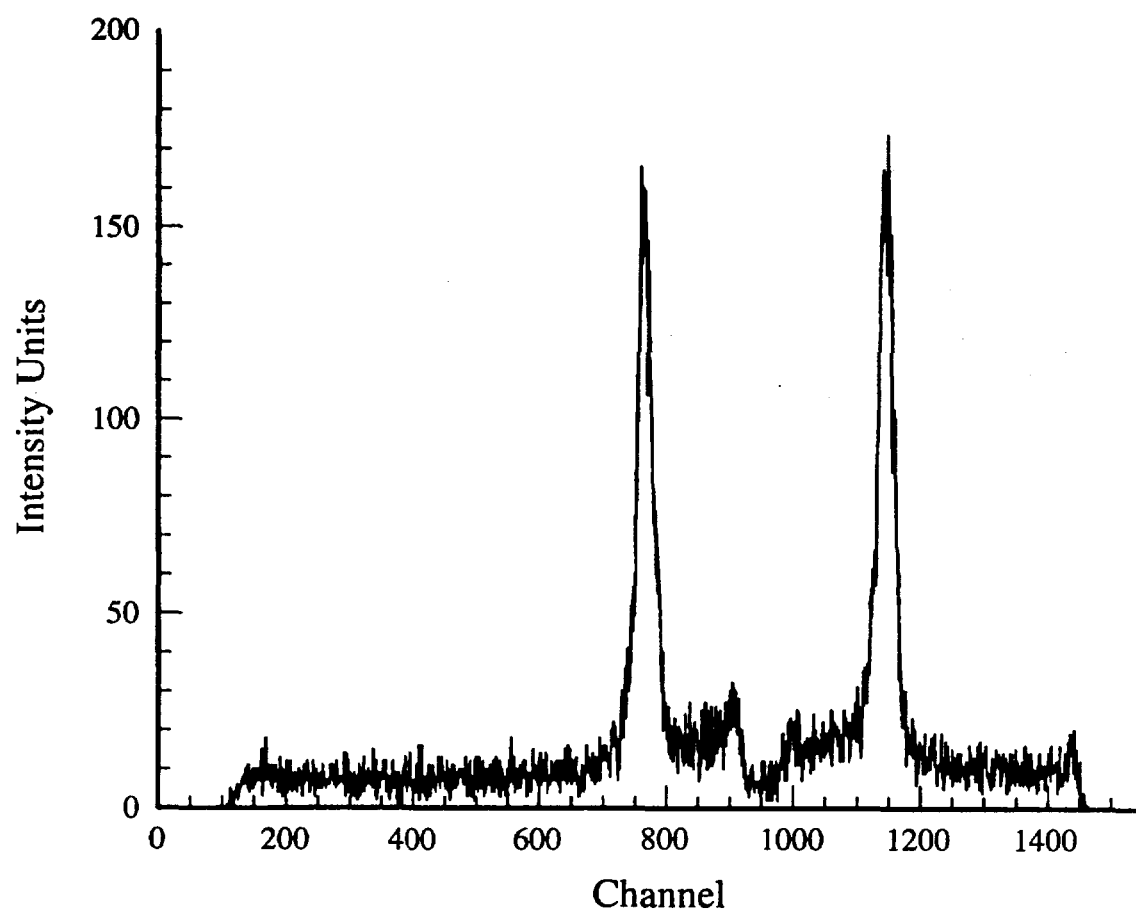


Figure 3.17 Small-angle X-ray scattering spectrum of pure C16 bolaamphiphile.

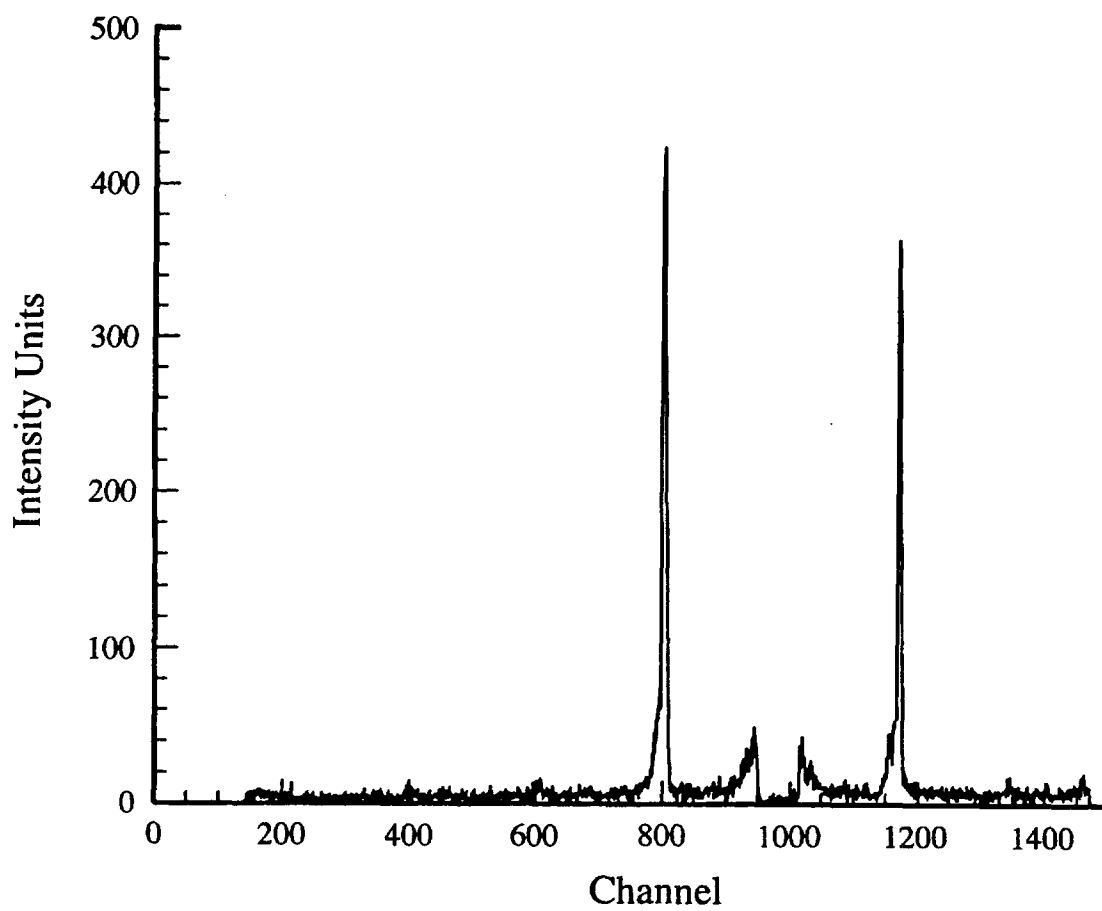


Figure 3.18 Small-angle X-ray scattering spectrum of 90% C16 bolaamphiphile in 10% H₂O. The pattern is indicative of the lamellar phase.

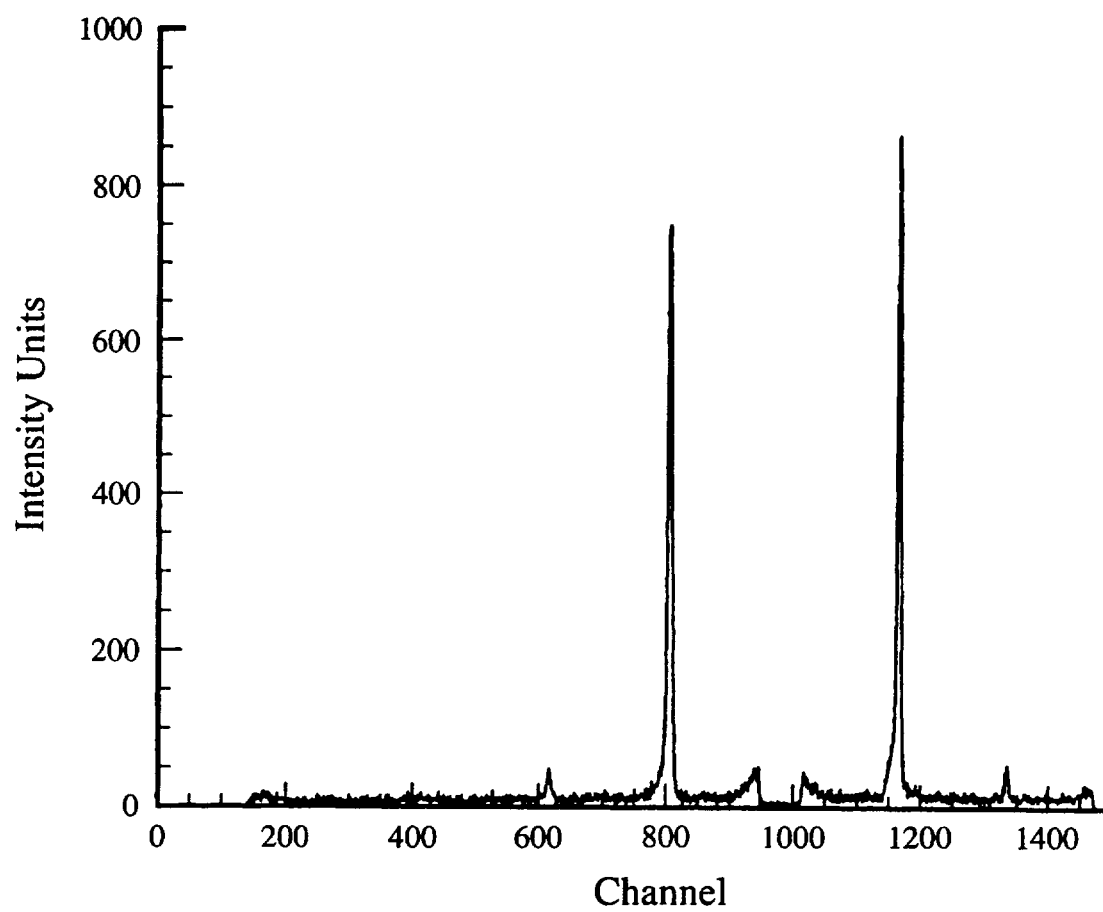


Figure 3.19 Small-angle X-ray scattering spectrum of 80% C16 bolaamphiphile in 20% water in the lamellar phase.

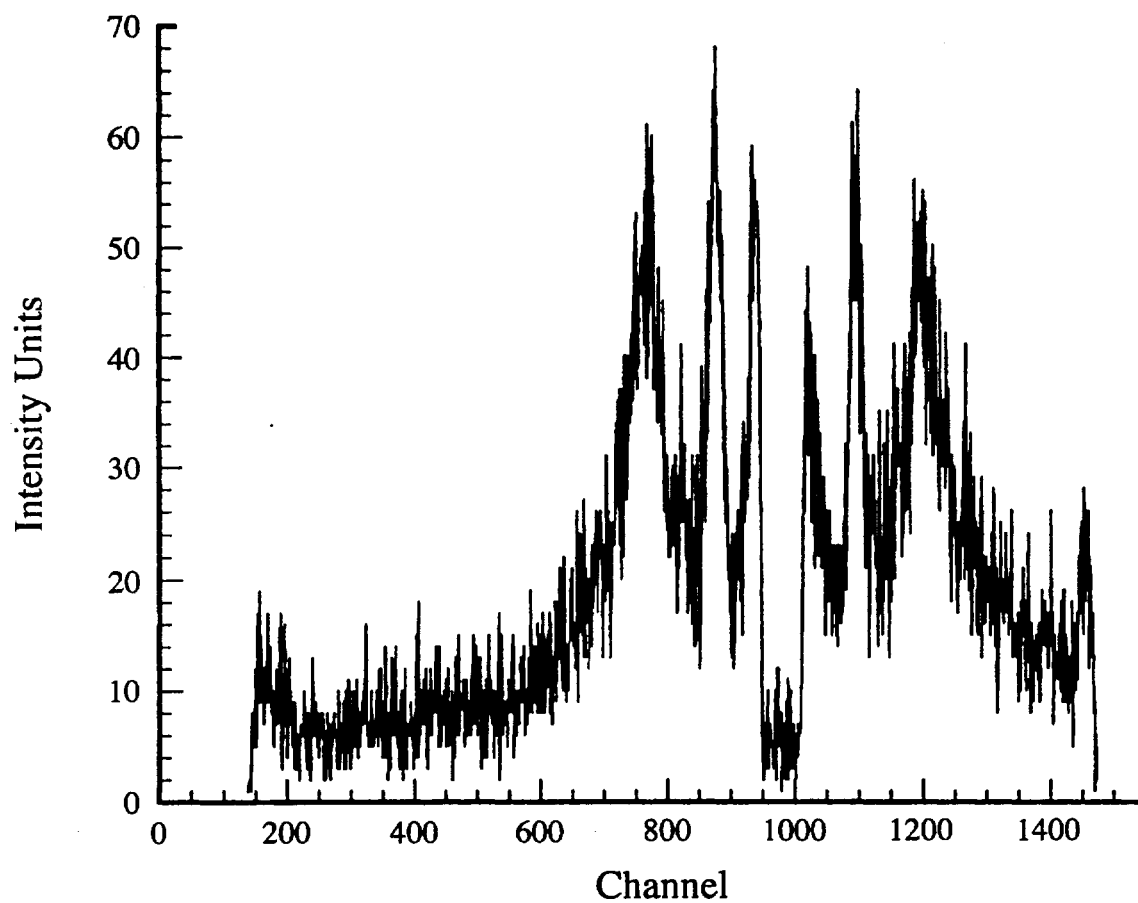


Figure 3.20 Small-angle X-ray scattering spectrum of 70% C16 bolaamphiphile in 30% H₂O. The vesicle phase is observed.

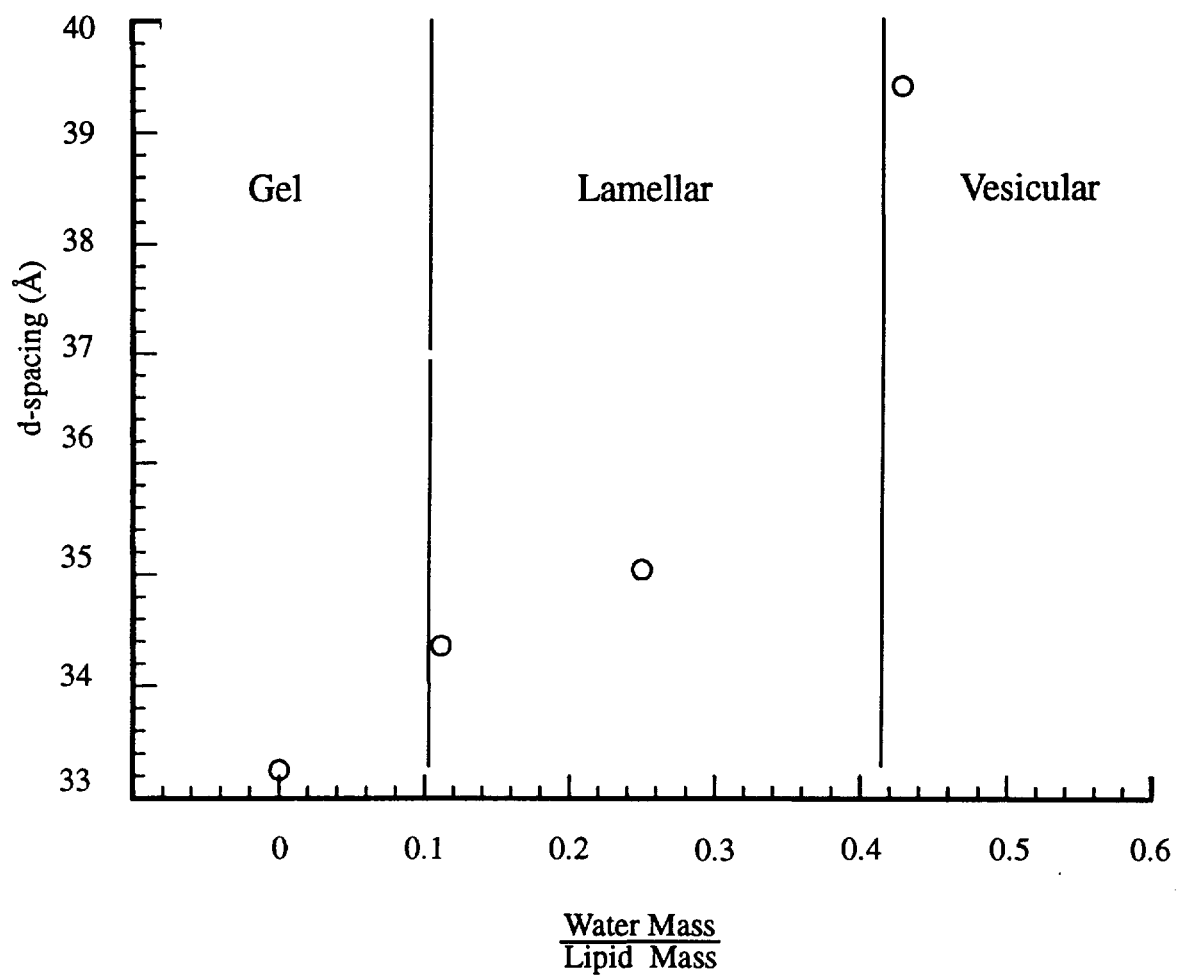


Figure 3.21 Observed dependence of d-spacing upon varying water levels with C16 bolaamphiphile (approximate phase diagram).

relationships. The advantages of such experiments are: (1) the lateral surface pressure can be easily controlled, (2) molecular areas are easily determined, especially at high lateral surface pressures where they should approach the limiting areas governed by the lateral packing constraints (thus they should correlate to the data obtained in the SAXS experiments), and (3) temperatures and subphase conditions are readily controlled.

Monolayer studies have a long history. In the late nineteenth century, Lord Rayleigh and Fraulein Pockels showed that monomolecular layers of amphiphilic molecules could be formed at the air-water interface. The classic method for the study of monolayers at the air-water interface utilizes a Langmuir trough. Typically, modern troughs are constructed of a hydrophobic material such as Teflon, which is filled with an aqueous subphase until a meniscus forms over the trough. Two parallel barriers, one movable and one immobile, serve to isolate the monolayer once it is spread upon the surface between the barriers. The amphiphiles are spread from a volatile organic solvent which is permitted to evaporate prior to the study. A surface pressure (π) results from the difference in surface tension of the pure subphase (γ_{subphase}) and the surface tension of the film (γ_{film}) equated as:

$$\pi = \gamma_{\text{subphase}} - \gamma_{\text{film}} \quad (3.8)$$

Pure water at 20° C has a surface tension (γ_{subphase}) of 72.9 mN m⁻¹. When very dilute films ($> 500 \text{ \AA}^2 \text{ molecule}^{-1}$) are spread on pure water, surface tension (γ_{film}) remains very close to 72.9 mN m⁻¹, giving a surface pressure of essentially zero. As the film is compressed by the moveable barrier, the density of the film increases; meanwhile, γ_{film} decreases and π increases. The surface pressure for monolayers at the air-water interface can range from 0 mN m⁻¹ to $\sim 72.9 \text{ mN m}^{-1}$. Surface pressure measurements can be achieved (directly or indirectly) by several methods. The Wilhelmy plate method takes advantage of the vertical force changes which occur on a paper or hydrophilic metal plate as the surface pressure changes [10]. The Wilhelmy plate is coupled to a force transducer, and suspended between the mobile and static barriers into the interface. The vertical force on the Wilhelmy plate is defined as:

$$F = \rho_p g l w t + 2\pi\gamma (t + w) \cos \theta - \rho_l g t w h \quad (3.9)$$

where F is the force on the Wilhelmy plate (mN), g is the gravitational acceleration, l , w , and t are the plate's length, width and thickness respectively, h is the depth to which the plate is immersed, θ is the contact angle between water and the plate, γ is the surface pressure, and ρ_p and ρ_l are the densities of the plate and liquid, respectively. Ordinarily, the Wilhelmy plate is completely wetted by the liquid subphase ($\theta \approx 0$) and t is very small compared to w . If the change in force is measured while keeping constant the plate immersion depth, the relation simplifies to:

$$\Delta F = -2\pi w \quad (3.10)$$

In this way, π is easily determined by measuring the vertical (in mN), with respect to area per molecule A (in $\text{\AA}^2 \text{ molecule}^{-1}$) at constant temperature; this yields the surface pressure-area isotherm. Two important parameters arising from intermolecular interactions which can be revealed in the π - A isotherm are (1) the limiting area per molecule (A_0) which is obtained by extrapolating, tangentially, from the steep part of the isotherm to zero surface pressure; and (2) the maximum surface pressure, P_c (and the corresponding molecular area at high pressure), where the monolayer collapses.

The π - A isotherm for hexadecanoic acid shown in Figure 3.22 illustrates the possible phases of a monolayer at the air-water interface. These phases are gaseous, liquid expanded, condensed, and solid. The gaseous state is characterized by large intermolecular separation and low surface pressures ($< 1 \text{ mN m}^{-1}$). The surface pressure gradually rises as the molecules are forced into areas which are comparable to their molecular dimensions. At this state, a transition to the liquid expanded state occurs. At this transition, the surface pressure remains constant while the surface area decreases significantly. In this region, gaseous and expanded states coexist, analogous to the three-dimensional liquid-gas transition. The magnitude of the area discontinuity decreases as the temperature is increased and disappears completely above a critical temperature. Further decreases in the surface area from the liquid expanded state result in a gradual increase in the surface pressure. This reflects the interplay of attractive (i.e., van der Waals force) and repulsive (i.e., electrostatic) intermolecular interactions. At a certain critical area, the attractive van der Waals interactions dominate and a phase transition to a liquid condensed state occurs. This condensed state is similar to the liquid crystalline phase. Upon further reduction in

surface area, the molten hydrocarbon chains condense into a crystalline state similar to the gel phase. This phase is considered to be a two-dimensional solid state. Further reduction of area in the solid phase is limited since the compressibility in this state is lower than for the gas-to-liquid expanded transition. This difference in compressibility is exemplified by the differences in the slopes of the lines tangent to the ascending portion of the isotherms with respect to the two-phase transitions. Furthermore, the molecular areas in which the transitions occur differ, in that transitions from the gas-to-liquid expanded state occur at higher molecular areas compared to transitions from the liquid expanded-to-condensed state. Further area decreases (i.e., through the solid state), result in the collapse of the layer through many possible mechanisms; e.g., subphase migration, buckling and cracking. However, the precise mechanism of collapse cannot be derived from the π -A isotherm.

For a number of reasons, not all amphiphiles undergo the liquid condensed to solid-state phase transitions. If the repulsive forces between molecules are more significant than their attractive forces, material may be forced out from the film (e.g., into the subphase) while approaching the condensed state. This is simply a partitioning issue, based upon whether the amphiphiles prefer to be in a solid state or a water-solubilized state. When the material is forced away by collapse it does not contribute to the surface area; therefore, pressure changes upon further compression of the monolayer are not observed.

In order to understand the monolayer phase behavior, it is instructive to compare the π -A isotherms of several dialkyl phosphatidylcholines (PCs) to understand the influence of hydrocarbon chain length on the types of transitions observed near 20°C. Although temperature and subphase conditions under which the isotherms were collected may differ slightly, a qualitative interpretation is still possible [11] (see Figure 3.22). As discussed in the hexadecanoic acid example, there is a distinction between the slopes of the lines tangent to the ascending region of the isotherms, especially near the onset of the transition, as well as the molecular area range in which the transitions occur. In this comparison, dicapryloyl PC (C_{10}), dilauroyl PC (C_{16}), and dimyristoyl PC (C_{14}) have gradually ascending slopes and

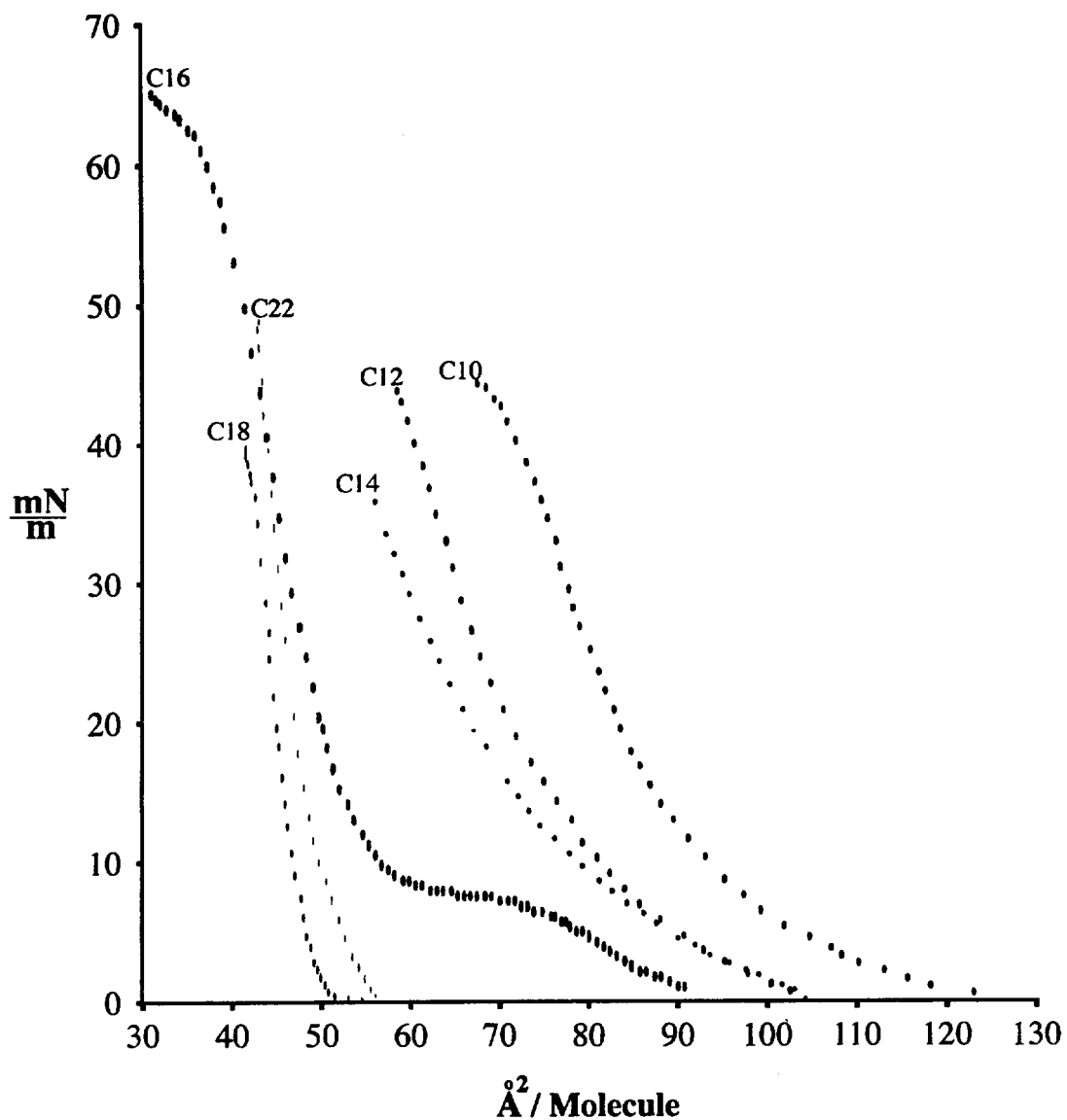


Figure 3.22 A comparison of isotherms, acquired at the air-water interface, of several dialkyl phosphatidylcholines (PCs). C10, dicapryoyl PC; C12, dilauroyl; C14, dimyristoyl PC; C16, dilauroyl PC; C18, distearoyl PC; C22, dibehenoyl. [From Ref. 2]

relatively higher molecular areas at the onset of the transition. In this analysis, the shorter-chain PCs display the liquid expanded state and do not undergo phase transitions to the liquid condensed state prior to collapse. In contrast, distearoyl PC (C_{18}) and dibehenoyl PC (C_{22}) phospholipids indicate sharper ascending slopes and somewhat lower molecular areas at the onset of the phase transition. These longer-chain PCs exhibit the liquid condensed state. DPPC (C_{16}), having an intermediate chain length, displays both types of phase transitions.

The possible interpretation of the alkyl chain length-dependent differences in π -A isotherms, for the series of phospholipids (i.e., why shorter-chain phospholipids, C_{10-14} PC, display liquid expanded states while the longer-chain phospholipids, C_{18-22} PC, exhibit the liquid condensed state) is correlated to their chain-melting transitions. Recall that C_{10-14} PC lipids exhibit chain-melting transitions below room temperature, while C_{18-22} PC lipids undergo such transitions well above room temperature. In the C_{16} PC case (i.e., DPPC), the chain-melting transition occurs near room temperature, such that a combination of both phase types is observed (i.e., expanded and condensed states separated by a phase transition). The acquisition of π -A isotherms for C16 and C20 bolaamphiphiles and their comparison to the previously discussed data follows.

3.3.2 Experimental setup

The monolayer film balance used was a KSV 3000 trough (KSV Instruments, Helsinki, Finland) milled from a solid block of Teflon[®] to provide a 712.44-cm² surface area over a 1.1-liter total subphase volume. The density of the monolayer film was controlled by a mobile hydrophilic barrier which swept the interface by means of a microstepped DC motor. The surface pressure (π) was measured with a sand-blasted platinum Wilhelmy plate which was dipped in 100% ethanol and flamed to red hot with a bunsen burner, then suspended from an electronic microbalance. The Wilhelmy plate was maintained in the null position by an electronic negative feedback loop. Surface pressure was determined digitally from the restoring force on the plate using a computer-stored calibration constant.

3.3.3 General experimental considerations

In the series of experiments, chloroform solutions of pure bolaamphiphile lipids (40.0 μL) were spread using a microsyringe (Kloehn Microsyringe Inc.). The concentration of the C20 bolaamphiphile was 1.02 mg/mL, while the concentration of C16 bolaamphiphile was 0.68 mg/mL. The amount spread onto the surface corresponded to the two-dimensional gas state. The subphase was 18 M Ω (MilliporeTM) water at 20°C. The compression rate in these experiments was -6.0 cm²/min.

3.3.4 Monolayer data

To more easily interpret the π vs. molecular area isotherms of C16 and C20 bolaamphiphiles, the data were normalized and compared with the isotherms from a series of dialkyl PCs (Figure 3.23). In this composite plot, the bolaamphiphiles demonstrate much larger molecular areas compared to the dialkyl PCs. In the C16 bolaamphiphile case, the molecular area was 172 Å² while for C20 bolaamphiphile the measured molecular area was 105 Å². The magnitude of these areas is reasonable since each bolaamphiphile molecule has two headgroups. With two headgroups the amphiphiles would most likely assume a geometry with the two headgroups facing the water phase while the alkyl chains extend into the air phase. In another comparison, the bolaamphiphile data were included in an isotherm series of surface pressure versus area per headgroup (Figure 3.24). In this comparison, the area for the C20 bolaamphiphile corresponded to the longer-chained dialkyl PCs while the C16 bolaamphiphile had an area which corresponded to the shorter-chained dialkyl PCs. The interpretation for this behavior is that in the C20 bolaamphiphiles, the alkyl chains are more crystalline than in the C16 bolaamphiphiles which have fewer hydrophobic interactions. The resulting areas would require that the C20 bolaamphiphile compresses with the long connecting alkyl chain forming a hairpin turn in the air phase, permitting the alkyl chains to pack closely.

Another difference in the monolayer characteristics of the C16 bolaamphiphiles and C20 bolaamphiphiles is the molecular area at the onset of the gas-liquid expanded transition. The fact that C16 bolaamphiphiles exhibit a larger area implies that there

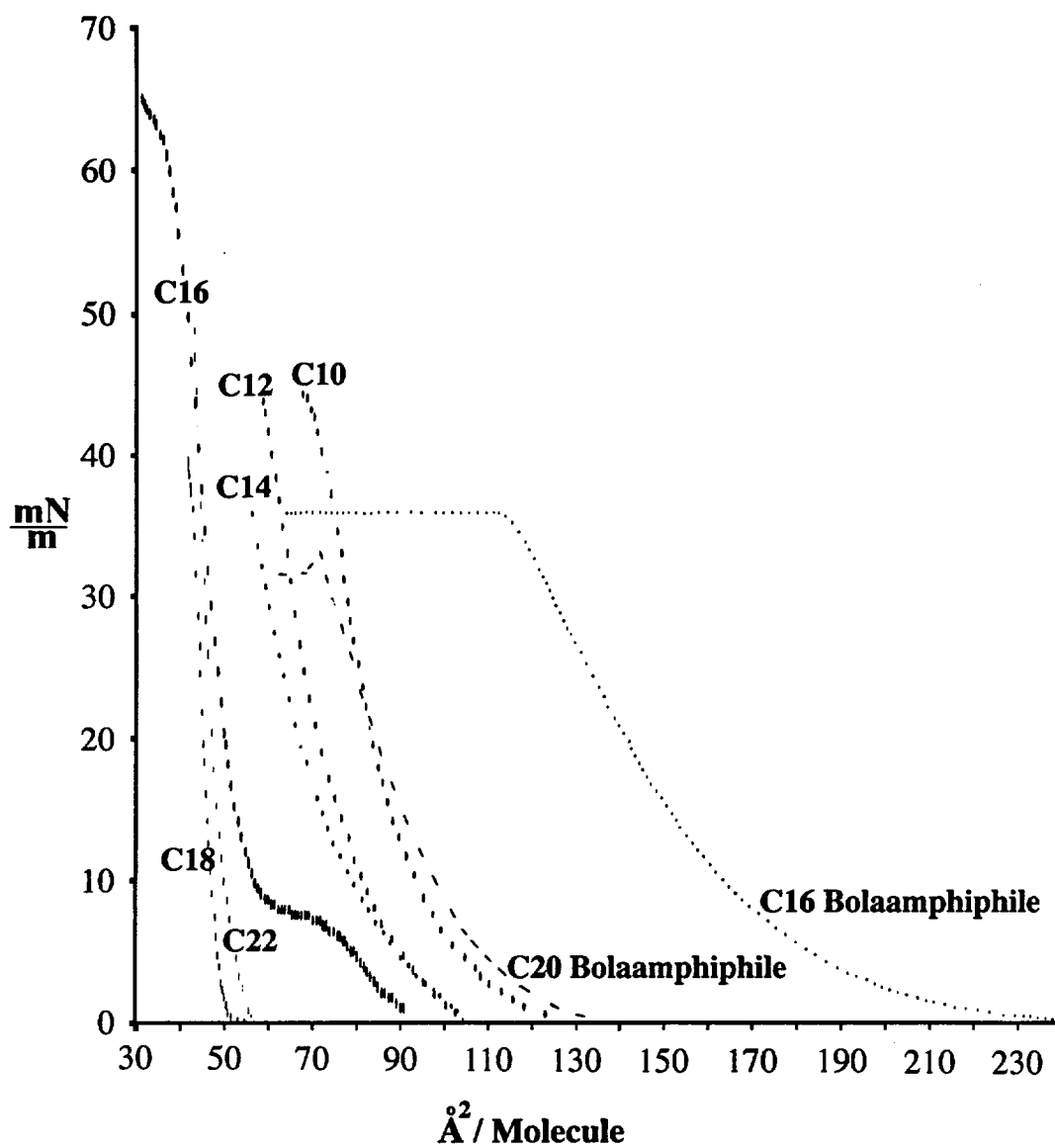


Figure 3.23 A comparison of pressure versus area isotherms, acquired at the air-water interface, of several dialkyl phosphatidylcholines (PCs). C10, dicapryoyl PC; C12, dilauroyl; C14, dimyristoyl PC; C16, dilauroyl PC; C18, distearoyl PC; C22, dibehenoyl [from Ref. 2]. Also included are the isotherms from the bolaamphiphile experiments indicating larger molecular areas.

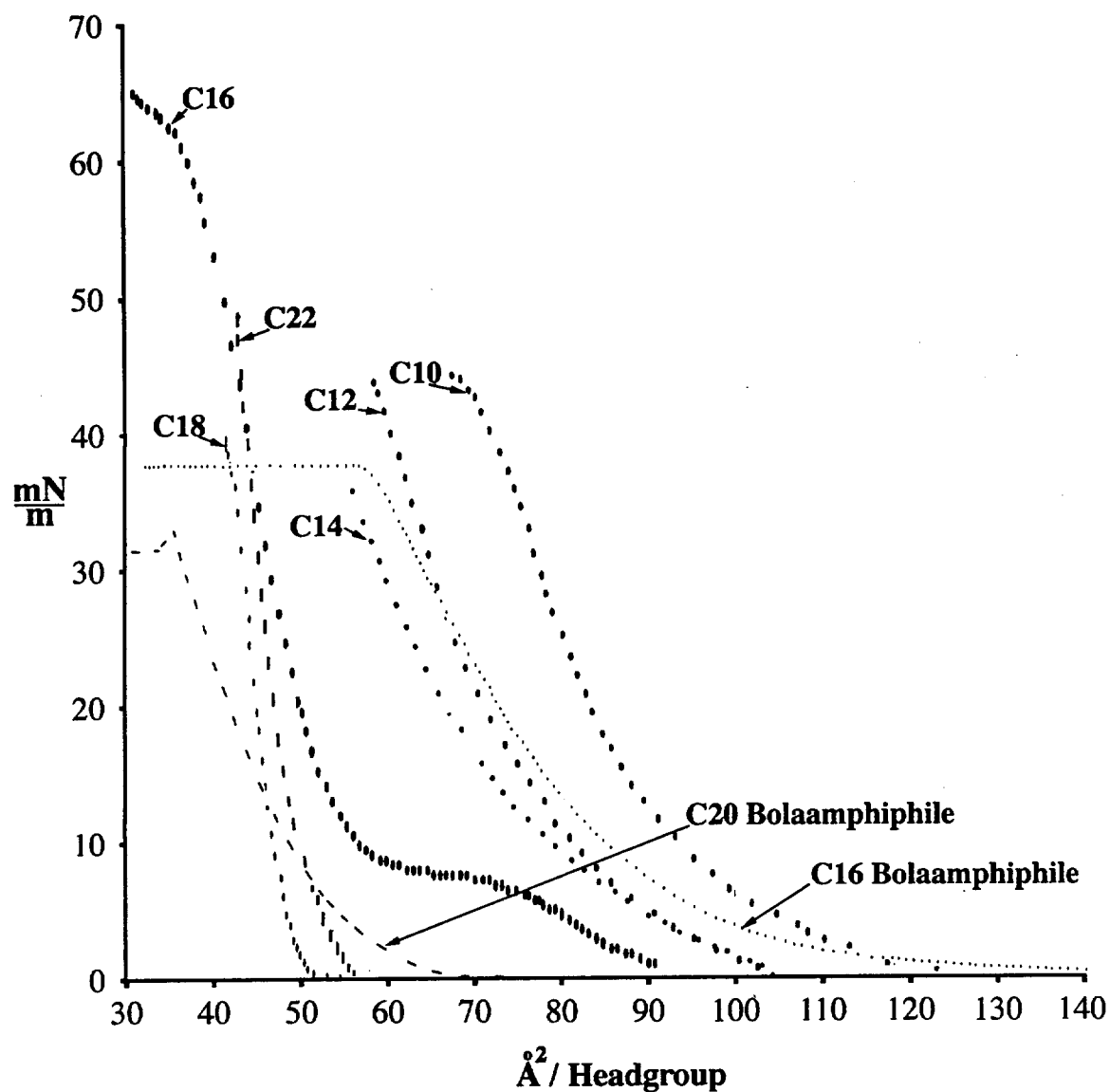


Figure 3.24 A comparison of pressure versus area per headgroup isotherms, acquired at the air-water interface, of several dialkyl phosphatidylcholines (PCs). C10, dicapryoyl PC; C12, dilauroyl; C14, dimyristoyl PC; C16, dilauroyl PC; C18, distearoyl PC; C22 dibehenoyl [from Ref. 2]. In this analysis, the C20 bolaamphiphile behaves more similarly to the longer-chained dialkyl PCs with onset pressure occurring at smaller area than does the C16 bolaamphiphile which resembles the shorter-chained PCs at larger areas.

is a different packing mode than in C20 bolaamphiphiles at the air-water interface (i.e., gas expanded vs. condensed liquid state). The C16 bolaamphiphiles have shorter alkyl chains and fewer hydrophobic interactions than C20 bolaamphiphiles; the shorter chains give rise to a bending stress due to the limit of methylenes that can contribute gauche configurations. It should be noted that the extrapolated area per headgroup is 50 \AA^2 for C20 bolaamphiphile, consistent with the cross-sectional area found by SAXS analysis.

The data from the bolaamphiphile monolayer studies also indicate a demarcation from conventional, monopolar phospholipids in that the latter are capable of sustaining much higher surface pressures than the bolalipids. This can be attributed to losses in translational degrees of freedom per headgroup in the bolaamphiphile system due to the covalent linkage which would limit the film's ability to rapidly respond to changes in surface pressure.

C16 and C20 bolaamphiphiles, although structurally similar, behave uniquely in surface pressure versus area experiments at the air water interface. On the basis of the number of methylenes in which they differ, the differences in phase behavior are consistent with what one observes in a series of dialkyl PCs.

References

1. Marsh, D. (1991) General features of phospholipid phase transitions. *Chem. Phys. Lipids* **57**, 109–120.
2. Helfrich, W. (1974) Blocked lipid exchange in bilayers and its possible influence on the shape of vesicles. *Z. Naturforsch. C* **29**, 510–515.
3. Seddon, J. M., Cevc, G., and Marsh, D. (1983) Calorimetric studies of the gel-fluid (L beta-L alpha) and lamellar-inverted hexagonal (L alpha-HII) phase transitions in dialkyl- and diacylphosphatidylethanolamines. *Biochemistry* **22**, 1280–1289.
4. Seelig, A., and Seelig, J. (1980) Lipid conformation in model membranes and biological membranes. *Q. Rev. Biophys.* **13**, 19–61.
5. Israelachvili, J. N., Mitchell, D. J., and Ninham, B. W. (1977) Theory of self-assembly of lipid bilayers and vesicles. *Biochim. Biophys. Acta* **470**, 185–201.
6. Luzzati, V., Tardieu, A., Gulik-Krzywicki, T., Rivas, E., and Reiss-Husson, F. (1968) Structure of the cubic phases of lipid-water systems. *Nature* **220**, 485–488.
7. Cevc, G., and Marsh, D. (1987) *Phospholipid Bilayers. Physical Principles and Models*, Wiley, New York, p. 370.
8. Luzzati, V., Gulik-Krzywicki, T., and Tardieu, A. (1968) Polymorphism of lecithins. *Nature* **218**, 1031–1034.
9. Marsh, D. (1990) *Handbook of Lipid Bilayers*, CRC Press, Boca Raton, FL, pp. 163–173.
10. Gaines, G. L. (1966) *Insoluble Monolayers at Liquid-Gas Interfaces*, Wiley-Interscience, New York, p. 386.
11. Mingotaud, A.-F., Mingotaud, C., and Patterson, L. K. (1993) *Handbook of Monolayers*, Vol. 1, Academic Press, San Diego, pp. 778–804.

CHAPTER 4

CHARACTERIZATION OF BOLAAMPHIPHILE VESICLES

4.1 Introduction

Phospholipids are capable of spontaneously forming vesicles in aqueous solution when the system is above the chain melting transition temperature. Such vesicles exist as lamella which enclose an aqueous volume. The size of these vesicles can vary from tens of nanometers to tens of microns. Vesicles can be made from lipids such that the resulting membrane serves as a suitable model system for membranes of biological origin. There are many methods of forming vesicles; some of these lead to vesicles with different morphologies and lamellarities. For example, small unilamellar vesicles (SUVs) exhibit the smallest sizes that are possible for phospholipid vesicles; these are most commonly formed by sonication. Other vesicle preparation methods give rise to unilamellar or multilamellar vesicles of varying sizes. These sizes can vary depending upon the ionic strength of the bulk water, the constituents of the membrane, and the processing methods chosen. Multilamellar vesicles (MLVs) are typically formed by simple hydration/vortexing protocols to produce a wide range of sizes up to 10,000 nm. There are also the techniques of high-pressure extrusion through filters of controlled pore size [1] or solvent injection/evaporation to form large unilamellar vesicles (LUVs) which, as the name implies, are single bilayer structures with diameters varying between 50 and 10,000 nm.

Studies conducted to this point have provided information regarding the lyotropic mesomorphism of bolaamphiphile lipids. The conclusion in this regard is that bolaamphiphiles share substantial similarities to conventional phospholipids; i.e., they exhibit lamellar (Gel-liquid crystalline) and vesicular phases. However, they are

lacking in the appearance of hexagonal or cubic phases within the temperature range examined. In the following chapter, attention is focused on the development of these materials for electron transfer and ion translocation studies. For this purpose, the biomimetic vesicular phase of the bolaamphiphiles was chosen in order to emulate the membranes found in natural photosynthesis. To investigate the morphology and stability of the vesicles, bolaamphiphiles were processed by extrusion and the resulting particles analyzed by dynamic light-scattering and cryogenic transmission electron microscopy. These experiments are the focus of this chapter.

4.2 Dynamic Light-Scattering Spectroscopy

4.2.1 Introduction

Dynamic light-scattering spectroscopy (DLS, also called photon correlation spectroscopy or quasielastic light scattering) is a computationally intensive technique in which intensity fluctuations of light caused by particles undergoing Brownian motion in solution are analyzed. When a particle dispersion is illuminated by monochromatic light, intensity fluctuations are generated by differences in light-scattering efficiency of various particles; particle size can be derived from the intensity fluctuation distribution to give the particle translational diffusion coefficient, D . The related Stokes-Einstein diameter can be then determined for the particle [2], assuming that the light scatterer has spherical particle geometry such that the generalized diffusion or Smoluchowski equation is obeyed.

The vesicle diameters obtained from this technique are independent of the composition of the particles or, in dilute ($< 5\%$) dispersions, the particle concentration [3]. The laser radiation employed is non-destructive, and therefore contributes no artifacts which would arise from damage by data acquisition. The experiment provides a "frequency of occurrence of a particle" vs. diameter histogram in 15–30 min from lipid vesicles dispersed in aqueous buffer. The technique is suitable for Gaussian-like unimodal or bimodal distributions where the mean diameters are separated by 100 nm or more, but inadequate for highly polydisperse populations.

4.2.2 Experimental

The dynamic light-scattering (DLS) spectrometer used to study the particle size distribution of extruded vesicle samples was a Nicomp Model 200 Laser Particle Sizer operating at 632.8 nm and 5 mW [4]. The following figures show DLS data for pure C20 bolaamphiphile vesicles and 7:3 C20 bolaamphiphile:cholesterol vesicles which were extruded through 0.08 μm Nuclepore[®] filters using the extrusion protocol [1]. In the case of pure C20 bolaamphiphiles, the particle size distribution (Figure 4.1) indicates non-Gaussian behavior. Attempts to fit this data to spherical particles with finite polydispersity were not successful. The forced fit indicated a mean diameter of between 25 nm to 31 nm with a standard deviation of about 9 nm. Meanwhile the χ^2 values obtained were typically above 100. These two observations indicated that the pure C20 bolaamphiphile structures (vesicles) deviated significantly from the assumed spherical structures. However, it should be noted that for non-spherical vesicles, dynamic light-scattering does not provide information regarding the size of the particles since the Stokes–Einstein equation, used to relate the particle size to its diameter, is not obeyed.

This finding can be understood from the molecular packing parameters for the pure C20 bolaamphiphile. As shown previously, from monolayer and SAXS studies, the C20 bolaamphiphile prefers an elongated, axially symmetric membrane-spanning structure. To form a spherical vesicle, the configuration of the C20 bolaamphiphile must change significantly to accommodate the differential surface areas comprising the inside and outside surfaces of a highly curved structure. This is quite different from monopolar lipids which form bilayer structures. In the later case, the surface area differences can be adjusted by varying the number of amphiphiles on the outer and inner surfaces of the spherical vesicle. However, bolaamphiphiles must adopt some unfavorable U-shaped conformers to accommodate the surface area mismatches produced by vesicles with small radii of curvature. The detailed packing considerations in spherical vesicles have been discussed by Israelachvili [5]. The geometric considerations which must be met to conform to a spherical vesicle morphology depend on the molecular packing fraction. The radius of curvature of the spherical vesicles is given by:

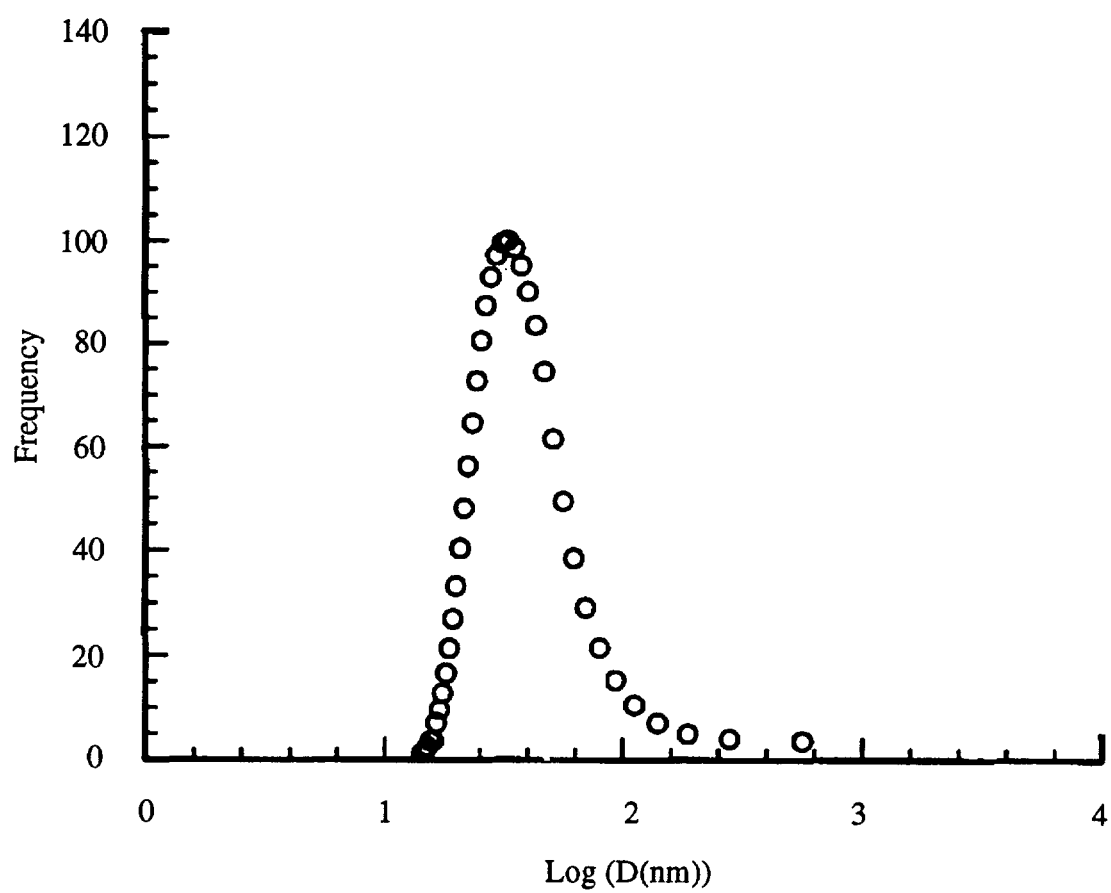


Figure 4.1. Dynamic light-scattering data from pure C20 bolaamphiphiles.

$$R_c = l_c \{3 + \sqrt{3(4P - 1)}\} / 6[1 - P]$$

where P is the packing fraction:

$$P = v/a l_c$$

where v is the molecular volume, a is the cross sectional area, and l_c is the length of the hydrocarbon region of the molecule. Thus, when $P = 1$, i.e., a cylindrical molecule, R_c is infinite, implying a planar structure. When $P = 1/3$, R_c is equal to l_c . In this limit, a micellar structure is expected. When P is between $1/2$ and 1 , a vesicular structure is predicted. Cavagnetto et al. [6] have extended this analysis to binary mixtures of lipids. In this analysis, the packing fraction is recalculated based upon a molar average of the cross-sectional area and molar volume. Thus, the size of the vesicle can be easily controlled in binary mixtures. Since the C20 bolaamphiphile has a cylindrical molecular geometry, cholesterol—which has a wedge shape—was chosen to control the packing parameter and hence the radius of curvature.

C20 bolaamphiphile:cholesterol mixtures. Figure 4.2 shows the diameter distribution for C20 bolaamphiphile:cholesterol mixtures (7:3 molar ratio). The distribution is clearly Gaussian. The χ^2 Gaussian fits were between 2 and 3. This indicates that the fit to a spherical particle shape is justified. The mean particle size distributions in the freshly extruded 7:3 C20 bolaamphiphile/cholesterol (mean diameter of $857 \pm 237 \text{ \AA}$) and the three-day-old samples (mean diameter of $817 \pm 195 \text{ \AA}$) indicate that no vesicle diameter changes occur over a three-day period (average diameter $\cong 840 \text{ \AA}$).

Considering the packing constraints in this binary mixture and assuming that both the bolaamphiphile and cholesterol have a density of one, the combined average lipid molecular volume is 1460 \AA^3 . To calculate the average cross-sectional area for the binary mixtures, the cross-sectional area for cholesterol must be known. It has been determined from the monolayer studies that the cross sectional area for cholesterol is 40 \AA^2 [7]. The cross sectional area for the C20 bolaamphiphile lipid is 68 \AA^2 as determined from both SAXS and monolayer measurements (Chapter 3). The molecular length, l_c , was determined from our SAXS studies. From these measurements, we can calculate the packing fraction to be 0.94. However, the equation relating the mean radius to the packing fraction can be inverted to obtain the

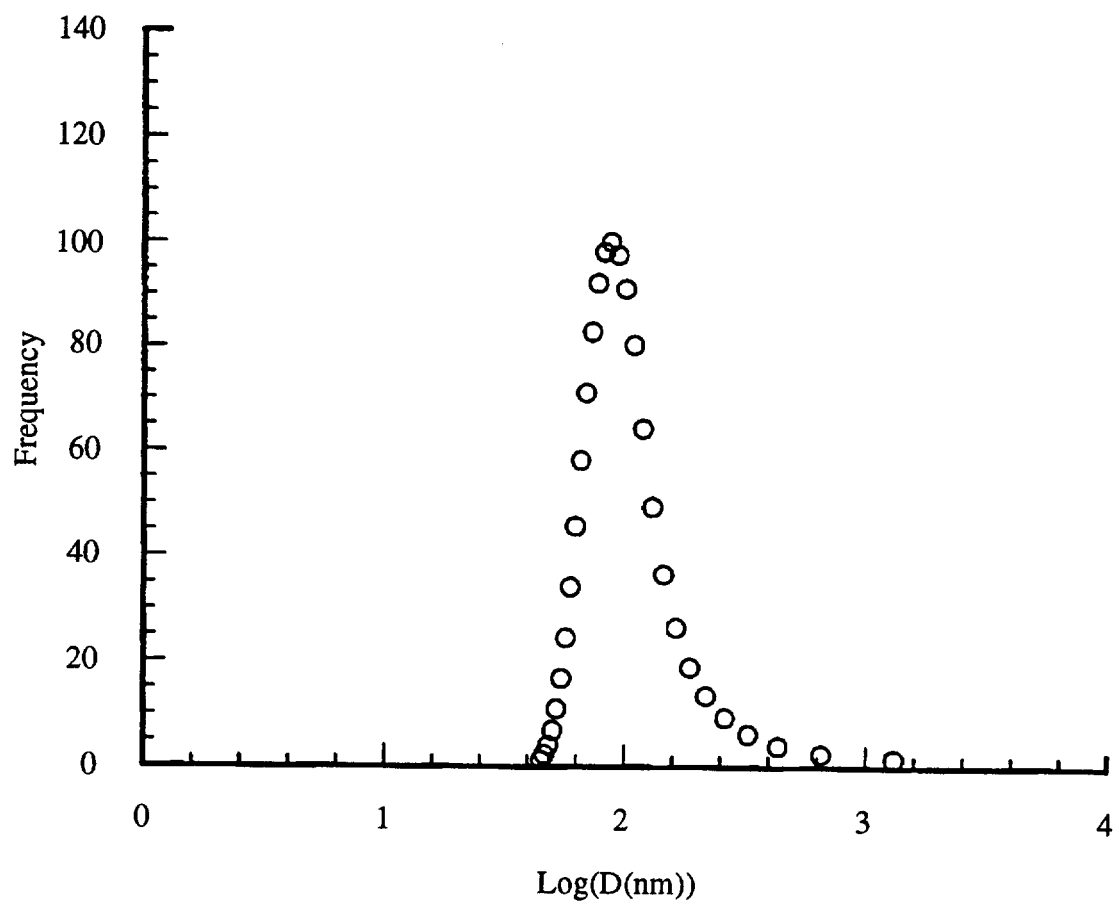


Figure 4.2. Dynamic light-scattering data from C20 bolaamphiphile/cholesterol 7:3 vesicles.

packing fraction since the light-scattering data provides the average radius of curvature (42.6 nm). The packing fraction determined in this way is 0.97. The agreement between these two numbers determined by independent experimental techniques underscores the validity of the foregoing analysis.

The light-scattering data suggested that stable 840 Å vesicles could be produced by extrusion of 7:3 C20 bolaamphiphile:cholesterol. On the other hand, pure C20 bolaamphiphile dispersions would not be reliably characterized using this technique. Therefore, cryogenic transmission electron microscopy was employed to provide additional insights into the supramolecular structures formed by the extruded C20 bolaamphiphile lipid samples.

4.3 Cryo-TEM

The light-scattering studies described in the previous section indicated a possible non-spherical morphology for the pure C20 bolaamphiphile. It was therefore, of interest to determine the nature of the self-assembled structures by cryo-transmission electron microscopy [1,8–10].

This technique was used to observe the morphology of extruded samples of C20 bolaamphiphile, C20 bolaamphiphile:cholesterol and C20 bolaamphiphile:cholesterol:gramicidin [11]. Cryo-TEM is a viable method to visualize vesicle formulations of phospholipids. The micrographs resemble those obtained by light microscopy (i.e., the image is produced from a very narrow focal plane such that the objects appear in cross section), albeit at much higher magnification. The TEM method does not require the addition of staining agents, and therefore has advantages over heavy atom negative staining methods where possible lyotropic phase transitions can be induced by the staining agent.

4.3.1 Experimental method

The experimental technique of cryo-TEM is briefly described here. Pure C20 bolaamphiphile (30 mg, 0.0279 mmol) or the lipid mixtures of C20 bolaamphiphile (30 mg, 0.0279 mmol) and cholesterol (4.6 mg, 0.012 mmol) were subjected to 5

cycles of freezing in liquid nitrogen, thawing, and vortexing to hydrate the lipid. After the lipid was hydrated, the size of the vesicles was selected through 10 cycles of high pressure N₂ extrusion using 0.08 mm polycarbonate membranes. Gramicidin A (30 μl of 0.095 mg/ml, 0.11 mM) was then introduced into the vesicles in the C20 bolaamphiphile:cholesterol:gramicidin A experiments as trifluoroethanol solutions at a rate 2 μl/min, followed by incubation for 90 min at 60°C, and storing at room temperature for three days before analysis. Typically, a drop of the lipid dispersion was transferred to a 400-mesh gold grid by micropipet. The sample was incorporated into the grid and reduced to <50 μ thickness by blotting with filter paper from the opposite side of the grid from which the drop was applied. The sample grid was then rapidly plunged, with a spring-loaded device, into a liquid propane bath cooled to -195°C by liquid N₂. The sample was transported using a Reichert-Jung Model KF80 apparatus to a Zeiss EM 90 electron microscope operating at 60 kV which possessed a liquid N₂ cooled cryostage [8-11]. Precision translation of the cryo-stage, orthogonal with respect to the e⁻ beam, was required to locate vitreous ice having dimensions comparable to those of the vesicles, permitting direct observation of individual vesicles. Various regions of the sample were visualized at random to assess its general nature. Micrographs were then recorded that best represented the overall sample appearance. Micrographs were recorded at 12,500× magnification on photographic film. These were enlarged an additional factor of 2.5× during printing and then digitized using a Lacie Silverscan II interfaced with a Power Mac 6100/60w for data analysis. The images were then analyzed using Adobe Photoshop version 2.5.1 software. The scaling factor was determined by calibrating from optically distinct features. For determining the size of the spheroidal structures, an average of three diameter measurements per particle were used. Particle size distributions were determined from populations of 100–125 particles.

4.3.2 Results

In the pure C20 bolaamphiphiles, vesicle samples prepared at a lipid concentration of 30 mg/ml in 20 mm tris buffer at pH 8 could not be extruded at room temperature; therefore, the samples were extruded at 60°C and incubated in a

60°C bath after extrusion. The vesicle structures observed (Figure 4.3) varied in size, with multilamellar structures and non-spherical morphologies also apparent. Despite the fact that the pure vesicle solutions were extruded through 0.08 μm filters, the observed range of particle sizes was 0.15 μ to 1.5 μ . This outcome could be interpreted in many ways. It is possible that the vesicle sizes are smaller at high temperature or that larger vesicles may be easily distorted to accommodate the passage through the filter pores. The difficulties encountered when attempts were made to filter the vesicle solutions at room temperature can be attributed to the rigidity of the larger-than-pore-sized vesicles.

DLS studies were consistent with the observed morphologies in that very poor fits were obtained for the assumption of spherical structures. Clearly, the data depict not only spherical but highly invaginated structures. For such structures, the generalized Schmoluchowski relationship used to determine spherical particle sizes in light-scattering measurements is not valid. Given the irregular dimensions of pure C20 bolaamphiphile dispersions, particle size distribution analysis was abandoned. However, the data can be interpreted qualitatively. The SAXS studies suggested a membrane-spanning structure of the C20 bolaamphiphile. In such a structure, the packing fraction would be unity. The equation which relates the radius of curvature to the packing fraction indicates that large particle sizes would be favored. If the bolaamphiphile could adopt U-shaped conformations, (i.e., a bilayer structure), then it would be possible to accommodate the surface area mismatch and form smaller-sized spherical particles by enriching the outer membrane surface with U-shaped molecules. Therefore, the C20 bolaamphiphile system is unique with regard to the preferred larger-sized vesicles, compared to the classical phospholipids. Such a system may thus provide large entrapped volumes that could be useful in drug delivery and other liposome technologies.

As pointed out previously, the size of these vesicles can be controlled by tuning the packing fraction through the addition of dopants such as cholesterol. Light-scattering experiments indicated that the addition of cholesterol led to the formation of spherical structures with dimensions on the order of 84 nm. To confirm



Figure 4.3. The cryo-transmission electron micrograph of pure C20 bolaamphiphiles in tris buffer. The white scale bar represents 0.1 micron.

this finding, C20 bolaamphiphile/cholesterol vesicles were studied by cryo-TEM. These vesicles were capable of being extruded at room temperature.

The micrograph of C20 bolaamphiphile:cholesterol 7:3-containing vesicles (Figure 4.4) clearly show predominantly spherical unilamellar vesicles; however, in some instances it was possible to envision composite structures resembling a SUV trapped inside of a LUV. Unlike the pure C20 bolaamphiphiles, these systems did not show significant populations of vesicles with dimensions greater than 100 nm, i.e., greater than the dimensions of the filter pore.

Since our transmembrane electron transfer design requires the incorporation of gramicidin into the synthetic bolaamphiphile vesicles, it was necessary to incorporate gramicidin into C20 bolaamphiphile:cholesterol vesicles using the vectorial insertion protocol (i.e., methodology giving the C-ethanolamine domain at the outer vesicle surface) and verify their morphology by cryo-TEM. In all these studies the concentrations of gramicidin used were $1/4000^{\text{th}}$ the molar lipid concentration. This concentration corresponded to an average of 8 gramicidin molecules per vesicle. To show that this concentration of gramicidin did not induce changes in the morphology of C20 bolaamphiphile/cholesterol vesicles, cryo-TEM images were obtained. The micrograph in Figure 4.5 shows the presence of vesicles. Comparison of the size distribution derived from cryo-TEM analysis with particle size distribution from light scattering indicates that the average dimensions of the vesicles from the EM analysis is 85 ± 25 nm, compared to 85 ± 23 nm from light scattering. The agreement between two values is remarkable and suggests that subsequent studies with the extruded 7:3 C20 bolaamphiphile:cholesterol can assume a 85-nm particle size distribution with high confidence. The gramicidin-containing vesicles were subjected to the same form of data handling and the resulting average dimensions of the vesicles was 77 ± 17 nm.

As indicated before, electron microscopy and light-scattering techniques both have their strengths and limitations. However, within the limits of the measurements, however, we have shown that spherical vesicles containing gramicidin A can be formed and are stable over a three-day period.

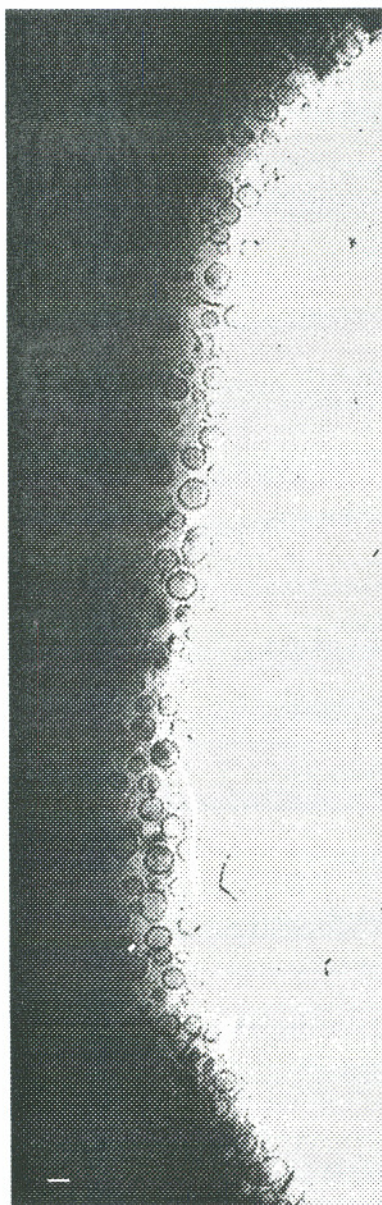


Figure 4.4. Cryo-transmission electron micrograph of 7:3 C20 bolaamphiphile:cholesterol vesicles in tris buffer. The white scale bar represents 0.1 micron.

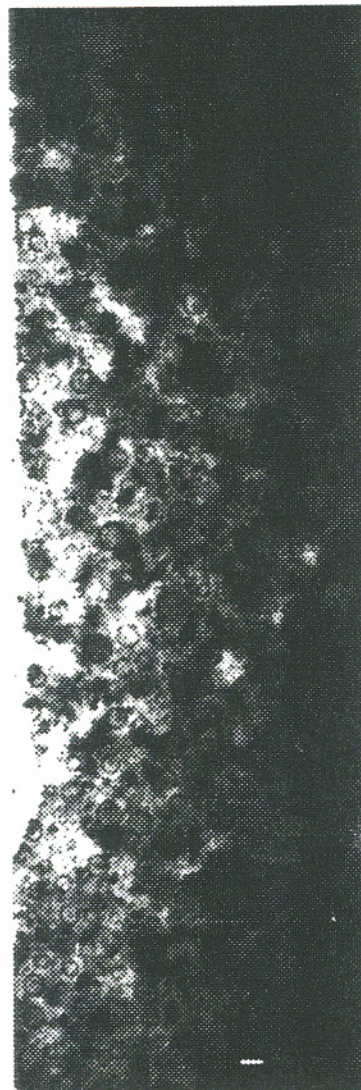


Figure 4.5. Cryo-transmission electron micrograph of 7:3 C20 bolaamphiphile:cholesterol vesicles after insertion of gramicidin A. The spherical vesicle morphology is preserved. The white scale bar represents 0.1 micron.

4.3.3 Discussion

The differences noted between the pure C20 bolaamphiphile and cholesterol-containing vesicles can be partially explained by considering the shape of the lipid. If the lipid assumes a membrane-spanning arrangement in the lamella as suggested by SAXS data, spherical vesicles having a membrane thickness of 27 Å (Chapter 3) must have different inner and outer surface areas, based on simple curvature requirements. In vesicles composed of pure C20 bolaamphiphiles, where the number of lipids on the inside and outside of the vesicles is the same due to the bipolar nature of the lipid, problems occurred in the attempts to extrude the vesicles at room temperature. The possibility of U-shaped C20 bolaamphiphiles occurring on the outer surface to accommodate the differences in relative surface area may be energetically disfavored due to the unfavorable turn which must occur in the membrane-spanning segment for such a U-shape configuration to exist. However, elevated temperature may provide sufficient thermal energy, allowing a reorganization of lipid in the membrane during extrusion. After elevated temperature extrusion of the C20 bolaamphiphile, the invaginated structures observed in the cryo-TEM micrographs probably represent an attempt to average the inside and outside surface areas through currently unknown lipid dynamics. An alternative interpretation is that the large irregular structures represent a kinetically trapped intermediate state that may be undergoing successive cycles of aggregation and fusion.

Cholesterol-containing C20 bolaamphiphile vesicles, however, were capable of being extruded at room temperature to give spherical vesicles. Presumably, the cholesterol occupied the needed area on the outer surface to stabilize the structure. Inclusion of gramicidin in these dispersions showed no deleterious effects upon the structure of C20 bolaamphiphile/cholesterol vesicles. This has important consequences for the design of photosynthetic devices. These considerations will be addressed in more detail in Chapter 5.

4.4 References

1. Hope, M. J., Bally, M. B., Webb, G., and Cullis, P. R. (1985) Production of large unilamellar vesicles by a rapid extrusion procedure. Characterization of size distribution, trapped volume and ability to maintain a membrane potential” *Biochim. Biophys. Acta* **812**, 55–65.
2. (a) Berne, B. J. and Pecora, R. (1976) *Dynamic Light Scattering*. W. J. Wiley, New York.
(b) Ford, N. C., Jr. (1985) Light scattering apparatus. In *Dynamic Light Scattering. Applications of Photon Correlation Spectroscopy* (Pecora, R., Ed.), Plenum Press, New York, pp. 7–57.
3. Menger, F. M., Lee, J., Aikens, P., and Davis, S. (1989) Vesicle size: Dependence on experimental parameters. *J. Colloid Interface Sci.* **129**, 185–191.
4. Bantle, S., Schmidt, M., and Burchard, W. (1982) Simultaneous static and dynamic light scattering. *Macromolecules* **15**, 1604–1609.
5. Israelachvili, J. (1985) *Intermolecular and Surface Forces*, Academic Press: San Diego, pp. 255–259.
6. Cavagnetto, F., Relini, A., Mirghani, Z., Gliozzi, A., Bertoia, D., and Gambacorta, A. (1992) Molecular packing parameters of bipolar lipids. *Biochim. Biophys. Acta* **1106**, 273–281.
7. Hirshfeld, C. L. and Seul, M. (1990) Critical mixing in monomolecular films: Pressure-composition phase diagram of a two-dimensional binary mixture. *J. Phys. (Paris)* **51**, 1537–1552.
8. Bellare J. R., Davis, H. T., Scriven, L. E., and Talmon, Y. J. (1988) Controlled environment vitrification system—an improved sample preparation technique. *Electron Microsc. Tech.* **10**, 87–111.
9. Dubochet, J., Adrian, M., Chang, J.-J., Homo, J.-C., Lepault, J., McDowall, A., and Schultz, P. (1988) Cryo-electron microscopy of vitrified specimens. *Q. Rev. Biophys.* **21**, 129–228.
10. Vinson, P. K., Bellare, J. R., Davis, H. T., Miller, W. G., and Scriven, L. E. (1991) Direct imaging of surfactant micelles, vesicles, disks, and ripple phase structures by cryo-transmission electron-microscopy *J. Colloid Interface Sci.* **142**, 74–91.

11. Thompson, D. H., Wong, K. F., Humphry-Baker, R., Wheeler, J. J., Kim, J.-M., and Rananavare, S. B. (1992) Tetraether bolaform amphiphiles as models of archaebacterial membrane-lipids: Raman-spectroscopy, ^{31}P NMR, X-ray scattering, and electron-microscopy. *J. Am. Chem. Soc.* **114**, 9035-9042.

CHAPTER 5

TESTING OF THE BOLAAMPHIPHILE-GRAMICIDIN-PORPHYRIN DESIGN CONCEPT

The purpose of the previous chapters was to demonstrate that stable vesicles of C20 bolaamphiphile:cholesterol in the presence of gramicidin A-porphyrin (GAP) could be constructed. To realize the design concept, asymmetric insertion of the GAP complex in C20 bolaamphiphile:cholesterol vesicle membranes was essential for promoting vectorial photoinduced transmembrane electron transfer. Moreover, realization of the coupled ion- and electron-transfer process required proof that the channel still functioned, despite having been chemically modified. This chapter will discuss the photochemical studies that were employed to determine the orientation of GAP in the C20 bolaamphiphile:cholesterol vesicle membranes and sodium NMR experiments to determine the ability of the channels to conduct sodium ions.

5.1 Flash Photolysis

5.1.1 Introduction

The results from the physical characterization of the 7:3 C20 bolaamphiphile:cholesterol vesicles suggested that these particles are sufficiently stable to serve as a host membrane system to test the model based on modified gramicidin A. These modifications involve the addition of a porphyrin (coupled to the N-terminus of the gramicidin) as a photochemical reducing agent (see Chapter 2) and water-soluble *N,N'*-dimethyl-4,4'-bipyridinium ions (methylviologen or MV^{2+}) as an oxidant. This system was chosen on the basis of work by Hurst and co-workers [1–3]. These studies used egg phosphatidylcholine (EggPC) in one case and dihexadecylphosphate (DHP) in another case, in which the photochemically generated redox pair were

separated across vesicle bilayers to prevent recombination [2,3]. The photochemical reaction between a porphyrin and MV^{2+} proceeds by photoexcitation of the porphyrin to give a triplet excited state, which transfers an electron to the MV^{2+} to yield a blue methylviologen radical (MV^+) and a porphyrin π -cation. The lifetime of this charge-separated state is strongly dependent on vesicle topology and solution conditions [2].

Since transmembrane electron transfer is electrogenic in the absence of compensating ion translocation, a membrane potential develops which counters further reaction. A significant membrane potential develops even after a few charged species are translocated across small liposomes [1]. The complex process of transmembrane oxidation-reduction followed by lipophilic ion transport across liposome membranes has been subjected to careful studies [4-6]. This work has shown that transmembrane electron transfer can occur in vectorially organized vesicle configurations [4]. In one example, hydrophilic reductants added to the vesicle's external aqueous phase were able to transfer electrons to oxidants entrapped in the vesicle's interior with correlated carrier-mediated (carbonyl cyanide *p*-trimethoxyphenylhydrazone) transfer of protons to the vesicle interior [7]. The acidification of the vesicle's interior provided evidence of electron transfer since the development of a proton gradient could only occur if a redox reaction was polarizing the membrane.

In another example, dihexadecylphosphate vesicle-bound MV^{2+} was reduced from across the membrane by dithionite ion with correlated transmembrane movement of one MV^+ radical or some other lipophilic cation per electron [8,9]. The fact that methylviologen is transferred across the membrane demonstrates that transmembrane redox had occurred; however, the mechanism by which it proceeds could not be ascertained from the experiment. To distinguish between mechanisms involving transverse diffusion of the redox components from transmembrane electron transfer pathways, the diffusion rates of these processes were compared. This approach was used in the Hurst laboratory to study viologen-mediated reduction of N-alkyl-N'-methyl-4,4'-bipyridinium ions (C_nMV^{2+}) across dihexadecylphosphate bilayer membranes [2,10]. In these experiments, the comparison of various chain-length viologens indicated that there were two pathways by virtue of (a) the degree of transmembrane redistribution resulting from the reaction, (b) the relative rates of

viologen diffusion (as obtained from ^{14}C -radioisotope labeling) and transmembrane redox, (c) the effects of lipophilic ions on the enhancement of transmembrane redox rates [2,10]. For short-chained C_nMV^{2+} ($n \leq 10$), the pathway was diffusionally governed, and there was about a 1:1 ratio in the transfer of C_nMV^+ radical cation with each transferred electron. Meanwhile, translocation of longer-chained C_nMV^{2+} ($n > 10$) across the membrane did not occur on the timescale of the redox reaction; the addition of other lipophilic ions was required to promote the electron transfer reaction, by dissipating the membrane potential. Given the inability of the longer-chained C_nMV^{2+} ($n > 10$) to traverse the membrane bilayer, electron transfer had to have occurred between C_nMV^+ and C_nMV^{2+} , on opposite sides of the bilayer. These findings may be based upon differences in the modes of binding between the short- and long-chained C_nMV^{2+} . The longer-chained C_nMV^{2+} have a greater possibility to aggregate within the membrane, while the shorter-chained analogs bind to the membrane at the aqueous interface [2,11–15]. The detailed kinetic data collected by the Hurst group illustrated that a transmembrane diffusive mechanism can serve to dissipate membrane potentials (which impede further electron transfer). Alternative interpretations, e.g., disproportionation of the viologen radical into MV^{2+} and MV^0 followed by diffusion of the neutral MV^0 have also been proposed [16]. Regardless of the detailed molecular pathway followed, however, it is clear that the membrane potential must be dissipated if transmembrane electron transfer rates are to be significant.

The GAP diad was designed to dissipate membrane potentials by permitting the transfer of cations in response to membrane potentials generated by electron transfer across the C20 bolaamphiphile:cholesterol vesicle membrane. To determine if GAP was capable of being configured in a GAP:C20 bolaamphiphile:cholesterol system such that it was photochemically active, flash photolysis and bulk photolysis experiments were performed.

The flash photolysis technique has been used to investigate electron transfer reactions from porphyrins to methylviologen. In this method, the triplet state lifetimes are measured. Electron transfer quenching between the porphyrin triplet and MV^{2+} can diminish the porphyrin triplet state lifetime in a concentration-dependent

manner. Studies in the Hurst laboratory have employed aqueous porphyrins, sacrificial electron donors, and amphiphilic N-alkyl-N'-methyl-4,4'-bipyridinium ions bound to the surface of dihexadecylphosphate or egg phosphatidylcholine membrane vesicles. Physical separation of the donors in the aqueous phase and the acceptors in the lamellar phase greatly increases the lifetime of the charge separated pair from submicrosecond to millisecond timescales [17].

To reduce the mechanistic complexity caused by diffusing species which was found in the above models for photoinduced electron transfer across vesicle membranes, we have chosen a different approach. A model has been envisioned which incorporates both the donor and the acceptor within an ion channel linker to improve charge separation efficiency and by utilizing a size-matched environment for maintaining the photogenerated charge gradient (Figure 5.1). This approach utilizes an oriented membrane-spanning ion channel modified with a porphyrin and a quinone for photochemical generation of a charge-separated pair. An ultrathin membrane is also used which should both accelerate the rate of transmembrane electron transfer by reducing the separation distance between the porphyrin and quinone and permit the function of the ion channel which dissipates the charge gradient. Gramicidin A modified with a porphyrin and quinone (GAPQ) would serve as the phototransducer in this design while C20 bolaamphiphiles:cholesterol vesicles would serve as the GAPQ's host matrix that forces the gramicidin to form a monomeric ion channel instead of the dimer exploited by *Bacillus brevis* [18,19].

There are several advantages to be gained by this composite system. Since the gramicidin A portion of the GAPQ would serve in the thin membrane-forming C20 bolaamphiphile:cholesterol case as a membrane-spanning ion channel, it should permit the balance of charge across the membrane associated with transmembrane photoinduced electron transfer. (Details concerning the ion transport will be discussed in the sodium NMR section.) The orientation of GAPQ may be controlled by exploiting the natural preference for it to insert with the tryptophan residues facing the aqueous interface, and using a hydrophobic porphyrin moiety such that it initially inserts into the hydrophobic region of the C20 bolaamphiphile:cholesterol vesicle membrane [20,21]. To test this hypothesis, we investigated two types of viologens as

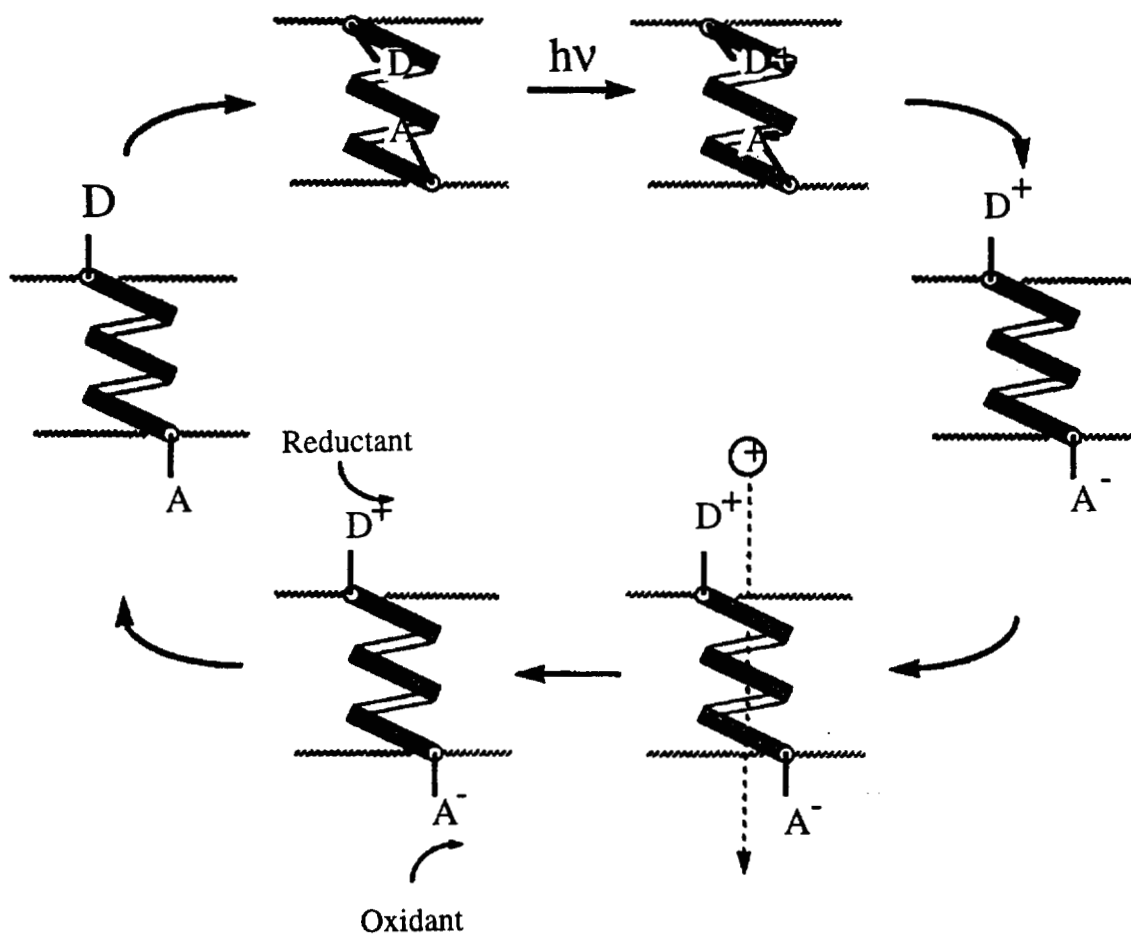


Figure 5.1 Schematic cycle depicting GAPQ function in a C20 bolaamphiphile:cholesterol vesicle membrane. The porphyrin donor (D) and the quinone acceptor (A) are attached at opposite sides of the channel. When light strikes the porphyrin, electron transfer to the quinone should occur. This transmembrane electron transfer generates a membrane potential, and the gramicidin channel responds by transferring a proton which dissipates the potential. When coupled to secondary reactions, the donor may then be reduced, while the quinone is oxidized, thereby restoring the system to the original state and permitting the next cycle.

electron acceptors, amphiphilic decylviologen and hydrophilic methylviologen. In this way, if porphyrin were to reside on the outer surface of the vesicle, after addition of GAP to previously extruded C20 bolaamphiphile:cholesterol (7:3) vesicles, quenching of the triplet state lifetime would be expected in the presence of methylviologen. The photochemical reactions were carried out utilizing the experimental set-up and protocols given below.

5.1.2 Experimental

5.1.2.1 Flash Photolysis

Flash photolysis experiments were conducted using a set-up shown in Figure 5.2. The triplet state lifetime of the porphyrin-derivatized gramicidin was monitored through changes in transmission of a continuous beam of light supplied by a 150 W HgXe lamp operating with a stabilized DC power supply. The light beam passed through a two-lens condenser, an aqueous heat filter, a light glass filter, and an electrical shutter before reaching the 1 cm × 1 cm cuvette sample compartment. After passing through the sample, the light passed through a focusing lens followed by a Bausch & Lomb F/3.5 monochromator into the photomultiplier tube. The resulting signal was sent to a Nicolet 4094B 12-bit digitizing oscilloscope which housed a 4562 plug-in. The triplet state was generated by utilizing a Xenon model 457 micropulser that triggered the oscilloscope and delivered 100 Joules/flash, with a halfwidth of $\sim 5 \mu\text{s}$. Before impinging the sample, the flash passed through a glass filter and a focusing lens.

The lipid mixture of C20 bolaamphiphile (10 mg, 0.0093 mmol) and cholesterol (1.54 mg, 0.0040 mmol) was extruded through 0.08 μ Nucleopore filters in 1.0 ml of 20 mM tris buffer, pH 8. GAP was then added by manual addition of 30 μl solution (0.28 mg/ml, 0.11 mM) GAP in trifluoroethanol over a 15-min period. The system was then purged with oxygen-free argon for 20 minutes. The triplet state lifetime was then recorded using an observation wavelength of 470 nm. 200 μl of 3.6 mM methylviologen was added, making the system 0.6 mM in methylviologen, and the triplet state lifetime was again recorded. The data are presented in Figure 5.3. The first-order plots (Figure 5.4) yielded decay constants of $2.6 \times 10^{-3} \text{ s}^{-1}$ in the

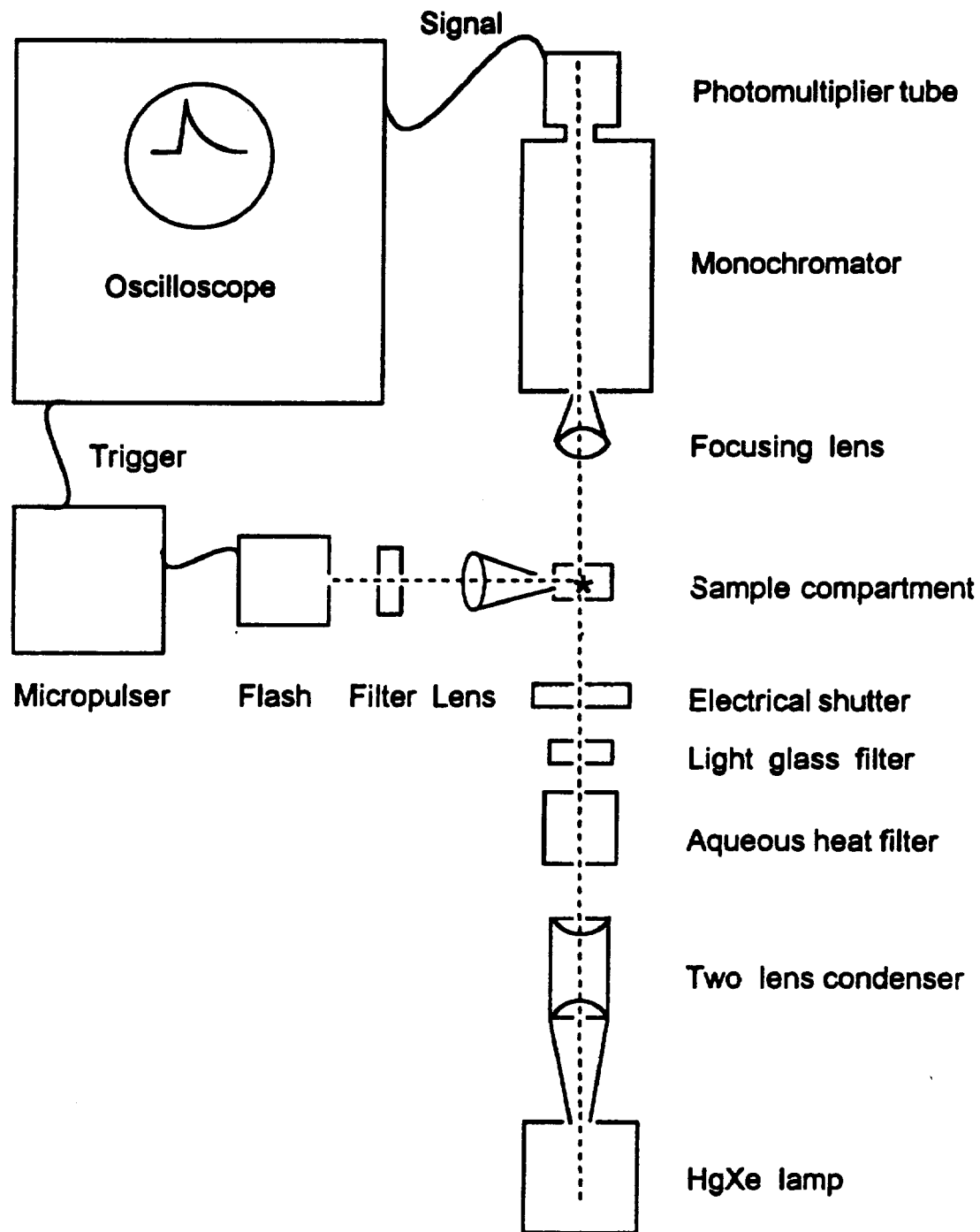


Figure 5.2 Schematic diagram showing experimental flash photolysis setup used for the triplet state lifetime measurements of GAP inserted in C20 bolaamphiphile: cholesterol vesicles. A micropulser generates a flash of light which passes through a filter, then a lens, before impinging the sample. An electrical shutter then opens and permits focused, filtered light to pass through the sample and enter a photomultiplier tube where a signal is generated. The signal is then sent to a digitized oscilloscope and stored for data processing.

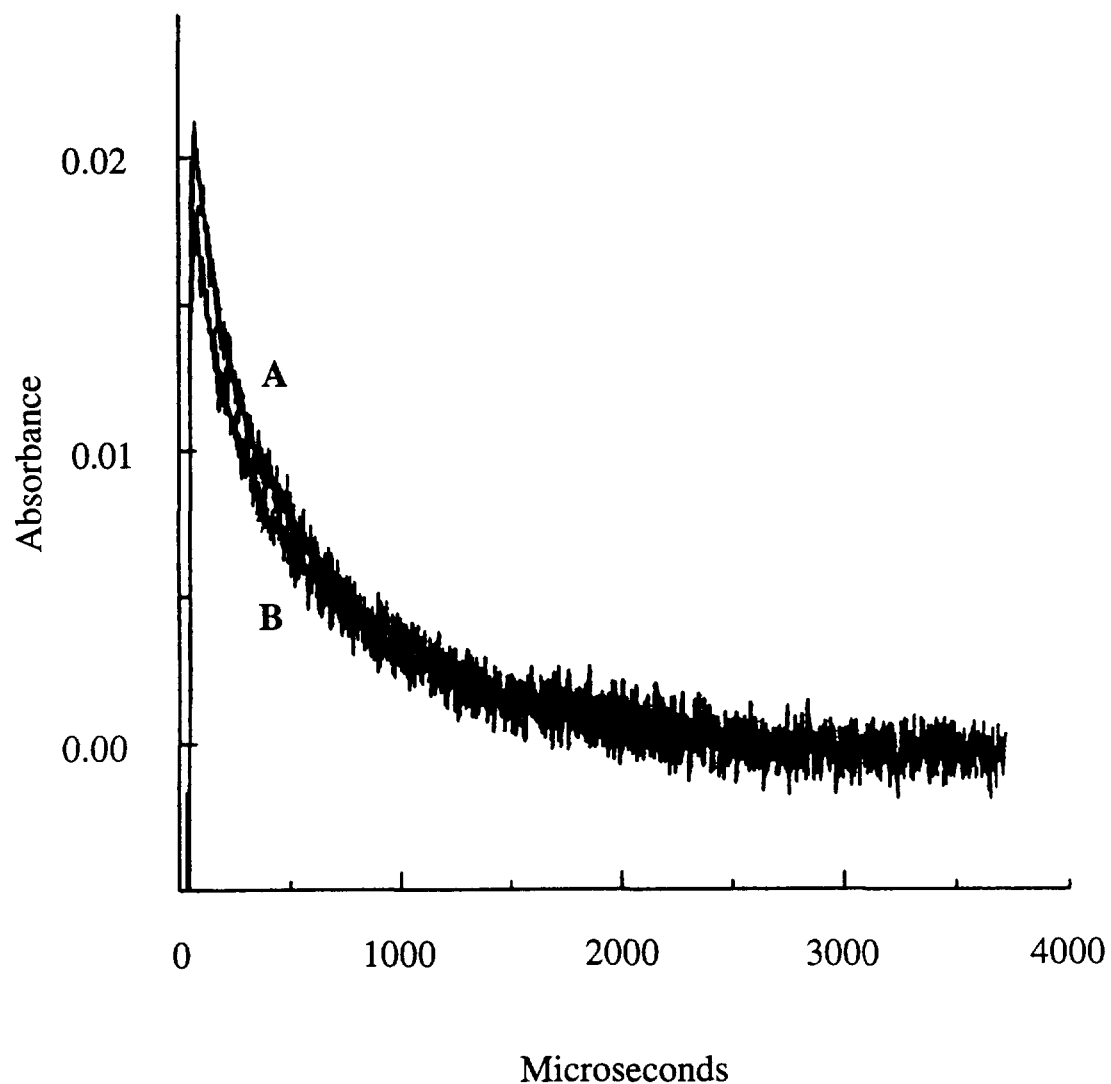


Figure 5.3 Triplet state lifetimes measured by flash photolysis of the GAP diad inserted into deoxygenated vesicles of 7:3 C20 bolaamphiphile:cholesterol in 20 mM tris buffer, pH 8. (A) In the absence of methylviologen; (B) in the presence of 0.6 mM methylviologen. The change in absorbance is attributed to the dilution associated with addition of the methylviologen solution.

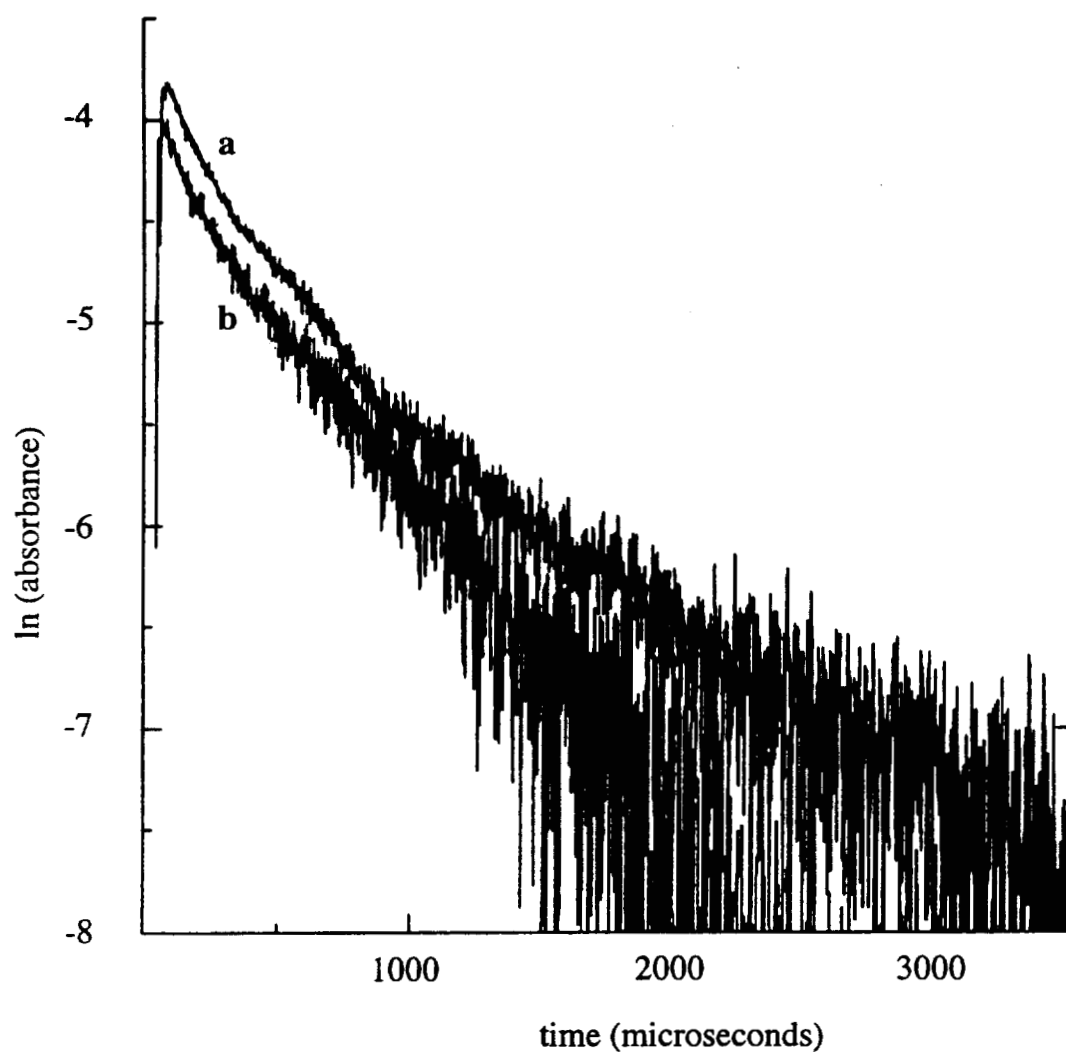


Figure 5.4 First-order plots of GAP porphyrin triplet states from the experiments conducted in 7:3 bolaamphiphile:cholesterol vesicles. (a) In the presence of methylviologen yielding a rate constant of 0.0026/sec; (b) in the presence of methylviologen 0.6 mM outside of the vesicle yielding a rate constant of 0.0028/sec. These are similar and indicate that the porphyrin is not accessible to the methylviologen.

absence of methylviologen and $2.8 \times 10^{-3} \text{ s}^{-1}$ when the concentration was 0.6 mM methylviologen outside. The pseudo first-order rate (decay) constant k_{decay} can be expressed as:

$$k_{\text{decay}} = k_{\text{nr}} + k_{\text{q}}[\text{Q}]$$

where k_{nr} is the non-radiative decay ($2.6 \times 10^{-3} \text{ s}^{-1}$), k_{q} is the diffusion limit ($10^9 \text{ M}^{-1} \text{ s}^{-1}$) and $[\text{Q}]$ is the concentration of methylviologen. This yields a k_{decay} of $6 \times 10^5 \text{ s}^{-1}$. The similarity ($2.6 \times 10^{-3} \text{ s}^{-1}$ versus $2.8 \times 10^{-3} \text{ s}^{-1}$) of the decay constants in the absence and presence, respectively, of methylviologen suggests that the porphyrin moiety was inaccessible to methylviologen quenching. Prior studies of methylviologen binding to phosphocholine vesicles indicate that these interactions are weak [1]. These experimental results are consistent with the notion that the lipophilic porphyrin inserts into the bolaamphiphile membrane vectorially to give an asymmetric vesicle architecture with the porphyrin moiety facing the inside of the vesicle (Figure 5.5).

5.1.2.2 Steady-State Photolysis

Bulk photolysis experiments were conducted to determine if photoinduced electron transfer could be promoted from GAP [inserted into C20 bolaamphiphile:cholesterol vesicles containing ethylenediaminetetraacetic acid (EDTA) as a sacrificial electron donor] to N-decyl-N'-methyl-4,4'-bipyridinium ions (C10 MV²⁺) added to the outside of the vesicles. The lipid mixture of C20 bolaamphiphile (10 mg, 0.0093 mmol) and cholesterol (1.54 mg, 0.0040 mmol) was extruded through 0.08 μ Nucleopore filters in 1.0 ml of 20 mM tris buffer, pH 8, containing 1.0 mM EDTA. The EDTA was removed from the outside of the vesicles by employing a Sephadex G-50 size exclusion column. 30 μ l of (0.28 mg/ml, 0.11 mM) GAP was then manually added to the vesicles as a trifluoroethanol solution over 15 min. C10 MV²⁺ was added to the outside of the vesicles to give a 25- μ M concentration (Figure 5.6). The sample was included in a cuvette and deoxygenated by bubbling with argon for 30 minutes. The system was illuminated with filtered light from a 100-W high-pressure xenon lamp (Oriel Model C-60-80). The light beam was passed through a water cell (10 cm path length) followed by a Corning 3-75 UV cut-off and a CS-470 blue-green filter before irradiating the magnetically stirred sample. The

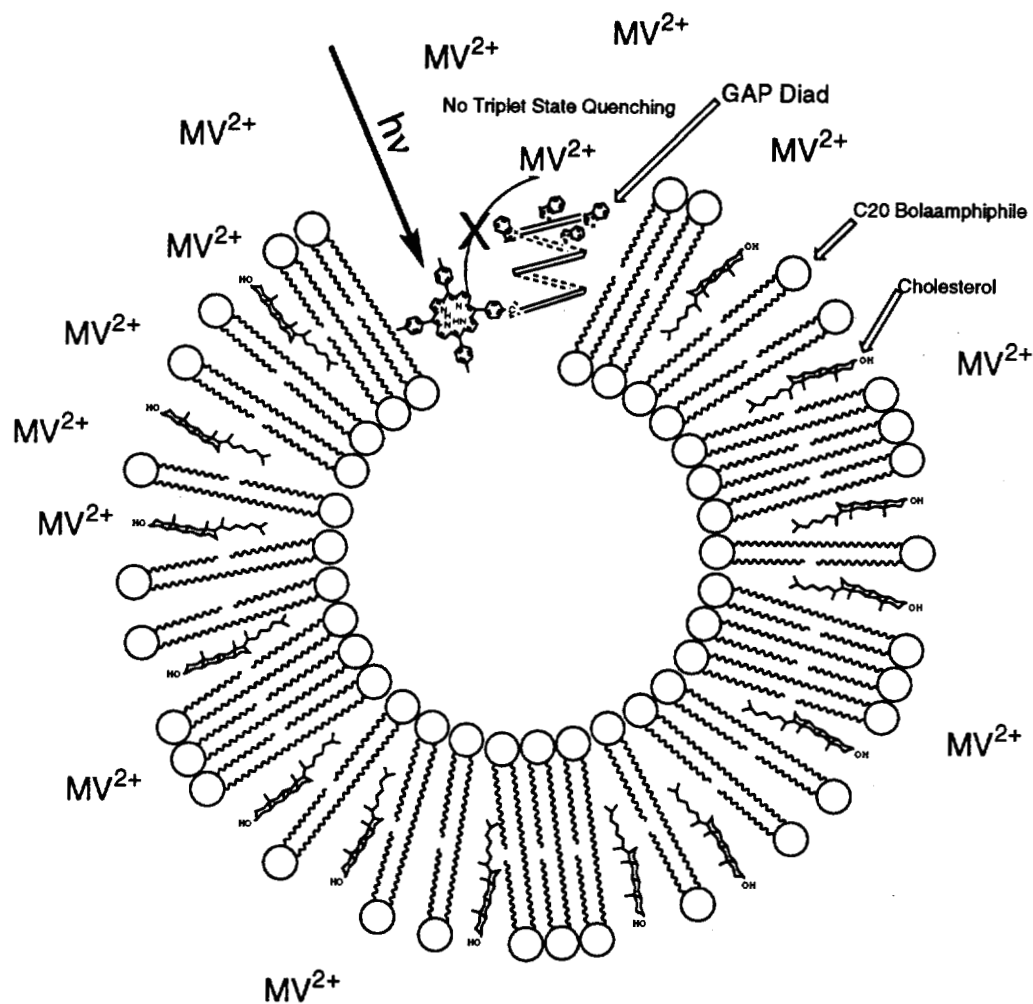


Figure 5.5 Schematic diagram showing GAP inserted into preformed 7:3 C20 bolaamphiphile:cholesterol vesicles. Flash photolysis in the presence of 0.6 mM N,N'-dimethyl-4,4'-bipyridinium ions (methylviologen) did not result in triplet state quenching. This is consistent with the depicted vesicle geometry.

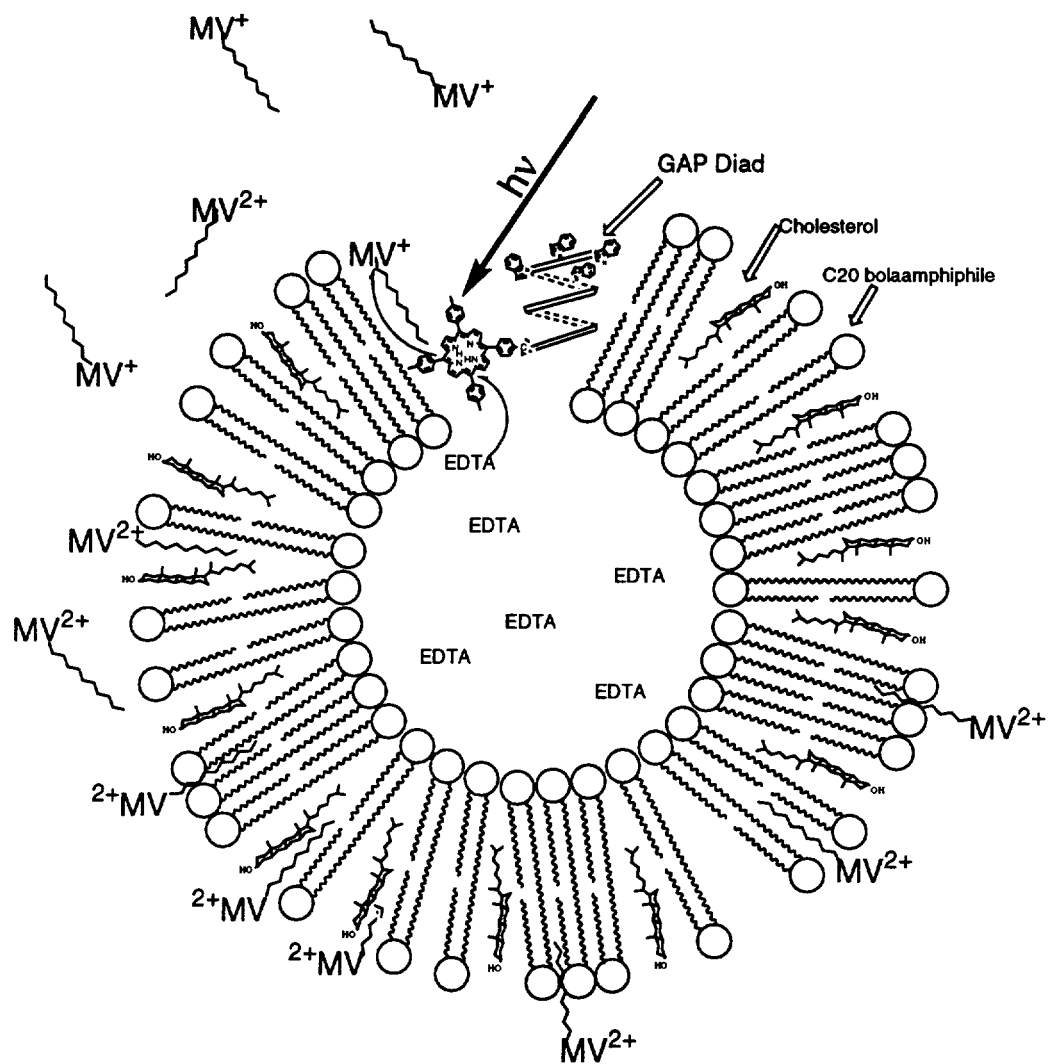


Figure 5.6 Schematic diagram showing GAP inserted into preformed 7:3 C20 bolaamphiphile:cholesterol vesicles with intravesicular EDTA. Bulk intravesicular photolysis in the presence of N-decyl-N'-methyl-4,4'-dipyridinium ions (C10 MV^{2+}) added to the outside of the vesicles indicated that electron transfer between the porphyrin and C10 MV^{2+} was occurring to form C10 MV^+ . This is attributed to the ability of the amphiphilic C10 MV^{2+} to partition into the vesicle.

photochemical reaction was monitored by removing the cuvette from the light source and collecting the absorption spectrum using a Hewlett-Packard 8452A diode array spectrophotometer.

In the absence of a microcompartment to separate the reactants, the porphyrin π -cation can be reduced by a sacrificial electron donor such as EDTA to a persistent methylviologen radical [1]. In our experiment, C10 MV⁺ radicals were detected in a time-dependent experiment by UV-Vis spectroscopy, as characterized by the appearance of a strong sharp band at 395 nm and a broad absorption throughout the visible region centered at 602 nm. The appearance of the C10 MV⁺ radicals indicate that photoinitiated electron transfer was occurring (Figures 5.7 and 5.8). This is consistent with the findings of Kuhn and Hurst who observed that C10 MV²⁺ has a significantly greater binding constant to the interface of egg phosphatidylcholine membranes than MV²⁺ [1]. In contrast to anionic dihexadecylphosphate vesicles, photostimulated diffusion of entrapped N,N'-diheptyl-4,4'-bipyridium ions does not occur in egg phosphatidylcholine vesicles [1,3]. This is likely due to the zwitterionic headgroup of the phosphatidylcholine headgroup which does not bind to the positively charged viologens as does the anionic headgroups of dihexadecylphosphate. Therefore, we conclude, on the basis of Kuhn's results and our own observations, that C10 MV²⁺ binds close to the hydrophobic region of the bolaamphiphile membrane due to the amphiphilic character of this electron acceptor. This partitioning is believed to facilitate the electron transfer from the porphyrin moiety by decreasing the distance between the redox pair (i.e., ³P and C10 MV²⁺).

Taken together, the flash and bulk photolysis experiments are both consistent with the proposed geometrical configuration in the C20 bolaamphiphile:cholesterol (Figures 5.5 and 5.6). Other configurations, however, may also explain the observations. If the porphyrin moiety is buried in the hydrophobic region of the C20 bolaamphiphile:cholesterol membrane regardless of the orientation of the GAP (i.e., through a random coil state of GAP or by partial insertion; Figure 5.9), the MV²⁺ would still be inaccessible and quenching in the flash photolysis experiment would not be observed.

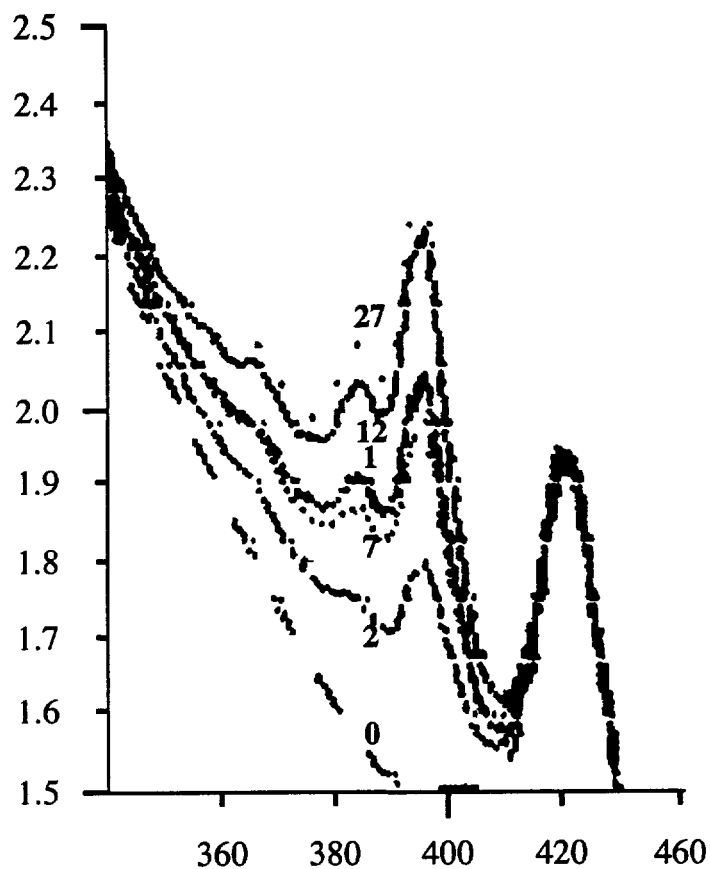


Figure 5.7 Spectra indicating the progress of photoinduced electron transfer in 7:3 C20 bolaamphiphile:cholesterol vesicles with the GAP diad inserted. These vesicles contain a 1.0 mM solution of EDTA inside and N-decyl-N'-methyl-4,4'-bipyridinium ions ($C_{10} MV^{2+}$) outside. $C_{10} MV^+$ radicals appear upon illumination, as indicated by the strong band at 395 nm. The total illumination times in minutes are printed on the spectra. The increase in the 395-nm band indicates that electron transfer, from the porphyrin attached to the GAP to $C_{10} MV^{2+}$, is taking place.

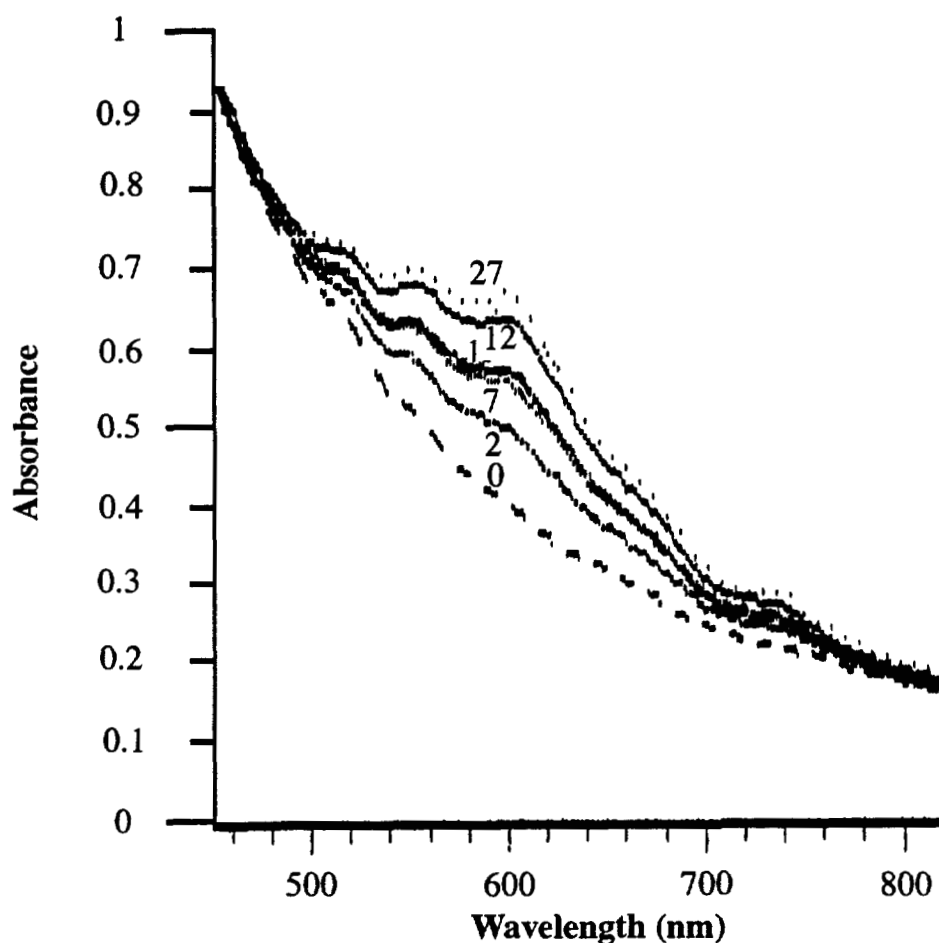


Figure 5.8 Expanded spectra indicating the progress of photoinduced electron transfer in 7:3 C20 bolaamphiphile:cholesterol vesicles with the GAP diad inserted. These vesicles contain a 1.0 mM solution of EDTA inside and N-decyl-N'-methyl-4,4'-bipyridinium ions (C10 MV²⁺) outside. C10 MV⁺ radicals appear upon illumination as indicated by the broad band centered at 602 nm. The total illumination times in minutes prior to the acquisition of the spectra are printed on the spectra. The increase in absorbance in the region band verifies that electron transfer, from the porphyrin attached to the GAP to C10 MV²⁺, is taking place.

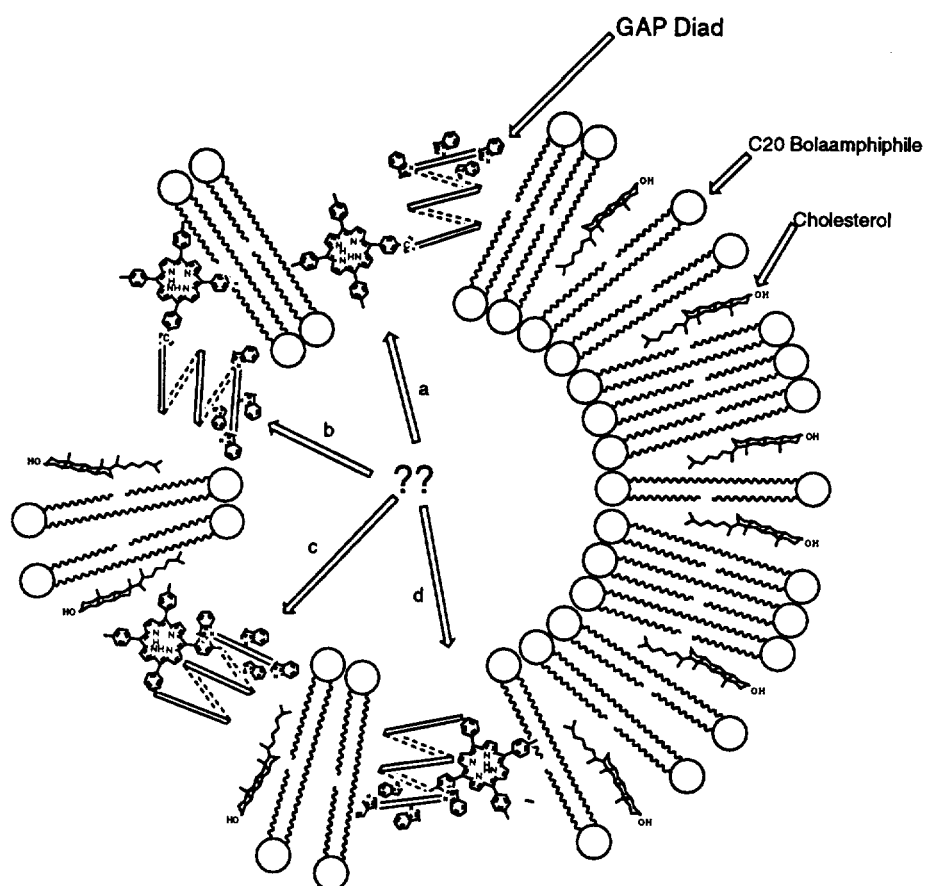


Figure 5.9 Schematic diagram showing possible orientations of GAP in a 7:3 C20 bolaamphiphile:cholesterol vesicle. (a) The porphyrin inserts first with tryptophan residues facing the external aqueous phase; (b) tryptophans insert first followed by the porphyrin; (c) as in b, but the porphyrin is buried in the membrane; (d) porphyrin is buried in the membrane but channel has the opposite orientation to c.

Control studies will be required to support these preliminary results. Flash photolysis experiments, as described above, conducted after the formation of the C20 bolaamphiphile:cholesterol vesicles in the presence of MV^{2+} inside and outside, are expected to show quenching of the porphyrin triplet state if the porphyrin moiety does indeed reside in the hydrophobic region of the membrane facing towards the vesicle interior. The absence of quenching in the presence of MV^{2+} inside and outside would indicate that the porphyrin moiety is buried deep in the membrane, regardless of the orientation of the GAP. A random orientation of the GAP may also allow the C10 MV^{2+} to be reduced. Other studies with variable chain length alkylviologens in different vesicle configurations (i.e., inside, outside, and both inside and outside) may be used to probe for the location of the porphyrin. The results are encouraging enough to warrant the synthesis of the GAPQ triad and undertake a comprehensive study of the spatial organization and photochemical properties.

5.2 Sodium Nuclear Magnetic Resonance

5.2.1 Introduction

The key feature of the bolaamphiphile GAPQ system design is the use of an ion channel as a linker between the porphyrin and quinone. The photogenerated charge-separated donor/acceptor pair in this case is electroneutral since it involves electron transfer across the vesicle membrane followed by ion translocation. The choice of gramicidin as a linker was based on the notion that, in principle, it could transfer cations in response to the photochemically generated transmembrane gradient, thereby dissipating charge development. Therefore, it was essential to test the permeability of Na^+ ions through bolaamphiphile:cholesterol vesicle samples containing either native or derivatized gramicidin. Hinton and coworkers [22,23] were able to show by ^{23}Na NMR that native gramicidin channels are conductive in 4:1 phosphatidylcholine:phosphatidylglycerol (PC:PG) vesicles. There are distinct differences between the Hinton case and the C20 bolaamphiphile:cholesterol systems. Since the bolaamphiphile membranes are much thinner than 4:1 PC:PG bilayer membranes, the gramicidin channel is most likely inserting as a monomer instead of

the dimeric form which occurs in biomembranes [18,24–28]. Experiments were undertaken to determine whether bolaamphiphile:cholesterol membranes are capable of forming an ion-impermeable barrier. Experiments were also conducted to ascertain whether gramicidin insertion results in ion conductivity. Finally, experiments were performed to establish if the gramicidin derivatized with porphyrin conducts ions. The outcome of these experiments would determine whether efforts towards building a photosynthetic model using bolaamphiphile:cholesterol vesicles with derivatized gramicidin channels should be continued.

5.2.2 Experimental

The sodium NMR experiments were conducted with a JEOL FX-90Q spectrometer using a 10-mm probe. Typically, C20 bolaamphiphile (18 mg, 16.8 mmol) and cholesterol (2.78 mg, 7.2 mmol) were co-dissolved in 2:1 chloroform:methanol and the solvent removed by evaporation under a nitrogen stream. 0.5 ml of D₂O or 100 mmol sodium chloride solution in D₂O was then added. The system was subjected to 5 cycles of freezing in liquid nitrogen, thawing, and vortexing to hydrate the lipid. After the lipid was hydrated, the size of the vesicles was selected through 10 cycles of extrusion using 0.08- μ m polycarbonate membranes. Gramicidin A (0.095 mg/ml, 0.11mM) or GAP (0.28 mg/ml) was then introduced to the vesicles as trifluoroethanol solutions at a rate of 2 ml/min and incubated for 90 min. Trifluoroethanol was chosen because it delivers the monomeric form of gramicidin [29,30]. Trifluoroethanol also permits the incorporation of gramicidin into diacylphosphatidylcholines as the $\beta^{6.3}$ helical conformation [31].

The key to determining Na⁺ ion conductivity across the membrane is distinguishing between the Na⁺ ion signals arising from the two pools, i.e., inside the vesicle and outside. This is achieved by adding 80 μ l of 10 mM of the membrane impermeable reagent, dysprosium(III) tripolyphosphate (Dy(PPP)₂), to 7:3 C20 bolaamphiphile:cholesterol vesicles after formation [32]. In this way, signals arising from Na⁺ ions outside the vesicles are shifted upfield relative to the sodium signals generated by the internally trapped species. Figure 5.10 shows the shift in the ²³Na

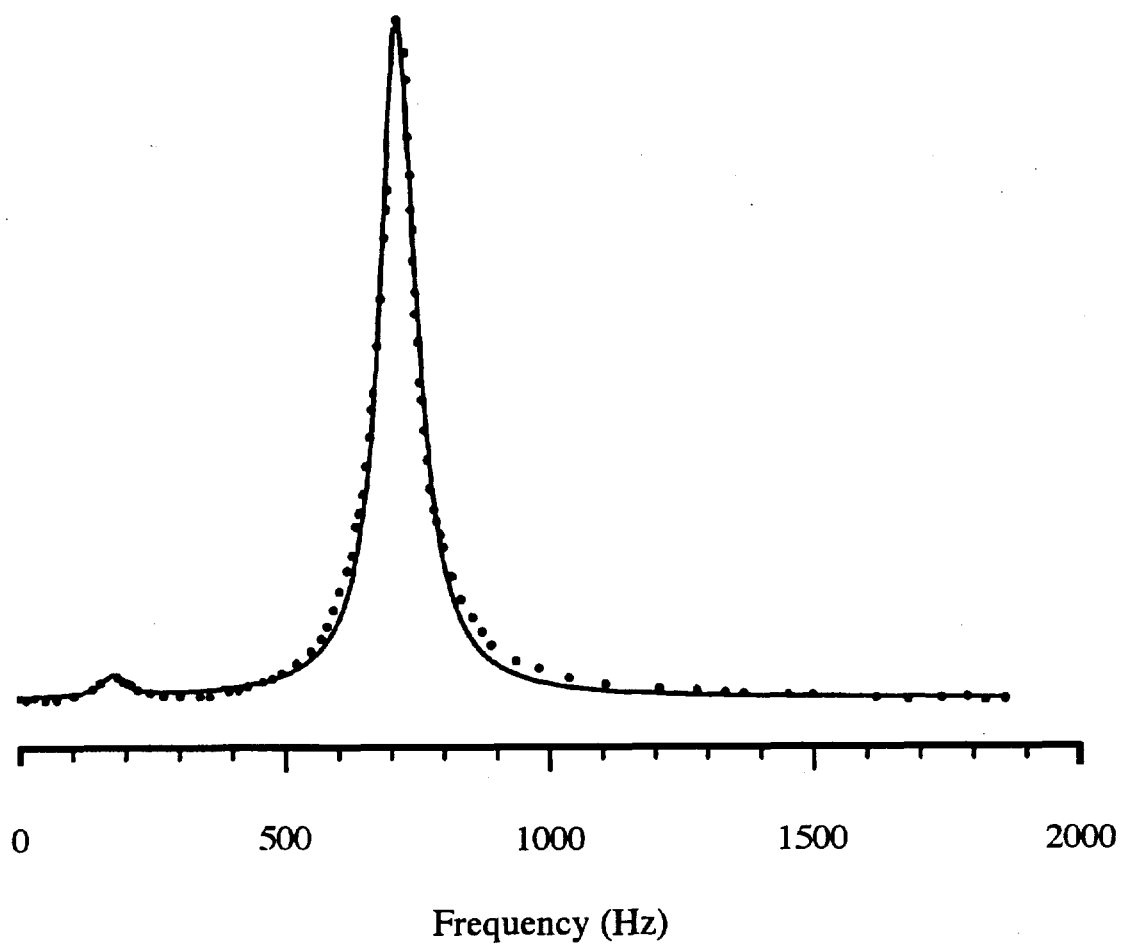


Figure 5.10 Sodium NMR spectral data (points) and NLSFIT simulation (line) of 7:3 C20 bolaamphiphile:cholesterol vesicles (in the absence of gramicidin A) with sodium ions inside and $\text{Dy}(\text{PPP})_2$ outside. This corresponds to an ion exchange rate of 0 ions per second.

NMR signal in the presence of Dy(PPP)₂ (180 Hz) arising from the outer pool, compared to the unshifted Na⁺ signal (710 Hz) arising from the inner pool.

The permeability of the bolaamphiphile membranes was then investigated using variable amounts of cholesterol in the C20 and C16 bolaamphiphile systems. (Recall that cholesterol addition was required for the formation of stable vesicles; see Chapter 4). To determine the bolaamphiphile:cholesterol ratio required for vesicles to be stable against sodium leakage, three formulations of each bolaamphiphile were extruded as described previously (20 mM tris buffer, pH 8), followed by addition of 60 μ l of 10 mM Dy(PPP)₂ and 100 mM NaCl. The ratios of C20 bolaamphiphile:cholesterol were 9:1, 8:2 and 7:3. The ratios of C16 bolaamphiphile:cholesterol were 8:2, 7:3, and 6:4. It was found that 30% cholesterol was sufficient for the vesicles of C20 bolaamphiphile to be stable toward Na⁺ leakage for at least 39 h, whereas with less cholesterol there was no discrimination between the two environments. All C16 bolaamphiphile:cholesterol mixtures studied rapidly leaked Na⁺ ions and therefore were not suitable for channel activity studies.

To determine whether gramicidin conducted sodium ions in the 7:3 C20 bolaamphiphile:cholesterol system, vesicles were prepared in the absence of sodium; then gramicidin was inserted into the vesicles such that there was an average of one channel per vesicle. 80 μ l of 50 mM Dy(PPP)₂ and 100 mM NaCl were then added and the NMR spectra acquired as a function of time. This trial indicated that the reaction was over in the time frame prior to acquisition of the first spectrum (the time required for reagent addition, instrument shimming and data acquisition; approximately 2 minutes). The porphyrin-derivatized gramicidin also promoted rapid sodium ion translocation in a similar screening. Given the rapid exchange rates, equilibrium state experiments were then performed by changing the gramicidin:vesicle ratio from 0:1, 1:1 and 5:1 (Figures 5.11, 5.12 and 5.13, respectively). In addition, the GAP system was studied with a GAP:vesicle ratio of 10:1 (Figure 5.14). These ratios were based on calculations from the vesicle diameters, and the weighted average molecular area of 60 \AA^2 in mixtures of 7:3 C20 bolaamphiphile:cholesterol, giving 16,000 lipid molecules per vesicle. As gramicidin was added, rapid exchange between the two Na₊ environments occurred such that the peak resolution decreased

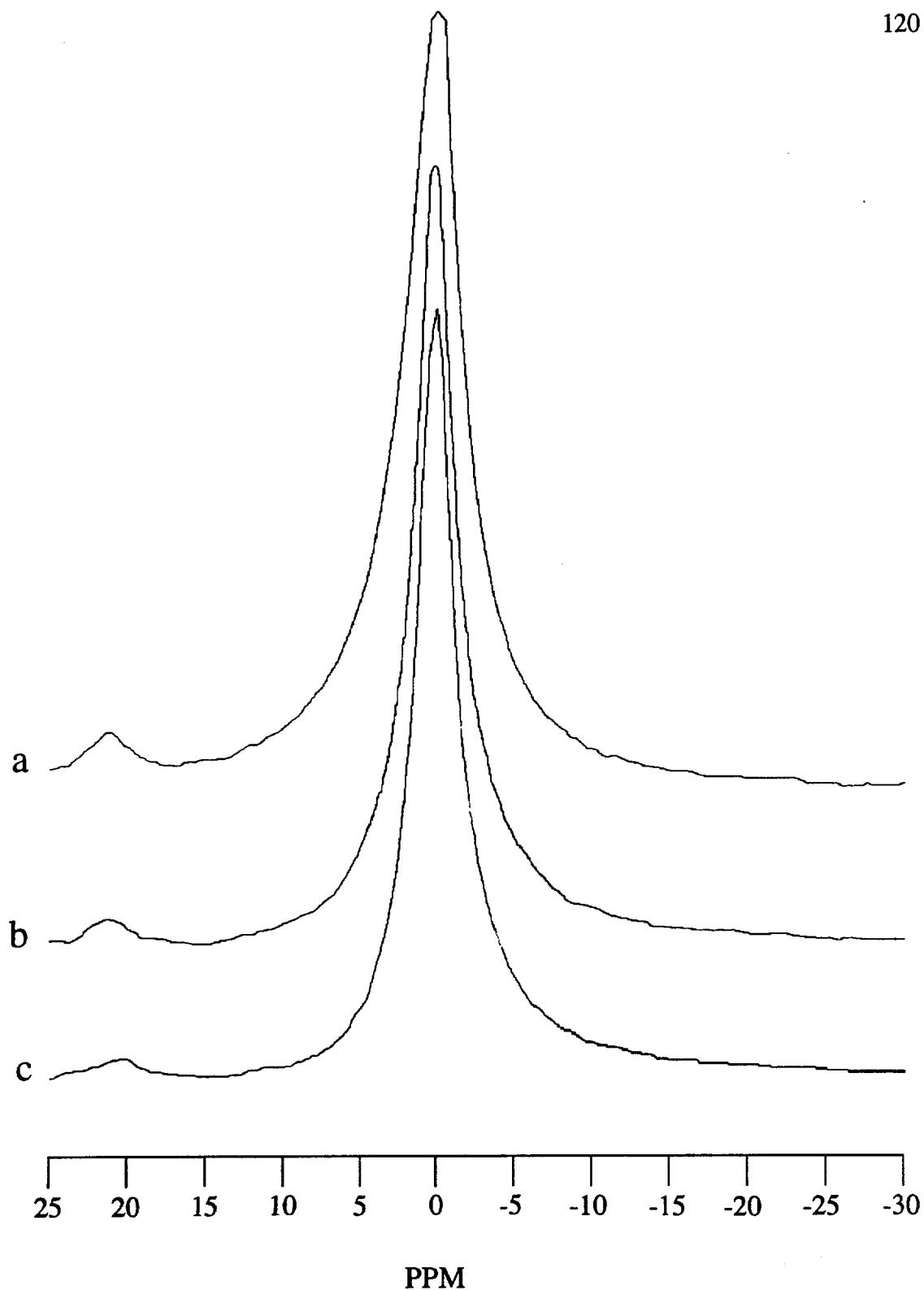


Figure 5.11 Sodium NMR spectra of vesicles measuring leakage as a function of time. To determine the stability of vesicles towards ion leakage, a sodium NMR study of 7:3 C20 bolaamphiphile:cholesterol vesicles with entrapped sodium ions inside (21 PPM) and dysprosium tripolyphosphate shifted sodium ions outside (0 PPM) was studied as a function of time. (a) Initial data; (b) 12 hours; (c) 39 hours.

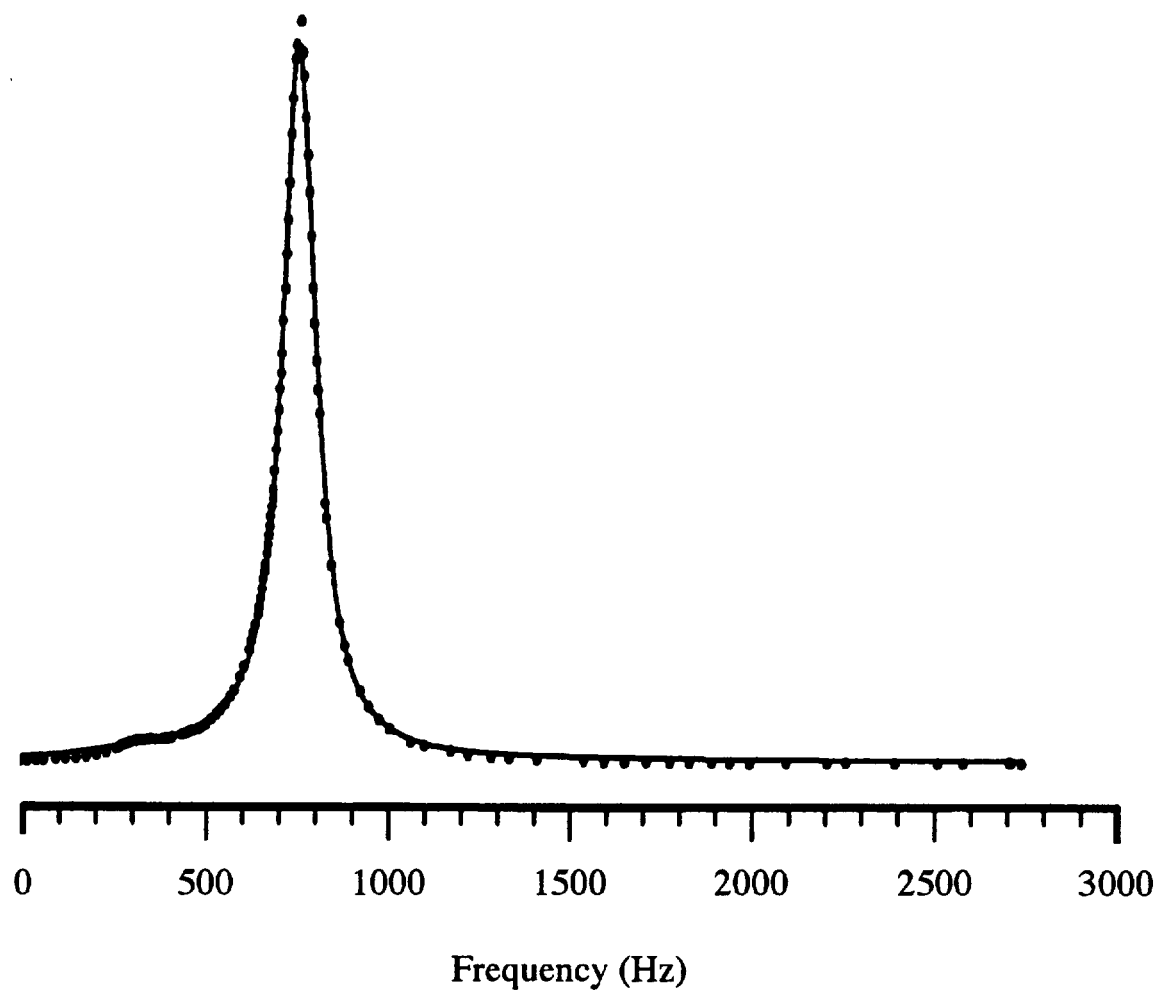


Figure 5.12 Sodium NMR spectral data (points) and the NLSFIT simulation (line) of 7:3 C20 bolaamphiphile:cholesterol vesicles with one native gramicidin channel inserted within the membrane and Dy(PPP)₂ added outside. This corresponds to an ion exchange rate of 1060 ± 89 ions per second per channel.

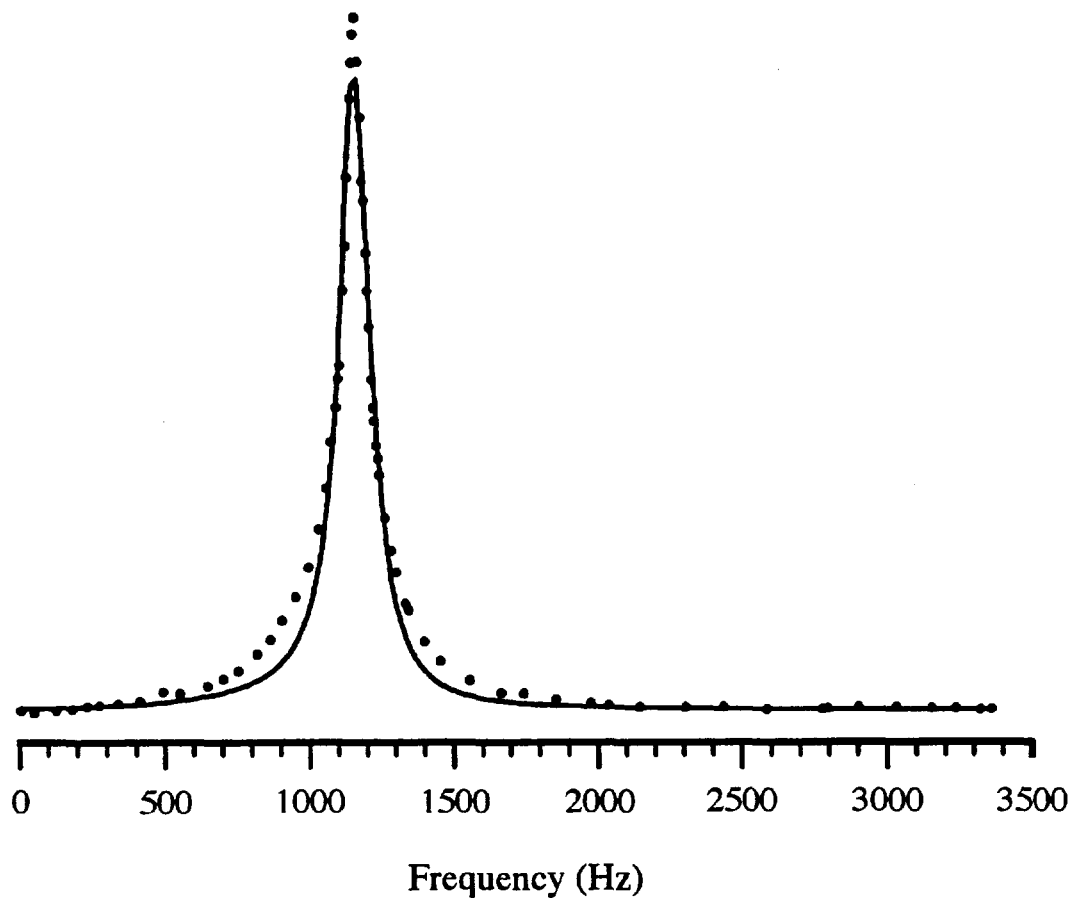


Figure 5.13 Sodium NMR spectral data (points) and the NLSFIT simulation (line) of 7:3 C20 bolaamphiphile:cholesterol vesicles with five native gramicidin channels inserted within the membrane and Dy(PPP)₂ outside. This corresponds to an ion exchange rate of 456 ± 67.8 ions per second per channel.

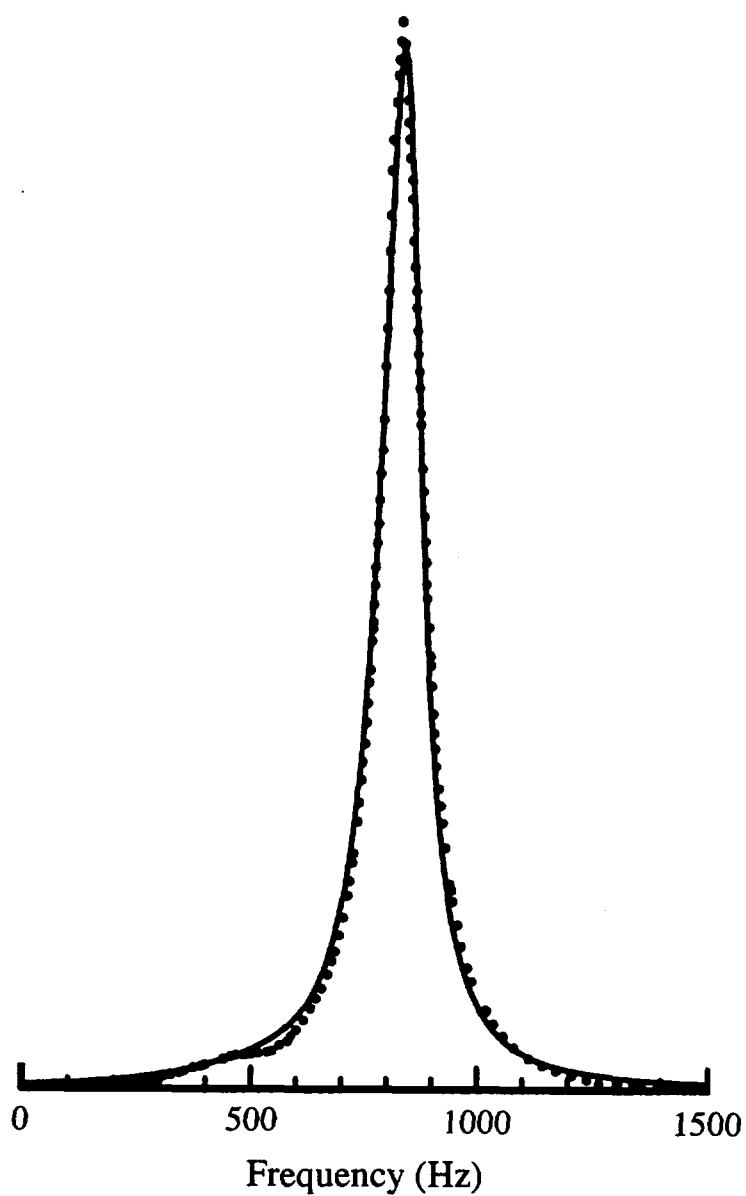


Figure 5.14 Sodium NMR spectral data (points) and NLSFIT simulation (line) of C20 bolaamphiphiles:cholesterol vesicles containing 10 GAP channels per vesicle. The exchange rate was determined to be 4914 ± 678 ions per second which corresponds to 491.4 ± 67.8 ions per second per channel.

as transmembrane diffusion was rapid on the NMR timescale. These spectra were compared to data taken from Hinton and coworkers [22], where the gramicidin:vesicle ratios were 0:1, 111:1, and 166:1 (Figures 5.15–5.17). Computational modeling was performed based on the matrix formulations of the modified Bloch equations [34]. To determine the rate of exchange, computational modeling of multi-site exchange was undertaken based on the expression:

$$I(X) = A\{(r + k)B + (X + (1 - 2P_A)W)C/(B^2 + C^2)\}$$

where

$$A = \text{normalization constant}$$

$$B = (1/T_2)(r + k) + W^2 - x^2$$

$$C = 2[rx - (1 - 2P_A)kW]$$

Tables 5.1 and 5.2 present the data from the spectra digitized from the experiments of Hinton on 4:1 phosphatidylcholine:phosphatidylglycerol (PC:PG):gramicidin systems, and the data obtained from the 7:3 C20 bolaamphiphile:cholesterol:gramicidin and 7:3 C20 bolaamphiphile:cholesterol:GAP systems [22]. Figures 5.18 and 5.19 simulate spectra from the two systems as the ion exchange rates are varied between 1–5000 ions per second for the Hinton case with 0.4- μm vesicles (Figure 5.18) and the C20 bolaamphiphile:cholesterol case of 0.1- μm vesicles (Figure 5.19).

Computational analysis of the sodium NMR data suggests that both native gramicidin and GAP channels incorporated in C20 bolaamphiphile:cholesterol membranes improve the ion exchange rates. These exchange rates are two to three orders of magnitude more rapid, under ionic equilibrium, than in 4:1 PC:PG bilayer membrane vesicles. In Hinton's system where the gramicidin A:vesicle ratio (GA:V) was 0:1, the background exchange rate was determined to be 2.08 ± 7.25 ; for a GA:V of 111:1, the exchange rate was 1.43 ± 0.09 ion channels per second (i/c/s) while for a GA:V of 166:1, the exchange rate was 1.83 ± 0.07 i/c/s. For the C20 bolaamphiphile:cholesterol case, when the GA:V ratio was 0:1, the exchange rate was 0 i/c/s; for a GA:V ratio of 1:1, the exchange rate was 1060 ± 89 i/c/s. For a GA:V ratio of 5:1, the exchange rate was 456 ± 60.2 i/c/s while a GAP:vesicle ratio of 10:1 produced an exchange rate of 491 ± 67.8 i/c/s. This enhancement of exchange rate in the bolaamphiphile systems is attributed to a different Na_+

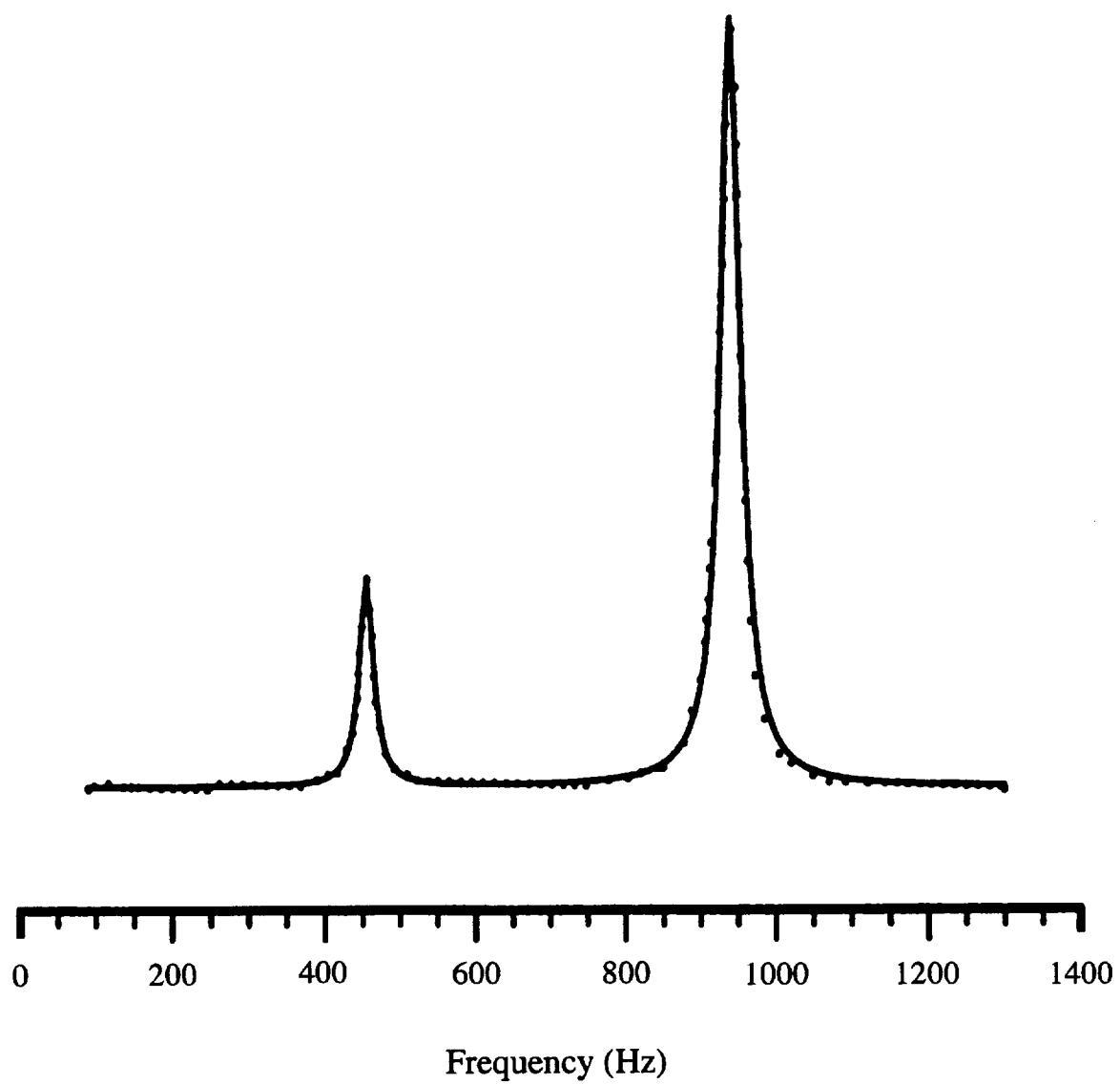


Figure 5.15 Sodium NMR spectral data (points) and the NLSFIT simulation (line) of 4:1 phosphatidylcholine:phosphatidylglycerol vesicles in the absence of gramicidin channels. The exchange rate was determined to be 2.08 ± 7.25 ions per second [22].

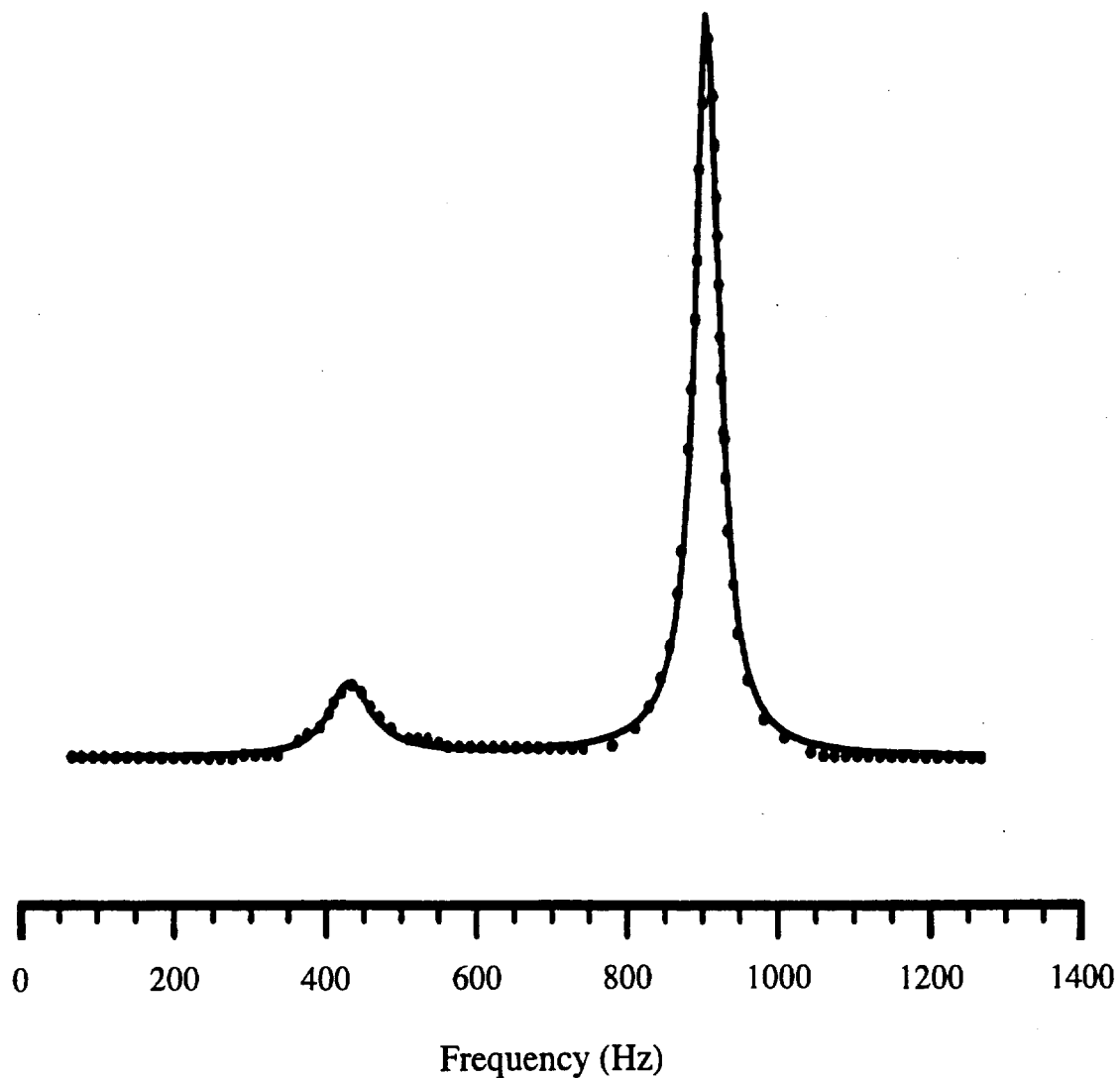


Figure 5.16 Sodium NMR spectral data (points) and NLSFIT simulation (line) of 4:1 phosphatidylcholine:phosphotidylglycerol vesicles containing 110 gramicidin channels per vesicle. The exchange rate was determined to be 158 ± 10 ions per second which corresponds to an exchange rate of 1.43 ± 0.09 ions per second per channel [22].

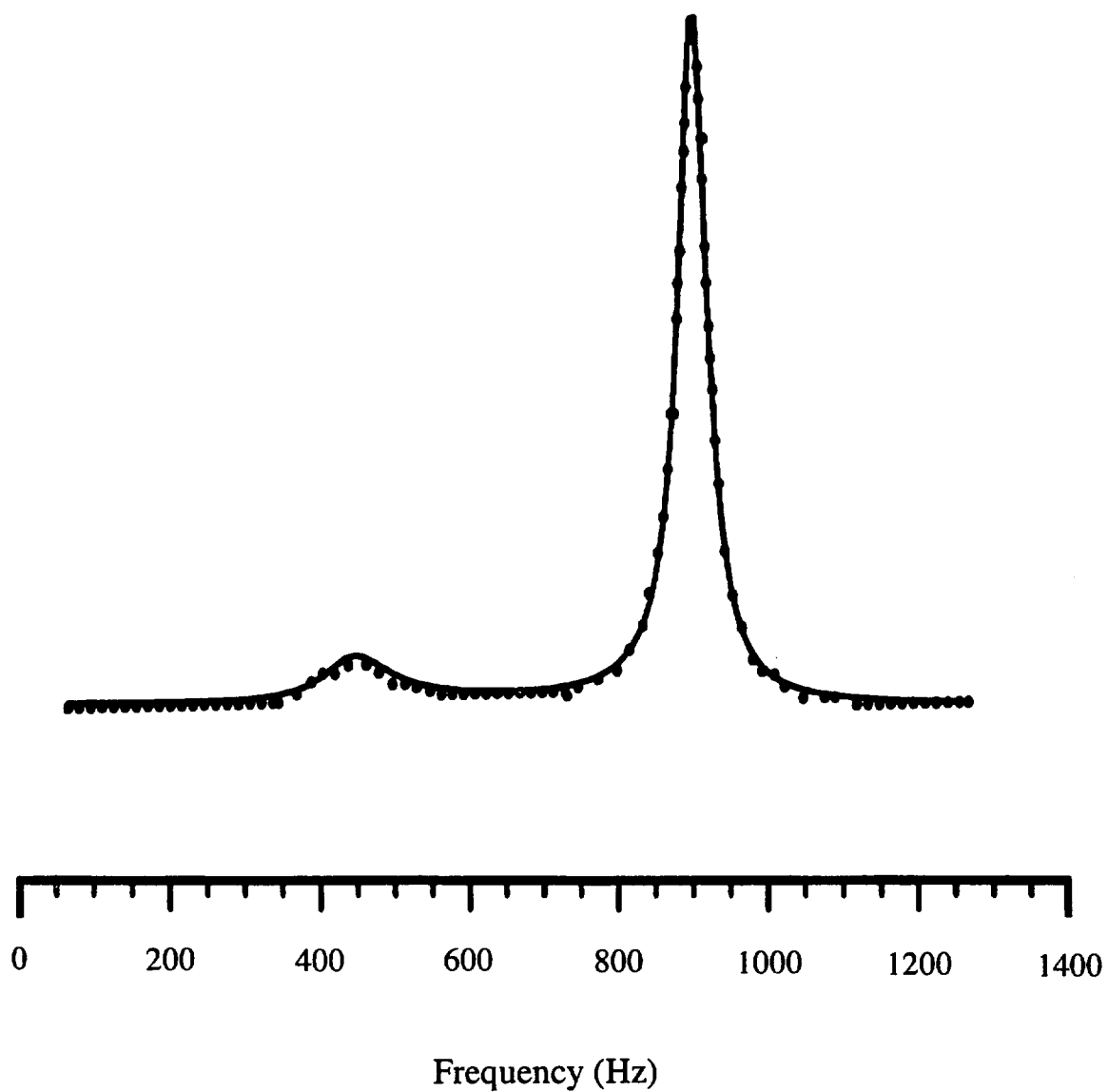


Figure 5.17 Sodium NMR spectral data digitized from published data [22] and NLSFIT simulation (line) of 4:1 phosphatidylcholine:phosphatidylglycerol vesicles containing 166 gramicidin channels per vesicle. The exchange rate was determined to be 304 ± 12 ions per second which corresponds to 1.83 ± 0.07 ions per second per channel [22].

Table 5.1
 Summary of ^{23}A NMR Parameters for 4:1
 Phosphatidylcholine:Phosphatidylglycerol Vesicles Containing Gramicidin A
 (analysis of data reported in [22])

	Spectrum		
	A^a	B^b	C^c
A^d	32079 ± 446	31142 ± 25	29191 ± 407
k^e	2.08 ± 7.25	157.98 ± 9.98	304 ± 12
ω_1^f	429.93 ± 0.62	420 ± 2.68	447.18 ± 0.16
ω_2^f	915.78 ± 0.16	898.2 ± 0.22	907 ± 0.19
b_1^g	70	70	70
b_2^g	100	100	100
P_1^h	0.162 ± 0.072	0.14 ± 0.07	0.138 ± 0.09
χ^2^i	45	10.33	8.32
C/V^j	0	100.67	166
$i/c/s^k$	NA	1.43 ± 0.09	1.83 ± 0.07

^a Control with no gramicidin A inserted in PC:PG vesicles

^b PC:PG vesicles containing an average of 111 gramicidin A monomers

^c PC:PG vesicles containing an average of 166 gramicidin A monomers

^d A is a normalization factor

^e k is the ion exchange rate

^f ω_1 and ω_2 are the peak positions

^g b_1 and b_2 are the respective line broadenings

^h P_1 is the entrapped volume

ⁱ χ^2 is the statistical fit

^j C/V is the number of channels per vesicle

^k $i/c/s$ is the ion exchange rate per channel per second

Table 5.2

Summary of ^{23}Na NMR Parameters for 7:3 C20 Bolaamphiphile:Cholesterol Vesicles Containing Either Gramicidin A or GAP

	Spectrum			
	A ^a	B ^b	C ^b	D ^c
A ^d	79146 ± 1605	141,979 ± 677	147,200 ± 2900	1586 ± 8.9
k ^e	(1)	1060 ± 89	2281 ± 301	4914 ± 678
ω_1^f	186.95 ± 24.29	282	667	430
ω_2^f	729.10 ± 0.48	772.29 ± 0.38	1167	830 ± 0.6
b ₁ ^g	174 ± 241	183	183	183
b ₂ ^g	263 ± 5.7	311	311	311
P ₁ ^h	0.0195 ± 0.161	0.034 ± 0.0029	0.0593 ± 0.007	0.03
χ^2 ⁱ	77.84	14	161	0.0095
C/V ^j	0	1	5	10
i/c/s ^k	0	1060 ± 89	456 ± 60.2	491 ± 67.8

^a Control vesicles (7:3 C20 bolaamphiphile:cholesterol) containing no inserted gramicidin channels

^b 7:3 C20 bolaamphiphile:cholesterol vesicles containing native gramicidin

^c 7:3 C20 bolaamphiphile:cholesterol vesicles containing GAP

^d A is a normalization factor

^e k is the ion exchange rate

^f ω_1 and ω_2 are the peak positions

^g b₁ and b₂ are the respective line broadenings

^h P₁ is the entrapped volume

ⁱ χ^2 is the statistical fit

^j C/V is the number of channels per vesicle

^k i/c/s is the ion exchange rate per channel per second

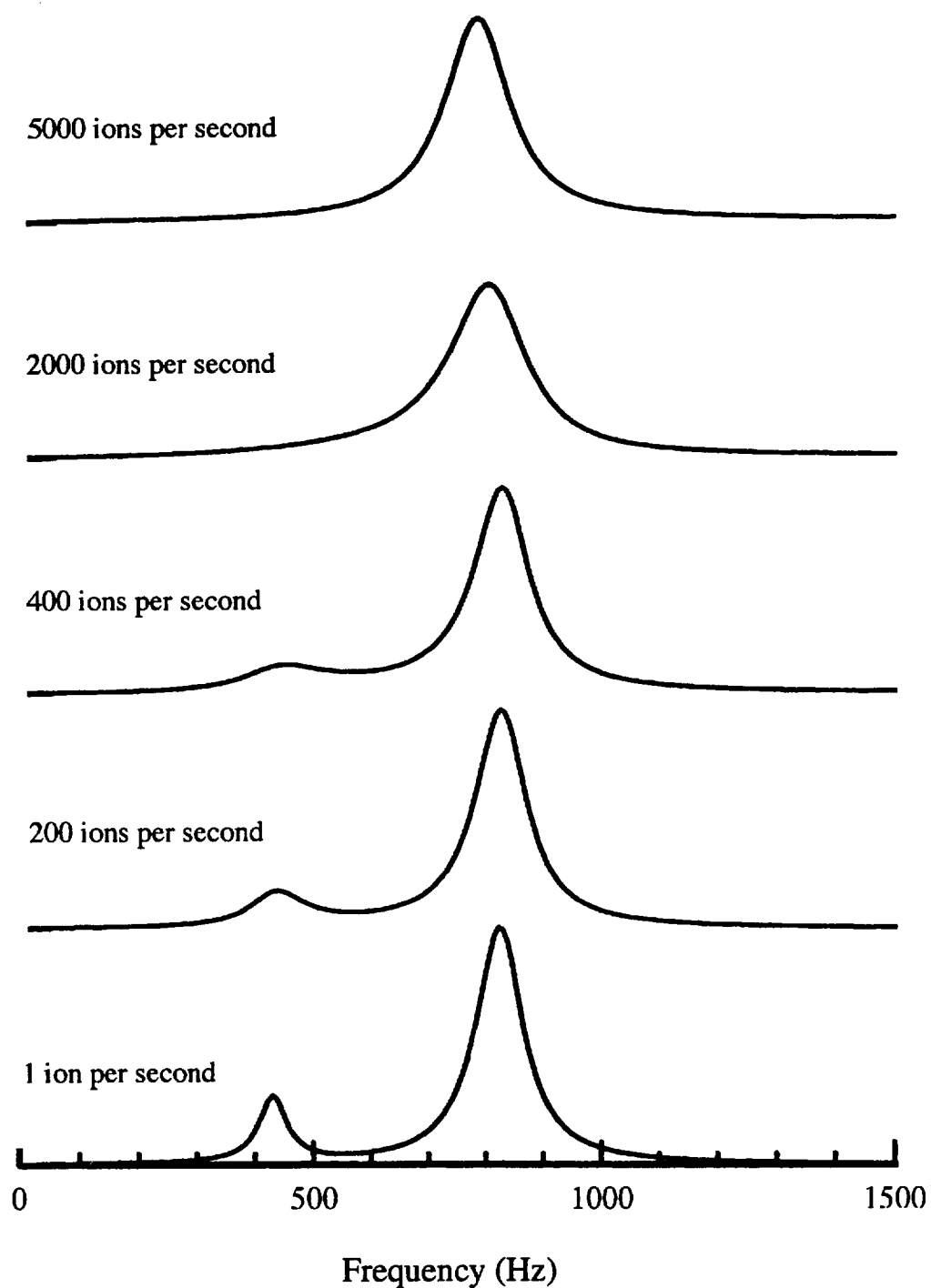


Figure 5.18 NMR computer simulation of 0.4-micron vesicles (similar to those of Hinton [22]) while the exchange rates are varied up to 5000 ions per second. As the exchange rate increases, the lines broaden. The peak at lower frequency is from ions within the vesicles while the higher frequency peak arises from the ions outside the vesicles.

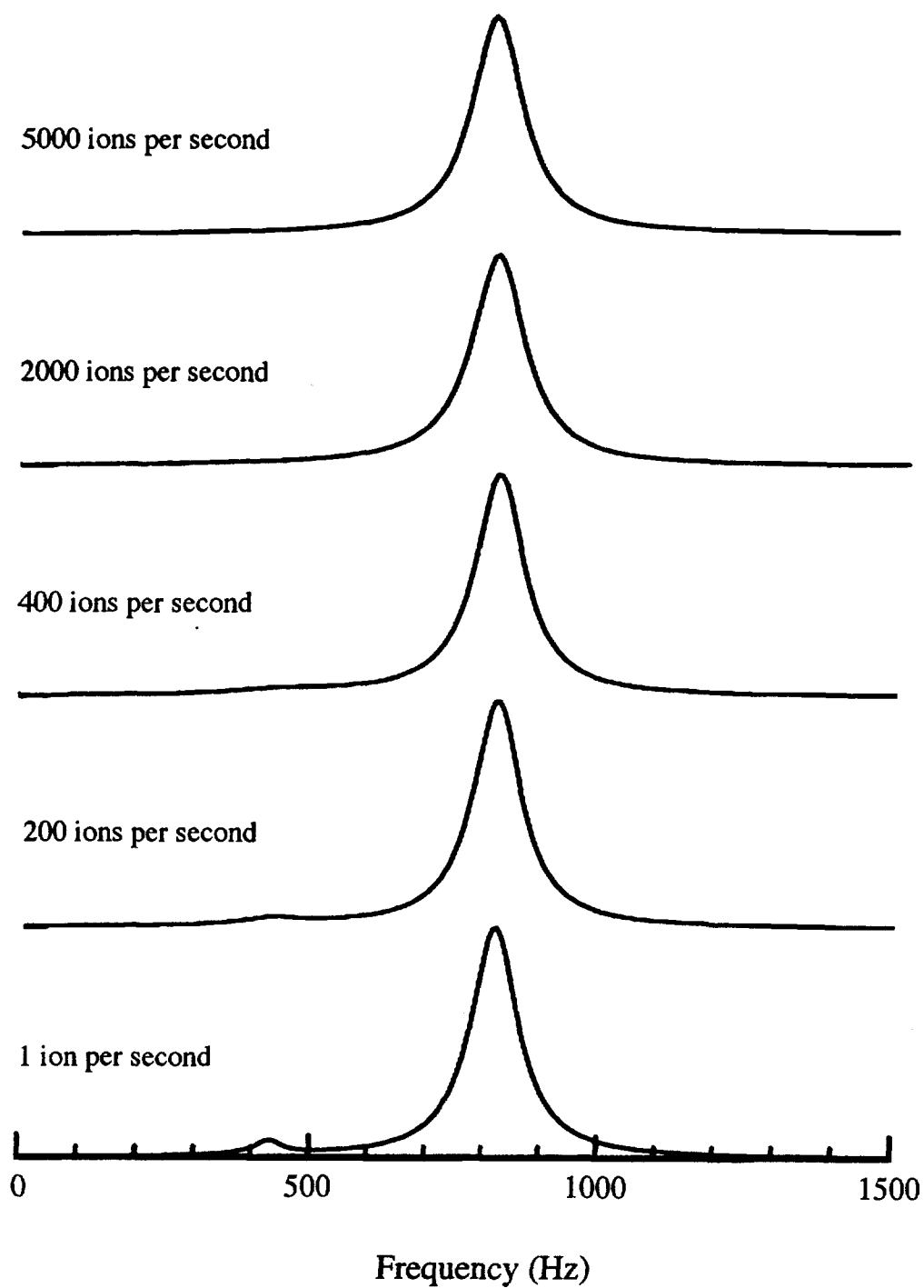


Figure 5.19 NMR computer simulation of 0.1-micron vesicles while the exchange rates are varied up to 5000 ions per second. As the exchange rate increases, the lines broaden. The peak at the lower frequency is from ions within the vesicles while the higher frequency peak arises from the ions outside the vesicles.

conduction pathway in the two systems. The channel acts in the dimeric state in 4:1 PC:PG bilayer membranes and is subject to flickering between conductive and nonconductive states as the channel associates and dissociates; thus, lateral diffusion of gramicidin A monomers, followed by docking of the dimer via H-bonding of the opposing N-formyl termini becomes the rate-determining step [33]. The thin dimension of the C20 bolaamphiphile:cholesterol membrane is believed to permit channel activity in the monomeric state such that the channel does not flicker, but rather is present in a continual "on" state.

The performance of the C20 bolaamphiphile:cholesterol GAP system in the sodium NMR experiments indicates that despite terminal derivatization of the gramicidin A with a porphyrin, the monomeric channel of the GAP diad was even better at translocating ions than the native dimeric gramicidin state. The outcome of these sodium NMR experiments indicates that continued development of the system is warranted.

5.3 References

1. Kuhn, E. R. and Hurst, J. K. (1993) Mechanisms of vectorial transmembrane reduction of viologens across phosphatidylcholine bilayer membranes. *J. Phys. Chem.* **97**, 1712–1721.
2. Patterson, B. C. and Hurst, J. K. (1993) Pathways of viologen-mediated oxidation-reduction reactions across dihexadecyl phosphate bilayer membranes. *J. Phys. Chem.* **97**, 454–465.
3. Lee, L. Y.-C., Hurst, J. K., Politi, M., Kurihara, K., and Fendler, J. H. (1983) Photoinduced diffusion of methylviologen across anionic surfactant vesicle bilayers. *J. Am. Chem. Soc.* **105**, 370–373.
4. Hurst, J. K. (1991) Dynamics of charge separation across vesicle membranes. In *Kinetics and Catalysis in Microheterogeneous Systems*, Surfactant Sciences Series, Vol 38, Marcel Dekker, New York, 183–226.
5. Lymar, S. V., Parmon, V. N., and Zamaraev, K. I. (1991) Photoinduced electron transfer across lipid membranes. In *Topics in Current Chemistry*, vol. 159, Springer-Verlag, Berlin, 1–66.
6. Robinson, J. N. and Cole-Hamilton, D. J. (1991) Electron-transfer across vesicle bilayers. *Chem. Soc. Rev.* **20**, 49–94.
7. Runquist, J. A. and Loach, P. A. (1981) Catalysis of electron transfer across phospholipid bilayers by iron-porphyrin complexes. *Biochim. Biophys. Acta* **673**, 231–244.
8. Patterson, B. C., Thompson, D. H., and Hurst, J. K. (1988) Methylviologen mediated oxidation-reduction across dihexadecylphosphate vesicles involves transmembrane diffusion. *J. Am. Chem. Soc.* **110**, 3656–3657.
9. Patterson, B. C. and Hurst, J. K. (1990) Cation regulated viologen-mediated transmembrane electron transfer. *J. Chem. Soc., Chem. Comm.* **17**, 1137–1138.
10. Lymar, S. V. and Hurst, J. K. (1992) Mechanisms of viologen-mediated charge separation across bilayer membranes deduced from mediator permeabilities. *J. Am. Chem. Soc.* **114**, 9498–9503.
11. Humphry-Baker, R., Thompson, D. H., Lei, Y., Hope, M. J., and Hurst, J. K. (1991) Structural investigations of dihexadecyl phosphate small unilamellar vesicles. *Langmuir* **7**, 2592–2601.

12. Lyman, S. V. and Hurst, J. K. (1994) Electrogenic and electroneutral pathways for methyl viologen-mediated transmembrane oxidation-reduction across dihexadecylphosphate vesicular membranes. *J. Phys. Chem.* **98**, 989-996.
13. Colaneri, M. J., Kevan, L., Thompson, D. H. P., and Hurst, J. K. (1987) Variation of alkylmethylviologen radical cation water interactions in micelles and vesicles from ESEM spectroscopy—effect of alkyl chain-length. *J. Phys. Chem.* **91**, 4072-4077.
14. Lei, Y. and Hurst, J. K. (1991) Reduction potentials of vesicle-bound viologens. *J. Phys. Chem.* **95**, 7918-7925.
15. Thompson, D. H. P., Barrette W. C., and Hurst, J. K. (1987) One-electron reduction of dihexadecyl phosphate vesicle bound viologens by dithionite ion. *J. Am. Chem. Soc.* **109**, 2003-2009.
16. Hammarström, L., Berglund, H., and Almgren, M. (1994) Transmembrane electron transfer by diheptylviologen: Disproportionation of viologen radical and viologen-induced leakage of external reductant. *J. Phys. Chem.* **98**, 9588-9593.
17. Hurst, J. K., Lee, L. Y., and Grätzel, M. (1983) Photoredox behavior of zinc (II) porphyrins in vesicle assemblies. *J. Am. Chem. Soc.* **105**, 7048-7056.
18. Wallace, B. A. (1986) Structure of gramicidin A. *Biophys. J.* **49**, 295-306.
19. Thompson, D. H., Kim, J.-M., and Di Meglio, C. (1993) Photoinduced charge transfer of bolaamphiphile membrane-gramicidin diad composites. In *Organic and Biological Optoelectronics*, SPIE **1853**, 142-147.
20. Killian, J. A., Tournois, H., and De Kruijff, B. (1990) Functional and structural aspects of gramicidin-lipid interactions. In *Dynamics and Biogenesis of Membranes* (Op den Kamp, J. A. F., ed.), NATO ASI Series, vol. H40, Springer-Verlag, Berlin, Heidelberg, 167-183.
21. Vogt, T. C. B., Killian, J. A., Demel, R. A., and De Kruijff, B. (1991) Synthesis of acylated gramicidins and the influence of acylation on the interfacial properties and conformational behavior of gramicidin-A. *Biochim. Biophys. Acta* **1069**, 157-164.
22. Buster, D. C., Hinton, J. F., Millet, F. S., and Shungu, D. C. (1988) Na-23-nuclear magnetic-resonance investigation of gramicidin-induced ion-transport through membranes under equilibrium conditions. *Biophys. J.* **53**, 145-152.

23. Hinton, J. F., Easton, P. L., Newkirk, D. K., and Shungu, S. C. (1993) Na-23-NMR study of ion-transport across vesicle membranes facilitated by phenylalanine analogs of gramicidin. *Biochim. Biophys. Acta* **1146**, 191–196.
24. He, K., Ludtke, S. J., Wu, Y., and Huang, H. W. (1993) X-ray-scattering with momentum transfer in the plane of membrane: Application to gramicidin organization. *Biophys. J.* **64**, 157–162.
25. Wallace, B. A., and Ravikumar, K. (1988) The gramicidin pore: crystal structure of a cesium complex. *Science* **241**, 182–187.
26. Langs, D. A. (1988) 3-Dimensional structure at 0.86 angstrom of the uncomplexed form of the transmembrane ion channel peptide gramicidin-a. *Science* **241**, 188–191.
27. Becker, M. D., Greathouse, D. V., Koeppe, R. E., and Andersen, O. S. (1991) Amino-acid-sequence modulation of gramicidin channel function—effects of tryptophan-to-phenylalanine substitutions on the single-channel conductance and duration. *Biochemistry* **30**, 8830–8839.
28. Watnick, P. I., Chan, S. I., and Dea, P. (1990) Hydrophobic mismatch in gramicidin-A'/lecithin systems. *Biochemistry* **29**, 6215–6221.
29. Urry, D. W., Mayers, D. F., and Haider, J. (1972) Spectroscopic studies on the conformation of gramicidin A. Evidence of a new helical conformation. *Biochemistry* **11**, 487–493.
30. Urry, D. W., Venkatachalam, C. M., Prasad, K. U., Bradley, R. J., Parenti-Castelli, G., and Lenaz, G. (1981) Conduction processes of the gramicidin channel. *Int. J. Quantum Chem. Quantum Biol. Symp.* **8**, 385–399.
31. Tournois, H., Killian, J. A., Urry, D. W., Bokking., O, R., De Gier, J., and De Kruijff, B. (1987) Solvent determined conformation of gramicidin affects the ability of the peptide to induce hexagonal H_{II} phase formation in dioleoylphosphatidylcholine model membranes. *Biochim. Biophys. Acta* **905**, 222–226.
32. Gupta, R. K., and Gupta, P. (1982) Direct observation of resolved resonances from intra-and extracellular sodium-23 ions in NMR studies of intact cells and tissues using dysprosium(III) tripolyphosphate as paramagnetic shift reagent. *J. Magn. Res.* **47**, 344–350.
33. O'Connell, A. M., Koeppe, R. E., and Andersen, O. S. (1990) Kinetics of gramicidin channel formation in lipid bilayers: transmembrane monomer association. *Science* **250**, 1256–1259.

34. Reeves, L. W., and Shaw, K. N. (1970) Nuclear magnetic resonance studies of multi-site chemical exchange. I. Matrix formulation of the Bloch equations. *Can. J. Chem.* **48**, 3641-3653.

CHAPTER 6

CONCLUSION

The goal of this research was to develop a new multicomponent supramolecular assembly and demonstrate its potential as a model for future solar photoconversion. Chapters 2–5 described the synthesis of bolaamphiphiles that were physically characterized in order to determine their suitability as host monolayer membranes for the inclusion of a photoactive ion channel. Chiral C16 and C20 bolaamphiphiles were successfully prepared on a gram scale as described in Chapter 2. The phase transition temperatures from differential scanning calorimetry experiments showed that the bolaamphiphiles exhibit melting transition temperatures similar to those displayed by the corresponding (conventional) dialkylglycerophosphocholine (i.e., T_c of C16 bolaamphiphile $\approx T_c$ predicted for dioctylglycerophosphocholine). Small-angle X-ray scattering experiments indicated the appearance of the vesicle phase at high water content, giving transmembrane dimensions of 32 Å for the C20 bolaamphiphile and 33 Å for the C16 bolaamphiphile. Cryo-transmission electron microscopy experiments and dynamic light-scattering experiments indicated that, in the presence of cholesterol, C20 bolaamphiphiles assembled into stable vesicles having a narrow size distribution. Molecular areas obtained from monolayer experiments were consistent with a U-shaped configuration that places the two phosphocholine headgroups towards the aqueous subphase. The outcome of these experiments supported the predictions for these bolaamphiphiles and encouraged the effort to further develop the photosynthetic model system.

The next task was to determine whether incorporation of the photoactive ion channel, GAP, could take place in vectorial mode.

The porphyrin linked to the GAP diad and inserted into extruded C20 bolaamphiphile:cholesterol vesicles using the 1,1,1-trifluoroethanol procedure, was shown to be inaccessible to external methylviologen by the flash photolysis experiments (Chapter 5). The absence of triplet-state quenching suggests that it is oriented away from the outer vesicle water interface by the gramicidin. Additional bulk photolysis experiments using a sacrificial electron donor entrapped inside the vesicle indicated that externally added alkylviologens could be photo-reduced. Although these experiments support the transmembrane electron transfer model, they are not unequivocal evidence for the transmembrane organization of the redox components. Additional control experiments are necessary to prove the orientation of the GAP module in the membrane.

The last contribution to the project focused on the ion-conducting ability of the GAP diad inserted into C20 bolaamphiphile:cholesterol vesicles. Using sodium NMR experiments, the C20 bolaamphiphile:cholesterol vesicles were shown to be impermeable to sodium ions in the absence of gramicidin. In the presence of either native gramicidin or GAP, the channel demonstrated a remarkable ability to translocate sodium ions by three orders of magnitude more rapidly than that shown for gramicidin in bilayer lipid membranes.

These studies of the multifunctional bolaamphiphile:cholesterol:GAP system suggest that it should be further developed as a model for solar photoconversion. Future experiments should focus on covalently linking a quinone acceptor moiety to GAP (producing GAPQ) (Figure 6.1) in order to complete the photoinduced electron transfer complex. Once the GAPQ "triad" is obtained, experiments to determine its organization in monolayer membranes will be needed. As with the GAP "diad," flash photolysis experiments should establish whether transmembrane photoinduced electron transfer can be accomplished. If electron transfer does not occur, the GAPQ triad complex can be "fine tuned" to poise the donor and acceptor in a more favorable spatial arrangement through the introduction of additional linkages between the gramicidin channel and the porphyrin and/or quinone moieties.

To determine the orientation of the GAPQ triad in bolaamphiphile monolayer membranes, experiments similar to the steady-state photolysis experiments with

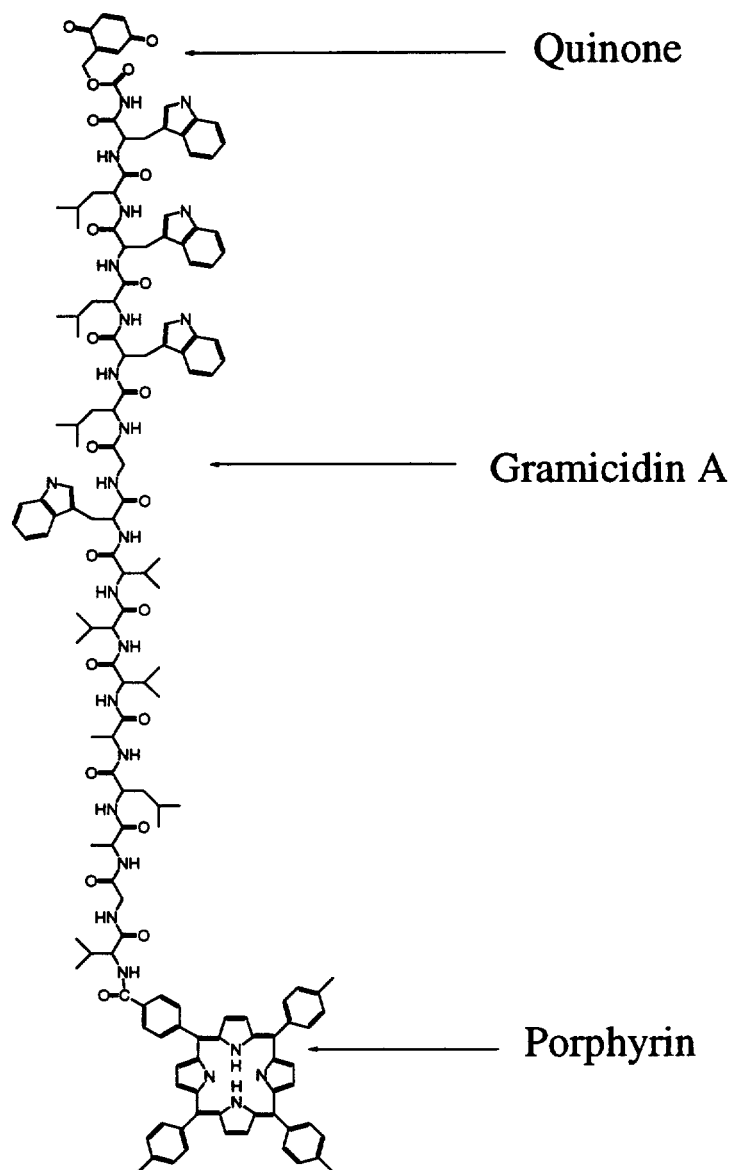


Figure 6.1. The GAPQ triad.

sacrificial donors (Chapter 5) should be undertaken. By varying the configuration of the system, insight may be obtained regarding the preferred orientation of the GAPQ in the thin host membrane.

Assuming that a working electron transfer complex can be achieved, the ion channel activity will also need to be reexamined. This is required to determine whether the additional structural changes associated with the incorporation of the quinone and tether segments will have undermined the ability of the channel to translocate cations. Sodium NMR experiments similar to those conducted on the partially derivatized GAP channel can be used for GAPQ:bolaamphiphile dispersions. A study where the GAPQ triad is incrementally added to liposomes of known entrapped volume would be aimed at determining possible aggregation effects upon GAPQ's ion channel conductivity. To further demonstrate that GAPQ is capable of functioning as a channel, known blocking agents can be added to demonstrate their interference with two-site ion exchange.

The studies presented in this dissertation demonstrate that opportunities exist for the development of a multifunctional supramolecular device using bolaamphiphile liposomes to achieve photoinduced electron and ion transfer. Modifications of this system may also find commercial application in planar membrane-based devices.

BIOGRAPHICAL SKETCH

Ciro Di Meglio was born in Norwalk, Connecticut on August 9, 1966 to Mr. & Mrs. Nicholas Di Meglio. He attended Joel Barlow High School and Worcester Polytechnic Institute, where he was awarded the B.S. degree in Chemistry in June 1989. While still an undergraduate he was employed by Alpha Analytical Laboratories in Westboro, Massachusetts. He began graduate study at the Oregon Graduate Institute of Science and Technology (OGI) in September 1990, doing research in the laboratory of Dr. David H. Thompson, now a faculty member at Purdue University. He was awarded the M.S. and Ph.D. degrees from OGI. While completing his dissertation, he joined Dr. Thompson's laboratory at Purdue.